

Development of High-Controllability Hot-Wire Welding Process for Enhanced Joint Properties and Weldability

(継手特性と溶接性の制御を可能とするホットワイヤ溶接技術
の開発)

September, 2023

Nattasak Suwannatee

Department of Mechanical Science and Engineering
Graduate School of Engineering
Hiroshima University

Abstract

The hot-wire gas metal arc welding (GMAW) process offers several advantages, including high deposition volume and reduced power consumption, reduced number of weld passes required, and increased process tolerance. Based on these benefits, this dissertation aims to achieve three main objectives.

First, the aim is to develop a single-pass welding method using hot-wire GMAW on 15-mm thick steel plate square butt joints without edge preparation. The author investigates the limitations of conventional GMAW and the effect of hot-wire fraction on the quality of the welded joints. The results demonstrated that the new approach yielded promising results when optimized conditions were applied. Specifically, a single-pass condition using a welding current of 450A, a hot-wire feeding speed of 15 m/min, and a travel speed of 0.6 m/min. Notably, this condition reduced power consumption by 81.25% and a remarkable saving of arc time by 91.67% compared to conventional GMAW.

Second, the aim is to determine the optimal hot-wire fraction and maximize deposition efficiency in GMAW. The author used hot-wire to compensate for the total deposition rate instead of relying solely on high welding current as in conventional GMAW. The hot-wire fraction was varied to identify its limitations. The findings showed that a hot-wire fraction of up to 41% of the total deposition rate provided a soundness condition. Beyond this threshold, issues such as molten metal precedence or lack of fusion will occur. By optimizing the ratio between hot-wire and GMAW fractions, a single-v butt joint on a 20-mm thick steel plate was achieved, resulting in a substantial 62% decrease in power consumption compared to conventional GMAW.

Last, the aim is to enhance joint properties through selective hot-wire filler metal during GMAW. The author used different filler wires with varying nickel (Ni) content to evaluate their impact on microstructure evolution, material characteristics, and fracture behavior. The results showed that increasing the Ni content increased the fraction of acicular ferrite in the weld metal, improving joint properties such as hardness and absorption energy. Hot-wire gas metal arc welding resulted in a 7% increase in hardness and a remarkable 45% increase in toughness compared to conventional GMAW. The hardness and toughness values of the weld metal varied based on the Ni content in the hot-wire filler metal. The findings highlighted the critical role of Ni content in determining the microstructure and mechanical properties of the weld metal. The addition of Ni through hot-wire insertion enabled the superior performance of the weld joint. Hot-wire insertion expands the process tolerance of GMAW sustainably, contributing to its ongoing development.

Table of Contents

Chapter 1	Introduction	1
1.1	Research background	1
1.1.1	State of the art in welding technology	1
1.1.2	Background of welded joint configuration	1
1.1.3	Background of narrow gap welding and hot-wire technology	2
1.2	Objectives and construction of the thesis.....	5
Chapter 2	Literature review	7
2.1	Introduction	7
2.2	Evolution of arc welding processes for thick steel plate	5
2.2.1	Development of welding processes	5
2.2.2	Development of welding techniques	12
2.3	Effect of welding parameters on weld metal microstructure and mechanical properties	13
2.3.1	Effect of welding parameters on heat input and cooling rate	13
2.3.2	Weld metal microstructure development	14
2.3.3	Effect of Ni on weldability and weld metal microstructure	19
2.4	Crystallographic evaluation in welds	21
Chapter 3	A novel approach to single-pass welding of square butt joints without edge preparation	25
3.1	Introduction	25
3.2	Materials, machines and methodology	25
3.2.1	Materials	25
3.2.2	Machines	26
3.2.3	Methodology	26
3.3	Calculations	28
3.3.1	Calculation of optimum hot-wire currents	28
3.3.2	Calculation of hot-wire fraction	29
3.3.3	Calculation of power consumption	30
3.4	Capability of gas metal arc welding process	30
3.4.1	Relationship between welding current and wire feeding speed ..	30
3.4.2	Arc phenomenon, bead appearance and weld geometry	31
3.5	Capability of hot-wire gas metal arc welding process	35
3.5.1	Relationship between hot-wire current and hot-wire feeding speed	35
3.5.2	Effect of hot-wire fraction on weld formation and weld geometry	36
3.6	Effect of hot-wire on cooling behavior and weld metal properties	38
3.6.1	Cooling profiles and obtained weld metal structure	39
3.6.2	Weld metal hardness	39

3.7	Production efficiency and power consumption	41
3.7.1	Production efficiency	41
3.7.2	Power consumption	41
3.8	Conclusion	43
Chapter 4	Optimization hot-wire fraction for enhance quality and precision of weld formation in GMAW process	44
4.1	Introduction	44
4.2	Materials and methodology	44
4.2.1	Materials	44
4.2.2	Methodology	45
4.3	Calculations	47
4.3.1	Calculation of hot-wire fraction	47
4.3.2	Calculation of power consumption	49
4.4	Compensatory condition	49
4.4.1	Arc phenomenon, bead appearance and weld geometry	49
4.4.2	Cooling profile and obtained weld metal structure	51
4.4.3	Mechanical properties of joint and power consumption	52
4.5	Limitation of hot-wire fraction	52
4.5.1	Arc phenomenon and bead appearance	52
4.5.2	Cooling profile and obtained weld metal geometry and microstructure	54
4.5.3	Mechanical properties of joint	55
4.6	Optimization condition	56
4.6.1	Arc phenomenon and bead appearance	56
4.6.2	Cooling profile and obtained weld metal geometry and microstructure	57
4.6.3	Mechanical properties of joint and power consumption	58
4.7	Advance microstructure evaluation	59
4.8	Conclusion	61
Chapter 5	An improvement of weld metal properties with selective hot-wire filler metal during GMAW process	62
5.1	Introduction	62
5.2	Materials and methods	62
5.2.1	Materials	62
5.2.2	Methodology	63
5.3	Effect of welding process on welded specimens	65
5.3.1	Arc phenomenon, bead appearance and weld geometry	65
5.3.2	Cooling profile and obtained weld metal structure	66
5.4	Effect of Ni content from hot-wire insertion on welded specimens	69
5.4.1	Bead appearance and weld geometry	69

5.4.2 Cooling profile and obtained weld metal structure	69
5.5 Conclusion	75
Chapter 6 Summary and future plan	76
Acknowledgements	78
Reference	79
Published or summited papers in regard to this thesis	91
Presentations	92

Chapter 1

Introduction

1.1 Research background

1.1.1 State of the art in welding technology

Welding is a critical joining process widely used in various industries such as construction, shipbuilding, and manufacturing, where the quality of welded joints is essential for the integrity of the final products [1-5]. Initially, welding processes were developed to achieve high productivity, often measured in deposition rate [6-8]. However, achieving high productivity using this approach frequently requires a high welding current and a larger diameter or multiple filler metals, as illustrated in Figure 1.1. Regrettably, high welding currents can lead to excessive heat input, resulting in the deterioration of joint properties, particularly in the heat-affected zone (HAZ) adjacent to the fusion line [7, 9-11]. There has been a shift towards developing welding processes that prioritized efficient heat control while maximizing joint quality, especially when welding thick steel plates [12-16]. This trend has driven the development of new welding techniques and technologies, including narrow gap welding, which can provide high-quality joints with controlled heat input, minimal distortion, and improved efficiency [17-19].

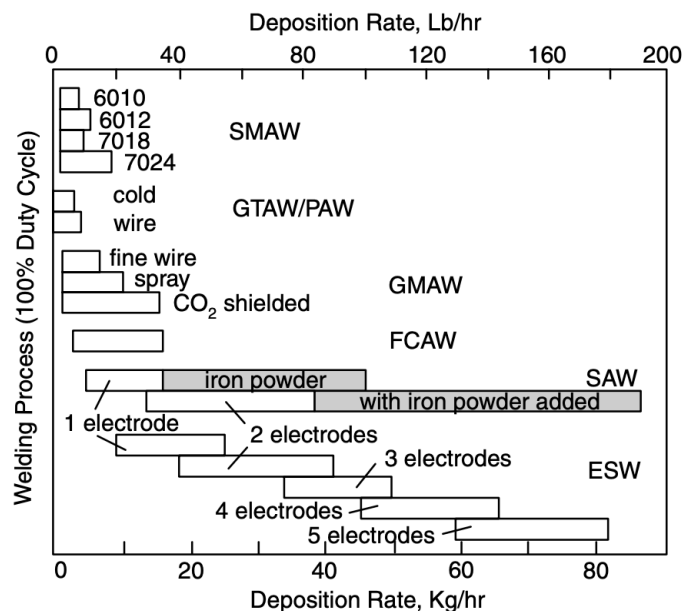


Fig. 1.1 Deposition rate in arc welding processes. (Reprinted from Kou [7])

1.1.2 Background of welded joint configuration

The evolution of welding technology has transformed the joint configuration and performed edge preparation, making welding practices more efficient and effective.

In the past, to achieve proper root penetration in thick steel plate joints, the complicated edge shapes required resource-intensive, time-consuming, and expensive. However, recent studies have shown the avoidance and reduction of complex edge shapes and larger gap sizes [20-25]. Figure 1.2 (a) depicts the conventional bevel types used to construct various butt joint types with corresponding deposition areas. Thanks to the advancements in welding technology, smaller gap sizes and deposition areas are now achievable, as illustrated in Figure 1.2 (b). This development has significantly impacted the welding industry, reduced the time and cost required for edge preparation, and ultimately increased productivity and efficiency.

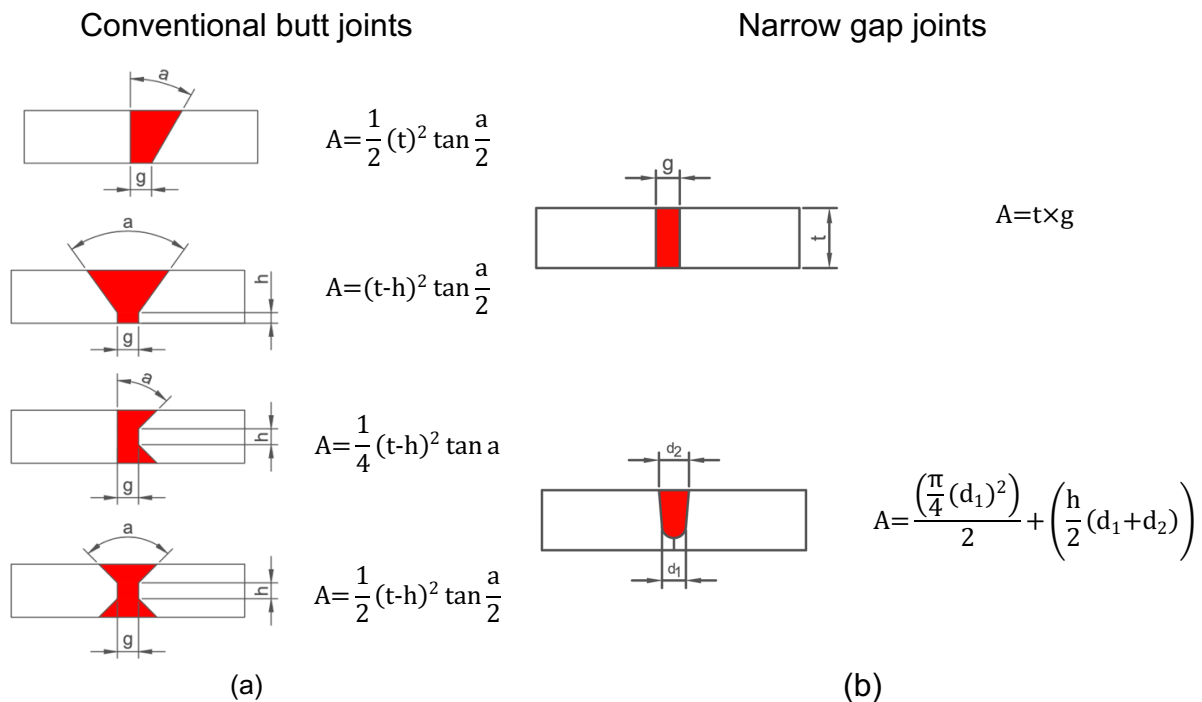


Fig. 1.2 Edge preparation and butt joint configurations.

1.1.3 Background of narrow gap welding and hot-wire technology

Narrow gap welding (NGW) is a specialized technique to join thick steel plates, pipes, and other materials requiring high structural integrity [23-28]. This technique involves creating a narrow gap, typically 5-10 mm, to reduce the need for filler metal and minimize heat input. Gas tungsten arc welding (GTAW) [23,25,26], gas metal arc welding (GMAW) [27-32], and submerged arc welding (SAW) [33-36] are suitable for NGW. Compared to conventional joints, NGW offers several advantages, including higher welding speeds, lower distortion, reduced fumes, and improved joint quality. However, it requires highly skilled operators, specialized equipment, and meticulous attention to detail, resulting in higher costs. While NGW provides significant benefits over conventional welding methods, productivity can improve by increasing the deposition rate using additional deposition volume, such as hot-wire insertion.

As previously mentioned, the hot-wire GMAW process can improve the productivity of NGW by increasing the deposition rate. In this study, the extra deposition volume from hot-wire fed into the narrow gap welding experiments to maintain the deposition rate with minimizing welding current and enhancing joint properties in subsequent experiments using selective filler wire. Figure 2.3 shows the capability of hot-wire GMAW. Although the hot-wire GMAW process requires a slightly higher welding current than conventional GMAW, it offers almost identical deposition volume to SAW while increasing productivity and reducing heat input.

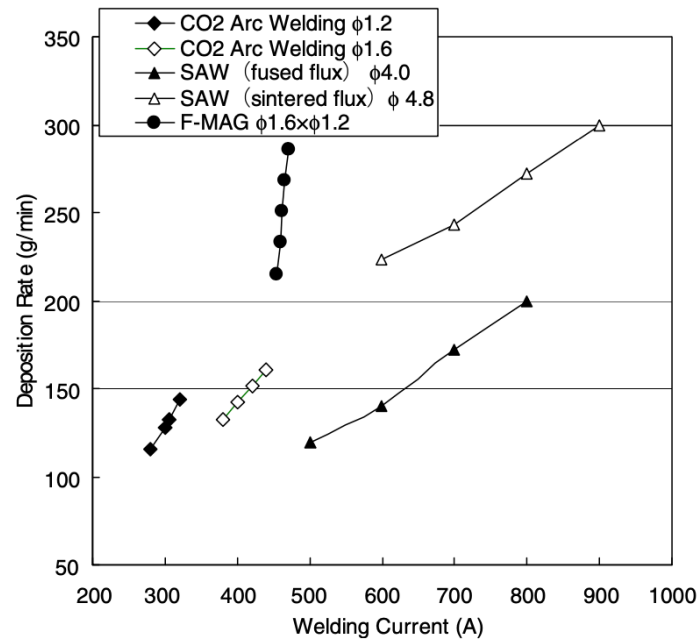
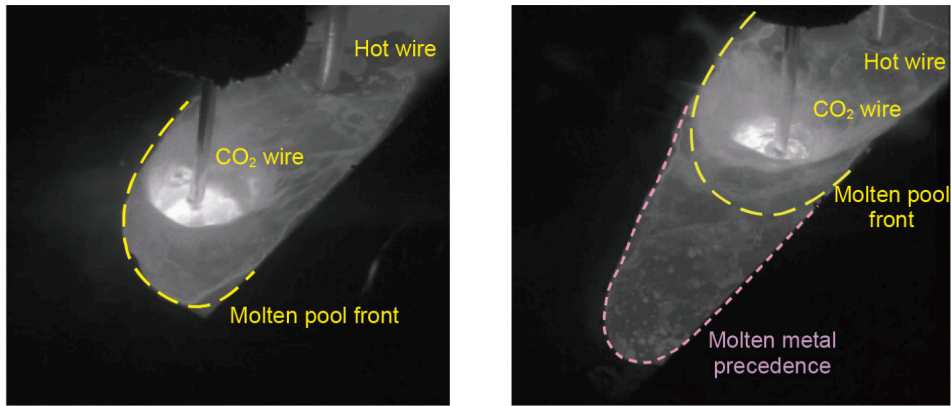
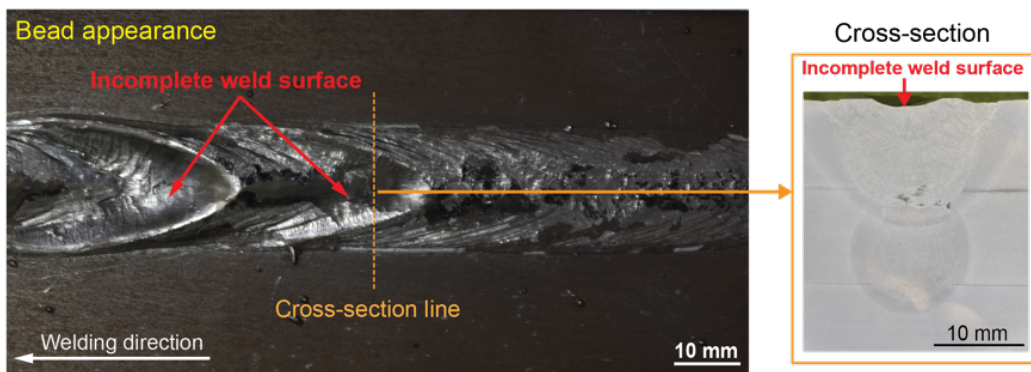


Fig. 1.3 Variation of deposition rate of weld metal with welding current under various welding condition. (Reprinted from Tsuyama et al [37])

However, some researchers reported the drawbacks of hot-wire GMAW. One such issue is the potential for excessive deposition rates can cause molten metal precedence [38]. This behavior is undesirable because the molten metal leads ahead of the molten pool and can cause irregular bead shapes and incomplete fusion, as shown in Figures 1.4 (a) and (b). Wonthaisong et al. [39,40] reported that the application of hot-wire GMAW led to higher weld metal hardness and lower toughness as illustrated in Figure 1.5 (a) and (b). In contrast, Tsuyama et al. [37,41] showed better joint properties of hot-wire GMAW over conventional GMAW. Using hot-wire insertion induced more acicular ferrite fraction because more non-metallic inclusion rose. To be addressed this, a systematic investigation was designed not only to explain on the production side but also on the metallurgical side. The weld metal microstructures were investigated using the heat history during melting and solidification. A detail studied the relationship between welding parameters and the obtained weld geometry was performed. Not only improving the controllability of molten pool formation but also achieving soundness joints and enhancing joint properties were set as primary goals of this dissertation.

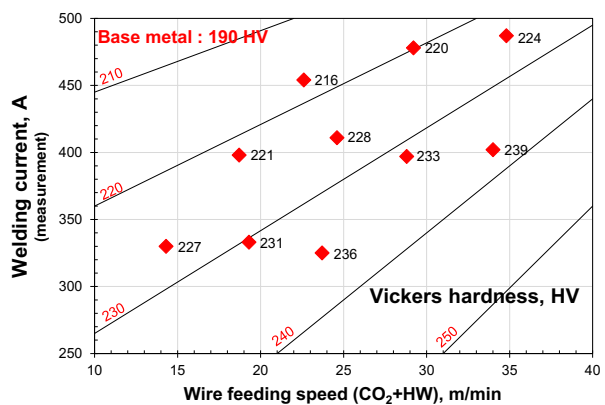


(a) Molten metal precedence

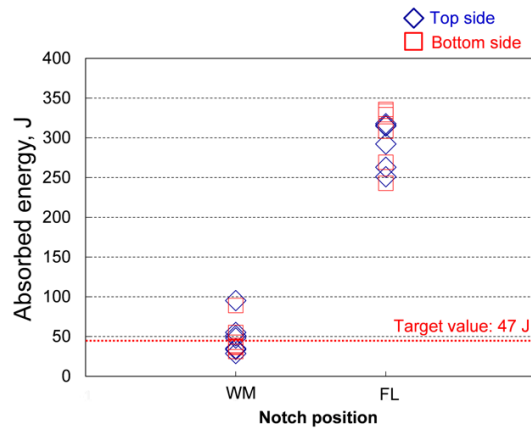


(b) Irregular bead shape

Fig. 1.4 Molten metal precedence leads poor bead appearance. (Edited and reprinted from Wonthaisong et al [38])



(a) Effect of hot-wire volume on weld metal hardness [39]



(b) Effect of hot-wire volume on absorption energy. [39]

Fig. 1.5 Effect of hot-wire volume on mechanical properties. (Reprinted from Wonthaisong [39])

1.2 Objectives and construction of the dissertation

The hot-wire GMAW process offers exceptional deposition volume without excessive power consumption, reducing the number of weld passes required and increasing process tolerance. Considering these benefits, this dissertation aims to achieve three objectives: first, to develop a single-pass welding method using hot-wire GMAW on 15-mm thick steel plate square butt joints without edge preparation; second, to conduct a systematic study on hot-wire insertion to determine the optimal hot-wire fraction and maximum deposition efficiency during GMAW; and last, to enhance joint properties using selective hot-wire filler metal during GMAW. Achieving these objectives will contribute to the advancement of hot-wire GMAW technology and its practical applications in welding.

Figure 1.6 shows the structure of this dissertation. Chapter 1 provides a summarized research background, objectives, and dissertation statements.

Chapter 2 reviews literature related to the evolution of hot-wire GMAW process, the effect of chemical composition on weld metal structure, and the theoretical basis for the experiments conducted in this dissertation.

In Chapter 3, the determination of GMAW process capability on square butt joints. The optimal hot-wire current for this application was determined. The elucidation of hot-wire GMAW on single-pass welding of 15-mm thick steel plate square butt joints without edge preparation. The power consumption and production efficiency of this novel process were proposed.

Chapter 4 uses the optimal hot-wire current and welding parameters determined in Chapter 3 to compensate for total deposition volume to create a soundness joint. I proposed the limitation of hot-wire fraction for a single-v butt joint by showing the limit of process and metallurgical. The optimized conditions can create a soundness condition for 20-mm thick steel plates while minimizing power consumption (62% reduction compared with conventional GMAW).

In Chapter 5, I proposed the novel application of hot-wire insertion using a selective hot-wire to improve the joint properties. The effect of nickel content was determined using the mentioned high controllability of the insertion method. The results found that more nickel content induces more acicular ferrite fraction and suppresses grain boundary ferrite fraction and Widmanstätten ferrite fraction, which results in better joint properties.

Finally, Chapter 6 presents the conclusions of this dissertation and suggests future work.

Chapter 1: Introduction and research objectives



Chapter 2: Literature review



Chapter 3: A novel approach to single-pass welding of square butt joint without edge preparation

- The limitation of conventional GMAW on square butt joint of 15-mm thick steel plate
- The optimum hot-wire current for precise deposition rate control
- Analysis of the joint properties, including mechanical and metallurgical characteristics, of the weld metal from hot-wire GMAW



Chapter 4: Optimization hot-wire fraction for enhance quality and precision of weld formation in GMAW process

- The compensatory total deposition rate using hot-wire insertion and its effect on weld metal properties
- Limitations of using hot-wire fraction in terms of metallurgy and processing side
- The optimized conditions to create a sound joint condition of 20-mm thick steel plate using only 2 weld passes with minimal power consumption



Chapter 5: An improvement of weld metal properties with selective hot-wire filler metal during GMAW process

- Effect of hot-wire fraction with hot-wire GMAW on solidification characteristics, weld metal structure, and mechanical properties
- Effect of Ni content from hot-wire insertion on the fraction of weld metal microstructure such as acicular ferrite, grain boundary ferrite, and Widmanstätten ferrite



Chapter 6: Summary and Future work

- Summary of the main findings and contributions of the dissertation
- Suggestions for future research directions.

Fig. 1.6 Construction of the dissertation

Chapter 2

Literature review

2.1 Introduction

This chapter presents a comprehensive literature review of the hot-wire Gas metal arc welding process (GMAW) and its practical applications. It begins by summarizing the evolution of arc welding processes for welding thick steel plates with maximum efficiency and minimal heat input. The discussion then draws out the hot-wire GMAW process, providing a detailed examination of its principles and characteristics. Specifically, the chapter explores the formation of the weld metal structure and its impact on the mechanical properties of the joint, including strength and toughness. The chapter investigates the potential benefits of using selective hot-wire filler metals with higher Ni content to improve weld metal toughness. This literature review establishes a strong foundation for the experimental work in the following chapters, ultimately contributing to the advancement of hot-wire GMAW technology and its practical applications in welding.

2.2 Evolution of arc welding processes for thick steel plate

2.2.1 Development of welding processes

Welding has become the primary method for joining steel in various construction fields because of its high joint efficiency and productivity. In Chapter 1, we briefly discussed the evolution of welding processes, which developed based on the required deposition rate for enhanced productivity. For heavy thick steel plates used in shipbuilding, bridge construction, and offshore structures, welding processes capable of handling thicker plates were needed [1-9].

Figure 2.1 shows the required number of welded passes for manual and semi-automatic processes, such as GMAW [42], shielded metal arc welding (SMAW) [43], and flux-cored arc welding (FCAW) [44] when performed on butt-joints of thick steel plates. High deposition rate processes such as submerged arc welding (SAW) required significantly fewer weld passes. However, SAW is susceptible to the problem of high heat input [7-9], leading to wider Heat-Affected Zones (HAZ) [7-14], as illustrated in Figure 2.2 (a). Low heat input welding processes such as laser beam welding (LBW) [46-48] and electron beam welding (EBW) [49-51] are the solutions. Figures 2.2 (b) and 2.2 (c) show the etched cross-sections of the welded joint subjected to LBW and EBW, respectively, requiring fewer welded passes and resulting in a narrower HAZ. Despite the desirable results, these processes are expensive and require complicated setups, high precision of joint configuration, and strict safety precautions, making them less workable for practical use. Figure 2.3 illustrates the comparative cost of laser welding with arc and gas welding.

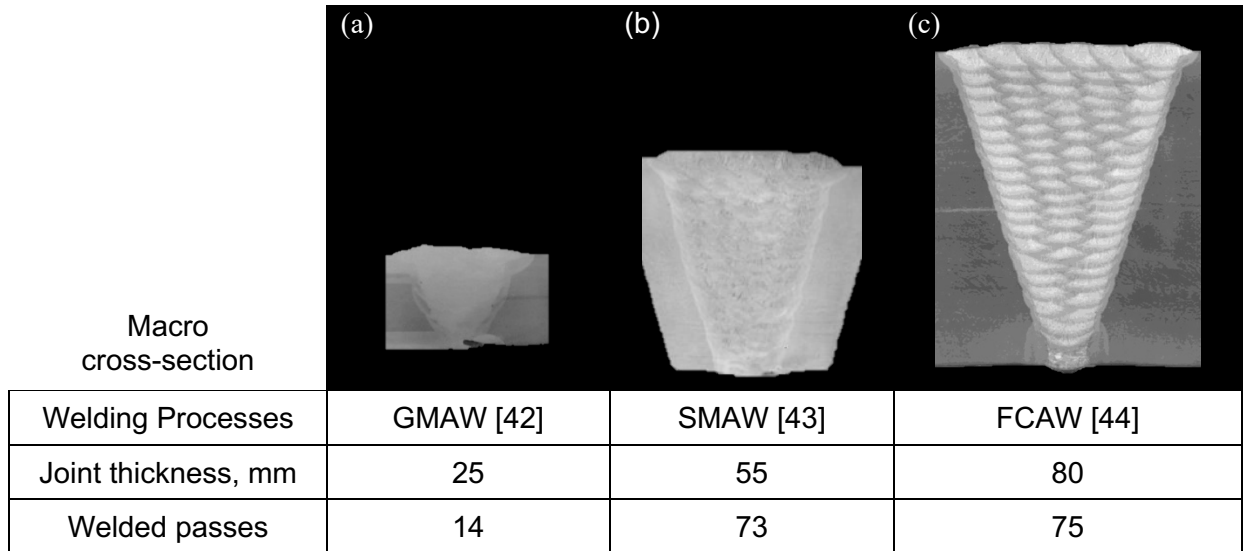


Fig. 2.1 Increasing required number of weld pass as thickness increased. (Edited and reprinted from Devaney et al [42], Song et al [43], Kartel et al [44])

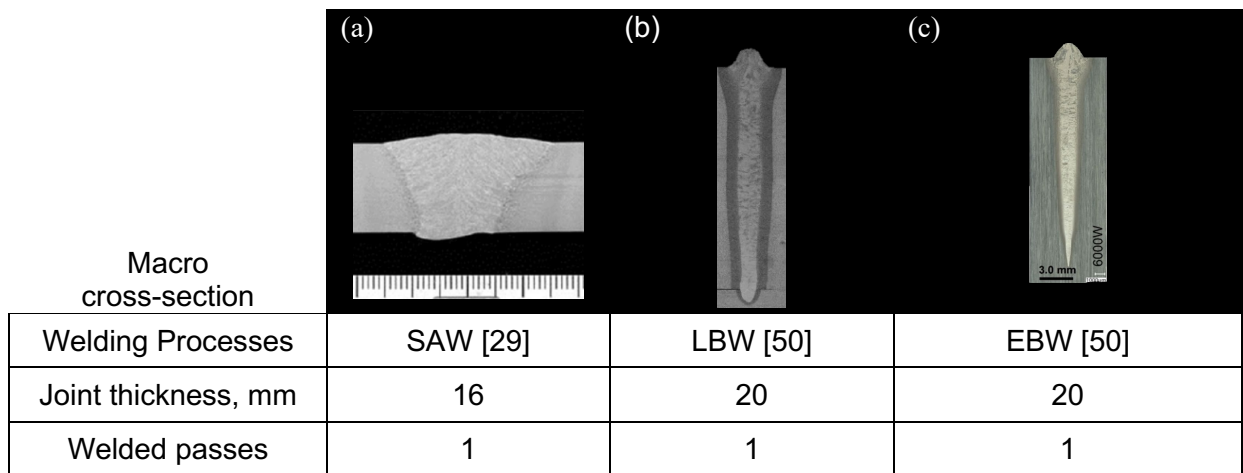


Fig. 2.2 Single pass welding even as thickness increased. (Edited and reprinted from Bao et al [29], Elmer et al [50])

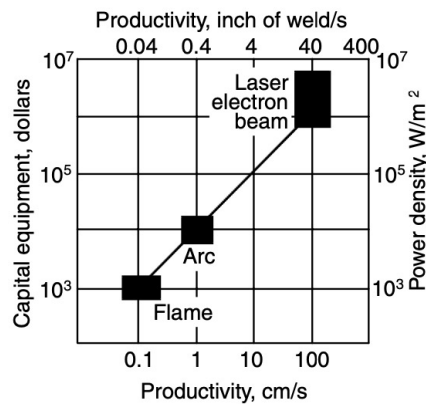


Fig. 2.3 Capital equipment cost vs. productivity. (Reprinted from Kou [7])

A Hot-wire insertion system was originally designed to assist the low deposition volume of GTAW [4]. The mechanism of hot-wire illustrates in Figure 2.4. At the initial state, the wire fed through the contact tip. Then it contacted the base metal surface where the closed-loop electrical circuit started. The wire was heated by electrical flow through the filler metal under Joule heating phenomena [25] until its melting temperature. Shinozaki et al. [25] proposed the calculated model to explain the relationship between the required hot-wire current and wire feeding speed in GTAW. Wonthaisong et al. [38,40] applied the calculation for hot-wire GMAW resulting in soundness joints of a 20-mm thick steel plate. Moreover, Zhu et al. [52] proposed equations to explain the relationship between hot-wire current and hot-wire feeding speed of different filler metals to extend the welding process tolerance. Figure 2.5 shows the suitable hot-wire currents of filler metals for wire feeding speed varied between 5 to 20 m/min.

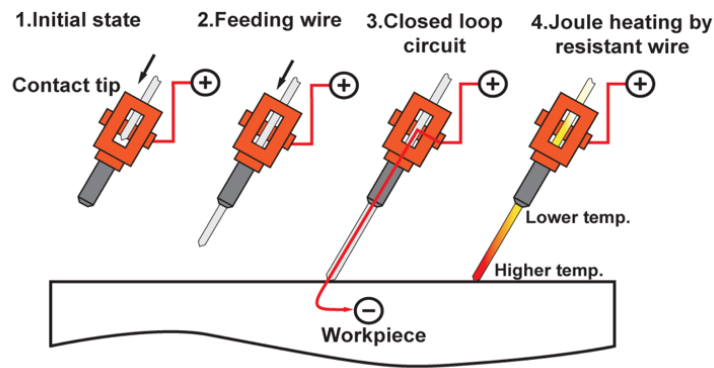


Fig. 2.4 Schematic of a hot-wire system. (Reprinted from Rittichai et al [22])

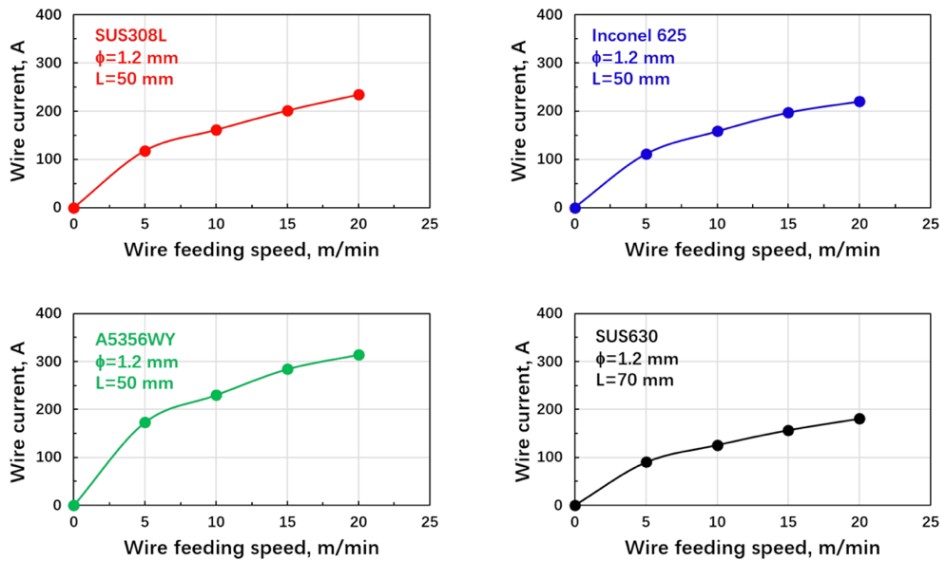


Fig. 2.5 Suggested hot-wire currents for (a) SUS308L (b) A5356WY (c) Inconel 625 and (d) SUS630. (Reprinted from Zhu et al. [52])

The development of welding thick steel plates has become more challenging. The primary goal is to maximize deposition volume while minimizing power consumption. To create a clear picture, the author reviewed and compared the productivity of several welding processes by plotting their relationship between deposition volume and required power consumption, as shown in Figure 2.6. SAW provided an extremely high deposition volume but required significant power consumption. In contrast, Baba et al. [36] modified GMAW using pure carbon dioxide as the shielding gas during a high arc current showing a high current CO₂ welding process resulting in a buried arc with high deposition volume and no spatter. Meanwhile, Tsuyama et al. [22] demonstrated a combination of hot-wire and GMAW processes, named "F-MAG," which provided almost identical deposition volume to SAW but required less power consumption, increasing productivity and reducing heat input to the workpieces.

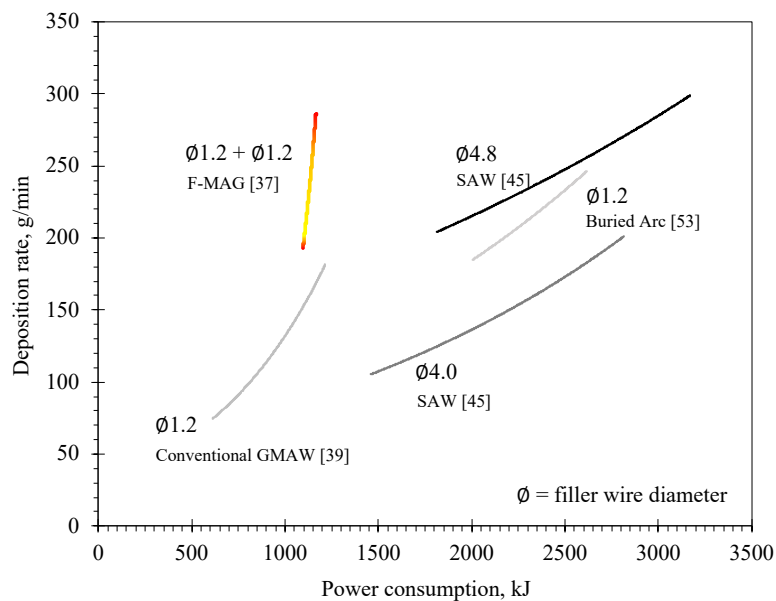


Fig. 2.6 Deposition rate vs. required energy consumption. [37, 39, 45, 53].

The hot-wire insertion has been used in various application but mostly is used to increase the deposition rate. Tsuyama et al., [45] reported the application of hot-wire in SAW which can increase deposition rate while required less welding current compare to tandem SAW as in Figure 2.7. A comparison of similar welded joint configurations between solo GMAW and hot-wire GMAW, where the number of welded passes significantly reduced shown in Figure 2.7. Kadoi et al. [54] showed the optimized condition between hot-wire insertion and laser welding in fillet joint. Kim et al. [55] using the reverse polarity technique for hot-wire in tandem arc welding to reduce the arc deflection resulting in wider and deeper molten pool. Marumoto et al., [56] successfully controlled bead shape using hot-wire insertion in GMA laser hybrid welding.

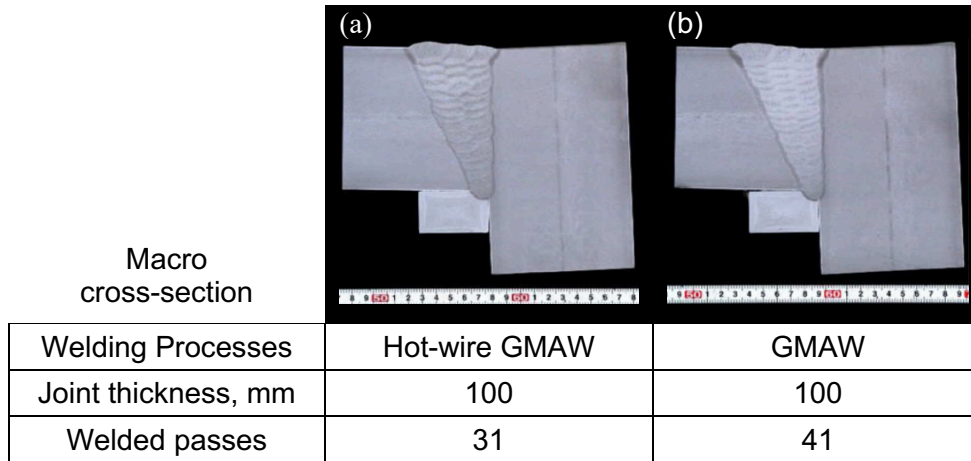


Fig. 2.7 Corner joint with and without hot-wire insertion. (Edited and reprinted from Tsuyama et al. [45])

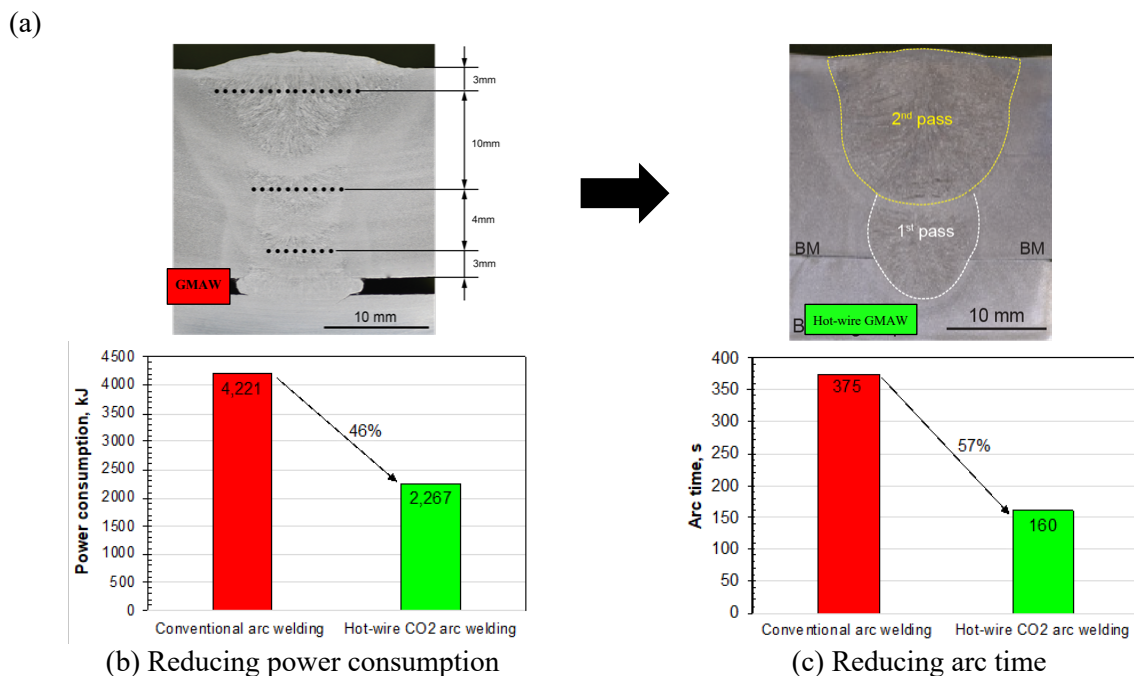


Fig. 2.8 Advantages of hot-wire: (a) Reduce of weld passes, (b) Reduce power consumption, (c) Reduce arc time. (Edited and reprinted from Wonthaisong [39])

Hot-wire GMAW has been continuously developed to maximize its efficiency and productivity. Wonthaisong et al. [38-40] successfully optimized hot-wire parameters to maximize the deposition rate during hot-wire GMAW. Figure 2.8 (a) shows that a single-v groove butt joint of 20-mm thick steel plate could be welded using only two weld passes. By using hot-wire GMAW, power consumption can be reduced by up to 46%, as illustrated in Figure 2.8 (b), and reduced about 57% of arc time, as depicted in Figure 2.8 (c) This emphasized the potential of the hot-wire insertion to ensure the weld quality in butt joint narrow gap single pass welding

without edge preparation and the author believes that this benefit can be used for sustainable development of this dissertation.

2.2.2 Development of welding techniques

The previous topic already exposed the development of hot-wire welding to increase the deposition rate while minimizing power consumption. However, the joint configuration techniques revolutionized as the welding processes developed. The narrow gap (NG) technique was applied to various welding processes. Ming et al. [57] used NG instead of conventional v-grooved and double v-grooved to reduce the amount of weld metal and lower heat input for dissimilar welding between SA508 Gr.3 and 316L stainless steel using Inconel 52 filler metal. Wang et al. [58] proposed a novel alternating magnetic field-assisted low-frequency pulse GTAW in narrow gap welding to create an arc characteristic and arc weaving. Traidia et al. [59] suggested the suitable welding parameter for a horizontal welding position of NG-GTA welding. Guo et al. [60] studied the microstructure evolution and mechanical properties of S960 high-strength steel using NG-laser welding. The NG-laser welding joints provided better tensile strength but less impact toughness over the GMAW joints. Kim et al. [61] used the NG configuration instead of the butt joint double-v groove and qualified for the ballistic test of combat vehicle steel. Abe et al. [62] established NG-SAW technology and suggested appropriate welding conditions. Balakrishnan et al. [51] studied the residual stress distribution of four welding processes, SAW, GTAW, laser, and electron beam welds, in 30 mm thick SA508 steel NG welding. The weld macrographs shown in Figure 2.9 revealed that the NG techniques reduced filler metal consumption and minimized the number of required weld passes. This comparison highlights the potential of NG, which enables single-pass welding with no edge preparation when combined with hot-wire insertion, revolutionizing the joining process.

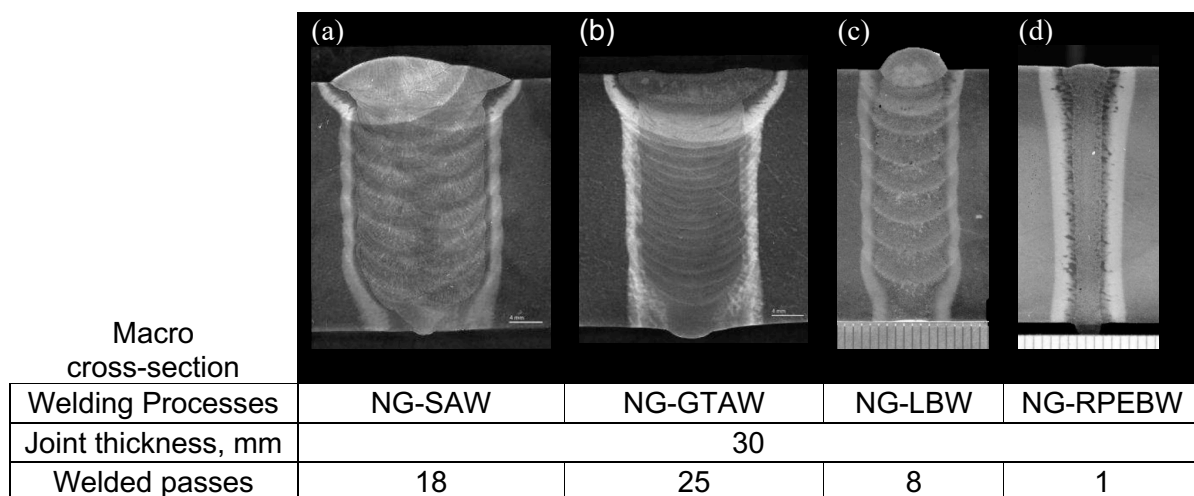


Fig. 2.9 Cross-Sectional Views of Narrow Gap Welding with Various Processes (Edited and reprinted from Balakrishnan et al [51]).

Maruyama et al. [63-65] summarized the wire feeding method in a NG welding. Figure 2.10 illustrates the different mechanical bending or rotating apparatuses employed to bend the wire and control the oscillation frequency. These techniques are used to ensure proper wire feeding and manipulate the arc movement during the NG welding process. In this dissertation, the author employed a simple weaving method in order to reduce the complexity and costly equipment.

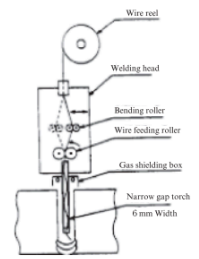
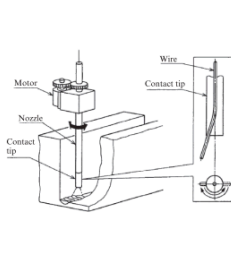
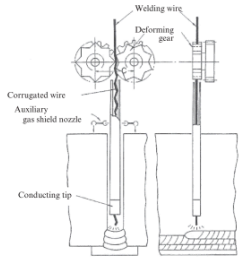
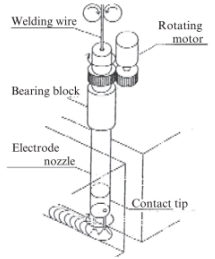
Method	(a) Wave-shaped wire	(b) Bent tip	(c) Curved tip	(d) High speed rotating arc
Principle of welding machine				
Groove width	Groove width : 9 mm (8–14) Torch : 6 mm <i>t</i> -35 mm <i>w</i>	16 (15–20) mm Nozzle : ϕ 8 mm	11–13 mm Torch : 8 mm <i>t</i> -65 mm <i>w</i>	12–18 mm Nozzle : ϕ 8 mm
Standard welding conditions	Wire diameter : 1.2 mm Arc current : 240 A, Pulsed Welding speed : 210 mm/min Shielding gas : 20% CO ₂ -Ar	1.2 mm 110–180 A, Pulsed 150–180 mm/min 20% CO ₂ -Ar	1.2 mm 260–270 A, Pulsed 210 mm/min 20% CO ₂ -Ar	1.2 mm 300–350 A 220–300 mm/min 20% CO ₂ -Ar
Weaving frequency	0.5–1.5 Hz Amplitude adjustment is easy.	0.2–0.6 Hz Amplitude adjustment is easy.	4–15 Hz Wire bending width: 2–4 mm	Max. 150 Hz Rotating diameter: 7.6 mm
Features	• Oscillates at low speed in straight lateral direction	• Reproduces the movement of experienced welders by detailed control	• Simple and high reproducibility oscillation mechanism	• Easy seam tracking by utilizing arc voltage

Fig. 2.10 Oscillation in narrow gap welding. (Reprinted from Maruyama et al. [63])

2.3 Effect of welding parameters on weld metal microstructure and mechanical properties

2.3.1 Effect of welding parameter on heat input and cooling rate

Welding is a complex process involving the application of heat and pressure to join metal parts [4-6]. In arc welding processes, an electric arc generates heat that melts the base metal, forming a molten pool. The heat input, which depends on welding current, voltage, travel speed, and electrode diameter, is a critical parameter for producing sound welds with desired mechanical properties.

Heat input plays a crucial role in determining the quality and mechanical properties of the weld joint. Heat input means the amount of heat energy supplied to the workpiece per unit length of the weld. During welding, heat input influences the cooling rate, which, in turn, affects the microstructure and properties of the weld metal. The calculation of heat input in arc welding processes can calculate using the following equation $HI = [(E \times I) / V]$ Where HI is heat input, in Joules per millimeter, E

is applied arc voltage during welding, in Volt, I is the applied welding current during welding, in Ampere, V is travel speed, in millimeters per second [7, 66].

The influence of heat input on the cooling profile of weld metal during the GTAW of 2024 aluminum depicted in Figure 2.11 (a). Funderburk [66] illustrated the relationship between heat input, cooling rate, and cooling time in Figure 2.11 (b). Peng et al. [67] evaluated the microstructure of TMCP890 under different temperature histories and showed that high heat input deteriorated the weld metal and adjacent area properties. The first goal of this study is to achieve single-pass welding for square-butt joints without edge preparation while maintaining fast travel speeds. This approach aims to minimize the impact of heat input on the properties of the weld metal and the heat-affected zone (HAZ).

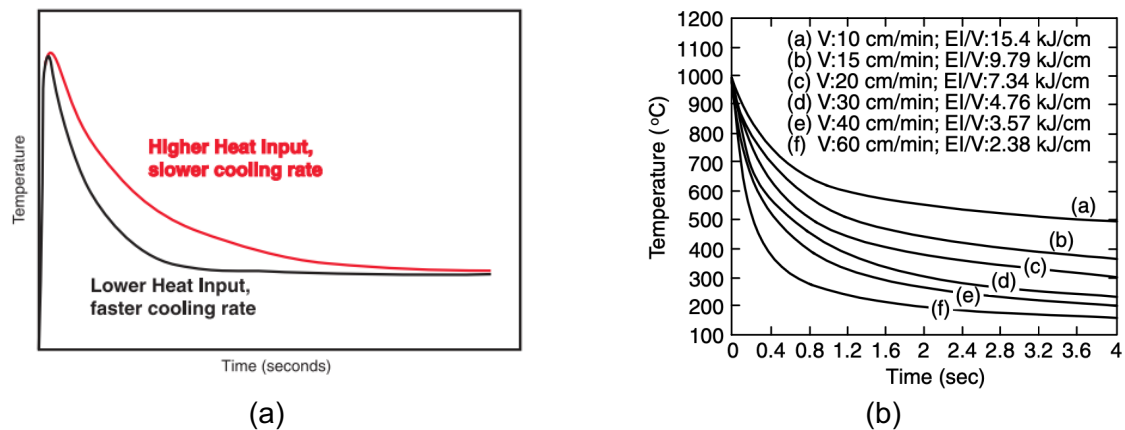


Fig. 2.11 Variation in cooling rates with heat input per unit length of weld; (a) Heat input and cooling rate (Reprinted from Funderburk [66]); (b) increasing welding speed (Reprinted from Kou [7])

2.3.2 Weld metal microstructure development

The author summarized the microstructure development in weld metal using the continuous-cooling transformation (CCT) diagram and illustrated the transverse cross-section of weld metal at different cooling stages. The arc temperature can increase to 2500K and generate a molten pool. David et al. [68] explained that during 2000-1700°C, the 0.1-1.0 μm of complexed oxide inclusions were distributed in the molten pool liquid. These inclusions are the product of dissolved oxygen and deoxidizing elements reactions upon the thermodynamic properties of liquid metal, gas, and slag phases illustrated in Figure 2.12 (a). Babu [69] proposed that during 1700-1600°C, the delta-ferrite starts solidification surrounding the oxide inclusions and transforms to austenite, as illustrated in Figure 2.12 (b). Then, the austenite grain may grow during the temperature range from 1600-800°C, as in Figure 2.12 (c). These austenites decompose to different ferrite morphologies during cooling

from 800 to 300°C. Figures 2.12 (d) and (e) illustrated the formation of allotriomorphic ferrite at the prior austenite grain boundary called grain boundary ferrite (GBF). Kou [7] defined it as a ferrite without a regular faceted shape reflecting its internal crystalline structure. With continued cooling, the mobility of the planar growth front of the GBF decrease, and the Widmanstätten ferrite or side-plate ferrite (SPF) forms at the ferrite-austenite boundaries as illustrated in Figure 2.12 (f). Substitutional atoms do not diffuse during the growth of SPF. With the even lower temperature, an insufficient driving force for SPF to grow inwards. The new ferrite nucleates ahead of the growing ferrite. Acicular ferrite nucleates at inclusion surface particles and randomly forms oriented short ferrite needles [7, 69], as illustrate in Figure 2.12 (g). Grong et al. [70] arranged the microstructure formed within austenite grain by transformation temperature as grain boundary ferrite (GBF), polygonal ferrite, Widmanstätten ferrite or ferrite side plate (FSP), upper bainite, lower bainite, and martensite. Figure 2.13 (a) and (b) showed ferrite morphologies in weld metal.

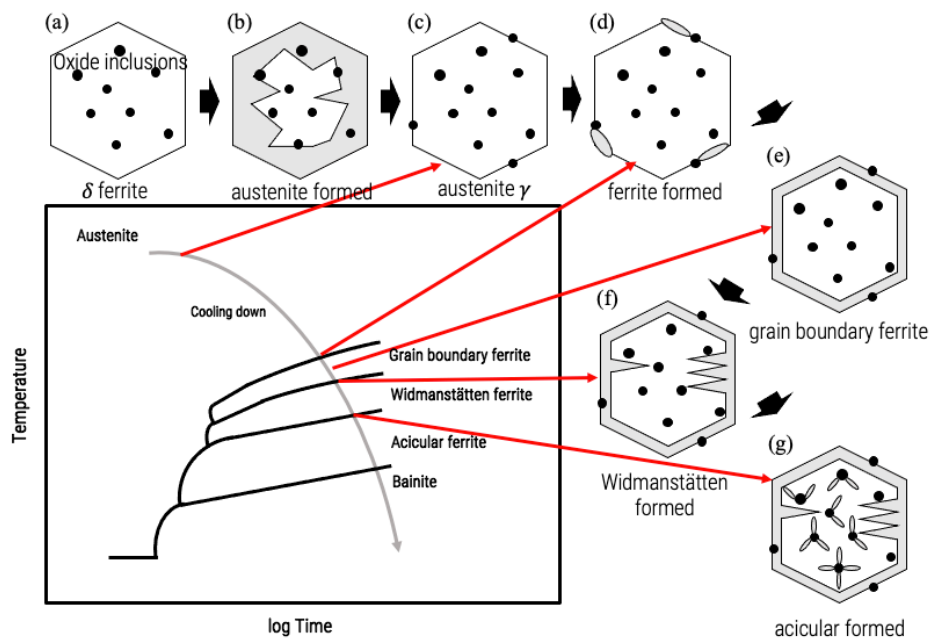


Fig. 2.12 CCT diagram for low carbon steel weld metal: (a) Oxide inclusions in weld metal liquid; (b) δ ferrite occurred and transformed to austenite; (c) full austenite; (d), (e) grain boundary ferrite developed; (f) Widmanstätten ferrite formed; (g) Acicular ferrite occurred (Edited from Kou [7], Babu [69], Onsøien et al. [71])

Figure 2.14 (a) represents the predominant acicular ferrite in low-carbon steel weld metal. Figure 2.14 (b) shows the inclusions surrounded by acicular ferrite [69]. AF nucleates heterogeneously on the surface of inclusions during the austenite-ferrite transition. As the transformation progresses, ferrite grains radiate in various directions, forming a fine-grained and interlocking structure of AF, with plate lengths of approximately 5-15 μm and widths of 1-3 μm . This chaotic structure significantly impedes the propagation of cleavage cracks, leading to improved mechanical properties, especially toughness.

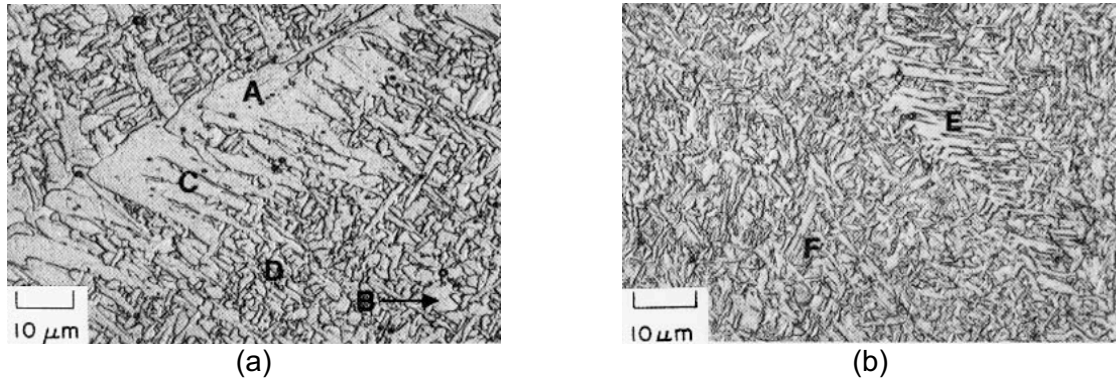


Fig. 2.13 Microstructure of low carbon steel weld metal; (a) GBF A, Polygonal ferrite at B, SPF at C, AF at D; (b) Upper bainite at E and Lower bainite at F (Reprinted from Grong et al [70])

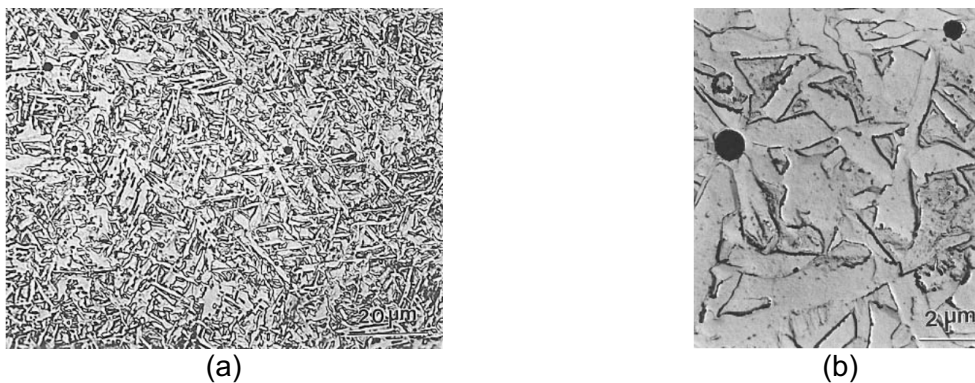


Fig. 2.14 Acicular ferrite; (a) predominately AF of a low carbon and low alloy steel weld. (b) AF and inclusion particle. (Reprinted from Babu et al. [69])

Aaronson et al. [72] defined “Widmannstätten star” to describe a microstructure of intragranular nucleated, chaotically arranged needle-shaped ferrite grains and later named acicular ferrite (AF) by Smith et al. [73]. Dr. Edgar C Bain discovered the Bainite structure during his research on the isothermal transformation of austenite [74]. AF plays a vital role in enhancing the toughness of steel, making it a subject of extensive research [75-77]. Shao et al. [75] summarized the mechanism of AF formation in high-strength and low-alloy steel, highlighting its significant role in improving strength and toughness. Wang et al. [76] explored the application of TiC-TiB₂ nanoparticles in as-cast low-carbon steel, which effectively limited the formation of FSP, reduced grain size, increased pearlite content, and simultaneously improved yield strength, tensile strength, and ductile. However, Cho et al. [77] critically assessed the current understanding of AF formation, emphasizing the need for more intensive studies to establish a comprehensive theory. AF remains a promising microstructure with the potential to enhance the combination of strength, toughness, and fatigue properties in the weld metal. Loder et al. [78] summarized the different characteristics between AF and bainite as in Table 2.1.

Table 2.1 Characteristics of acicular ferrite and bainite [78]

Phase	Acicular ferrite	Bainite
Nucleation	intragranular	inter- or intragranular
Nucleation site	point sites (inclusion surface)	mostly austenite grain surface
Transition temperature		similar
Grain form	needle-shaped/lenticular plates	Fine laths which form sheaves
Growth direction	various direction (star-like)	parallel lath
Parallelism	cannot form parallel lath	Lath are parallel within package
Growth mechanism		diffusionless
Growth stop reason		C-enrichment of austenite or impingement

Loder et al. [78] proposed that the formation of AF occurs without diffusion, causing the ferrite plates to become supersaturated with carbon. Islands of retained austenite may be present in the final microstructure if the austenite does not convert. The remaining carbon-enriched austenite transforms into martensite, bainite, or pearlite. Pearlite and bainite form at low and medium cooling rates. At high cooling rates, the remaining austenite transforms into martensite. The alloying additions such as carbon, silicon, and nickel affect the fraction of remaining austenite.

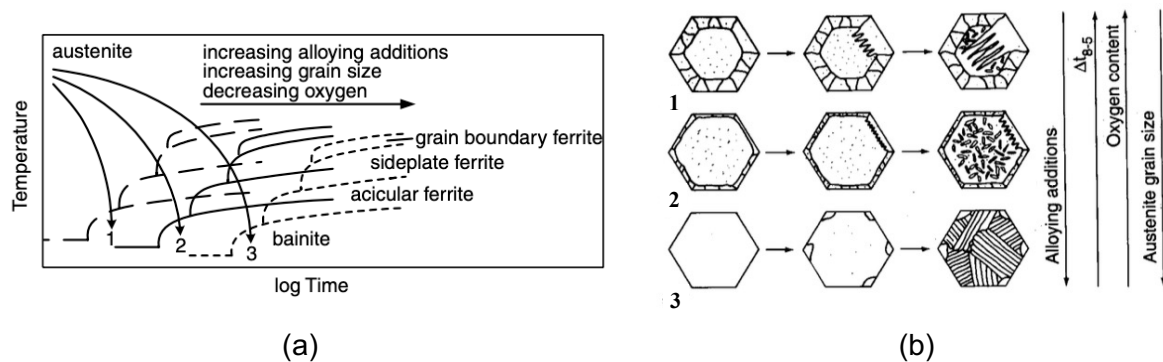


Fig. 2.15 Effect of alloy additions, cooling time, weld oxygen content, and austenite grain size on: (a) CCT diagram for weld metal of low carbon; (b) Schematic of grain development in weld metal. (Edited and reprinted from Kou [7])

Figure 2.15 (a) illustrates the impact of alloy additions, oxygen content, and austenite grain size on the CCT diagram for low-carbon weld metal [79]. It also shows that the CCT curve shifts towards longer times and lower temperatures. Rees et al [80] found that increasing the cooling rate results in a finer acicular ferrite structure due to higher supercooling and the resulting increase in the reaction driving force, which leads to a higher nucleation rate. As a result, numerous AF plates nucleate, limiting their growth space and resulting in finer structures. The vertical arrows indicate the effect of these factors. As the cooling rate slows down ($\Delta T_{8/5}$ increases) without effect from other parameters, the obtained structures will change from predominate bainite, Fig. 2.15 (b) mode 3 to predominately AF as in Fig. 2.15 (b) mode 2 and with the slowest of curve 3, predominate GBF and Widmanstätten ferrite could be obtained as in Fig. 2.15 (b) mode 1. The quantitative

studies from Lv et al. [81] clearly showed the effect of the cooling rate, prior austenite grain size, and nucleation density on AF sizes illustrated in Figure 2.16.

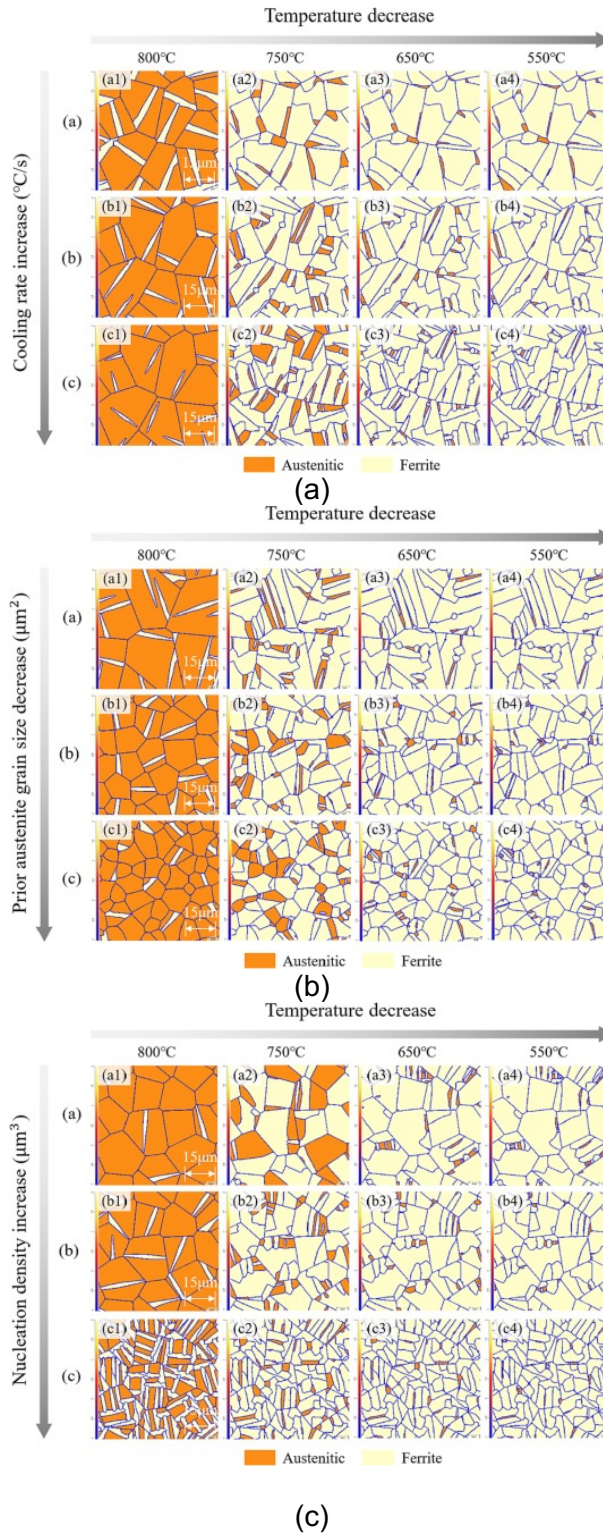


Fig. 2.16 Influence of (a) Cooling rate; (b) Prior austenite grain size; (c) Nucleation density on the evolution of austenite-AF microstructure transformation (Reprinted from Lv et al. [81])

Loder et al. [78] summarized the effect of austenite grain size on AF that the increasing austenite grain size reduces the grain boundary area available for ferrite nucleation, shifting the CCT curves towards longer times and lower temperatures. Phase transformation involves either homogeneous or heterogeneous nucleation. Heterogeneous nucleation is more likely due to reduced energy at interphase surfaces. Thus, during the austenite-ferrite transition, ferrite grains tend to nucleate heterogeneously on non-metallic inclusions (such as AF) or grain boundaries (e.g., Widmanstätten ferrite and GBF). Intragranular nucleation is favored with larger austenite grain size or more inclusions, while grain boundary nucleation becomes more likely with smaller grain or fewer inclusions. Oxygen content is another factor that affects the development of weld metal. Oxygen can be added to the weld metal from several methods as a shielding gas [71] or fluxes [82]. However, this oxygen content increased the inclusion volume fraction resulting in more AF fraction in the weld metal [71]. Similar to the report from Xu et al. [83] that the oxygen content in weld metal from the GMAW process led to more AF fraction and can increase the joint properties.

2.3.3 Effect of Ni on weldability and weld metal microstructure

The author separated this section to discuss only the effect of alloying elements intentionally added into the weld metal to improve the joint properties, especially Ni. The number of additional elements to improve the joint properties is limited to its weldability because excessive alloying element leads to deterioration of the properties. Talas [84] proposed the carbon equivalent equation proving the best scoring to predict the weld metal properties compared with several equations. Table 2.2 provides carbon equivalent equations where Ni shows less negative effect on the weldability among other multiplying factors.

Table 2.2 Carbon equivalent formulars [83-88]

Carbon equivalent provider	Formulars
CE _{WM} [84]	$C + (Mn + Cr + V + Si)/6 + (Mo/4) + (Nb/9) + (Ti/3) + (Cu/20) + (Ni/25) + 5B$
CE _{DI.1} [85]	$C + (Mn + Si)/6 + (Cr + Mo + V)/5 + (Ni + Cu)/15$
CE _{IIV} [86]	$C + (Mn/6) + (Cr + Mo + V)/5 + (Ni + Cu)/15$
P _{cm} [87]	$C + (Si/30) + (Mn + Cu + Cr)/20 + (Ni/60) + (Mo/15) + (V/10) + 5B$
CE _{WES} [88]	$C + (Mn/6) + (Si/24) + (Ni/40) + (Cr/5) + (Mo/4) + (V/14)$

Nickel is the only alloying element that improves strength and toughness properties simultaneously without negative weldability [89]. The significant extension of the austenite phase field by nickel alloying combination with its low diffusivity in the austenite lattice delays the austenite-to-ferrite transformation towards lower temperature or extended time. Wang et al [90] proposed that the increase of Ni content from 0.37%wt to 1.45%wt, AC1, and AC3 temperatures were reduced from

708°C and 823°C to 689°C and 802°C, respectively. Andrew [91] proposed the empirical equation to calculate the transformation temperature presented in Table 2.3. The resulting undercooling causes an increased ferrite nucleation rate and decreases the ferrite growth rate leading to a general refinement of the ferrite microstructure. Figure 2.17 shows the influence of nickel alloy content on the transformation behavior of low-carbon steels. However, several researchers [92-94] reported that excessive Ni content results in less AF fraction. Mohrbacher et al [89] concluded that the Ni content is limited by Mn content. The Mn content within 0.5 to 1.0%wt, while Ni remains at 4.0 to 5.0%wt, was recommended to achieve high weld metal toughness and prevent the risk of intergranular fracture.

Table 2.3 Critical transformation temperature AC1 and AC3 [91]

Critical temperature	Formulars
AC1	$723 - 10.7Mn - 13.9Ni + 29Si + 16.9Cr + 290As + 6.38W$
AC3	$910 - 203\sqrt{C} - 15.2Ni + 44.7Si + 104V + 31.5Mo + 13.1W$

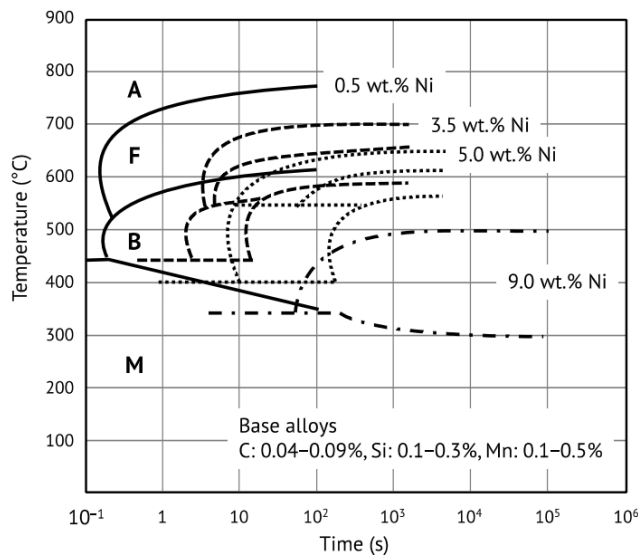


Fig. 2.17 Effect of Ni content on CCT diagram transformation behavior of low carbon steel (Reprinted from Mohrbacher et al [89])

Huang et al. [95] demonstrated this effect in low-carbon steels containing up to 0.5 wt% Ni. Nickel alloying markedly increased the CGHAZ toughness at -20 °C for low and high heat input welding conditions, with ductile fracture appearance in both cases. You et al. [96] investigated the influence of higher nickel additions (0.8 and 3.7 wt%) on the CGHAZ microstructure. For the selected weld cycle representing a heat input of 6 kJ/cm, the applied NbTi micro-alloy concept could not prevent substantial austenite coarsening at a peak metal temperature of 1300 °C. However, CGHAZ toughness at -20°C is still high. As mentioned above, AF is the desired structure in weld metal because it improves toughness. Bunaziv et al. [97] reported a significant improvement in the impact toughness of the weld metal produced from

laser-arc hybrid welding due to high AF fraction. The effect of AF fraction on impact toughness was also reported by Kim et al. [98] and Dallam et al. [99]. The Charpy v-notch toughness values in Figure 2.18 showed that as fraction AF increased, the absorbed energy increased [7]. The interlocking nature of AF, together with its fine grain size, provides the maximum resistance to crack propagation by cleavage. The formation of GBF, ferrite side plates, or upper bainite is detrimental to weld metal toughness since these microstructures provide easy crack propagation paths. Nickel retards the nucleation and growth kinetics of the GBF, refines the microstructure, and increases the share of AF at the expense of GBF.

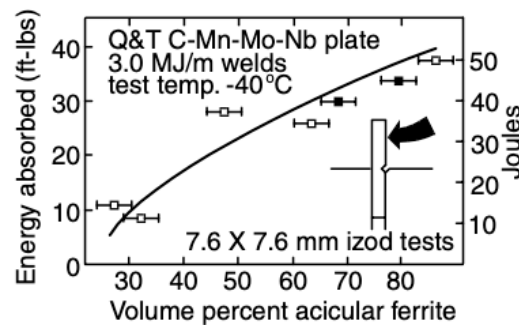


Fig. 2.18 Effect of AF fraction on absorbed energy from SAW welded specimens (Reprinted from Kou [7])

2.4 Crystallographic evaluation in welds

The microstructural characterization of metals has evolved significantly due to the increased use of the Electron backscatter diffraction (EBSD) technique because this technique allows obtaining information on a high number of microstructural characteristics from diffraction patterns of the scanning electron microscopy (SEM) and data treatment into diverse maps, figures, and histograms. These obtained diffraction patterns enable us to measure the crystal orientation, grain boundary misorientations, grain size, phase identification, texture, and strain [100-104].

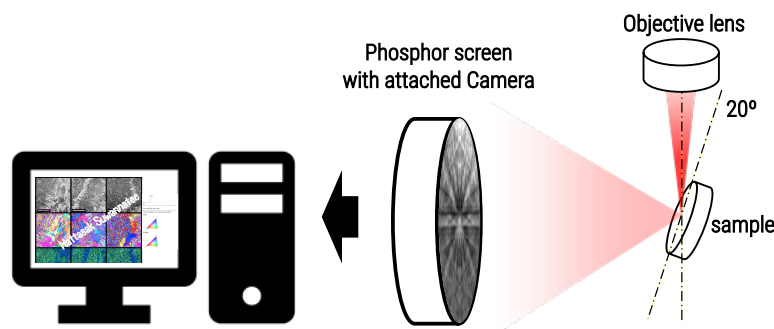


Fig. 2.19 The experimental setup for EBSD analyze

Proper mechanical polishing is needed to provide sufficient quality Kikuchi patterns with a high-confidence index. The further required step is polishing with Colloidal silicas consisting of negatively charged particle silicon dioxide. The final step for EBSD preparation is Electropolishing and immediately observing to avoid the oxidation problem by attaching the mount with 70 degrees tilted toward the Phosphor-screen as illustrated in Figure 2.19.

An inverse pole figure (IPF) is a tool for representing crystal orientation maps, as it provides a color key for interpreting the data. The IPF has three corners, each representing a specific orientation, and individual measurements correspond to points plotted on the IPF. To facilitate visualization, colors such as red, blue, and green are assigned to the corners of the figure, with smooth transitions between colors. This color scheme allows each measurement to be associated with a unique color in the orientation maps, as shown in Figure 2.20. Peng et al. [67] utilized the IPF map to examine the influence of the cooling rate on the grain size in HAZ. Lehto et al. [103] proposed the IPF maps of weld metals produced from different welding processes. Figure 2.21 illustrates the IPF map where the black line represented grain boundaries (more than 10° misorientation angle).

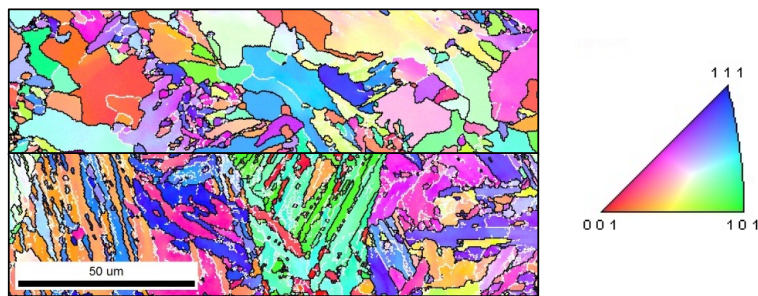


Fig. 2.20 Samples IPF Maps (EBSD IPF maps in this dissertation)

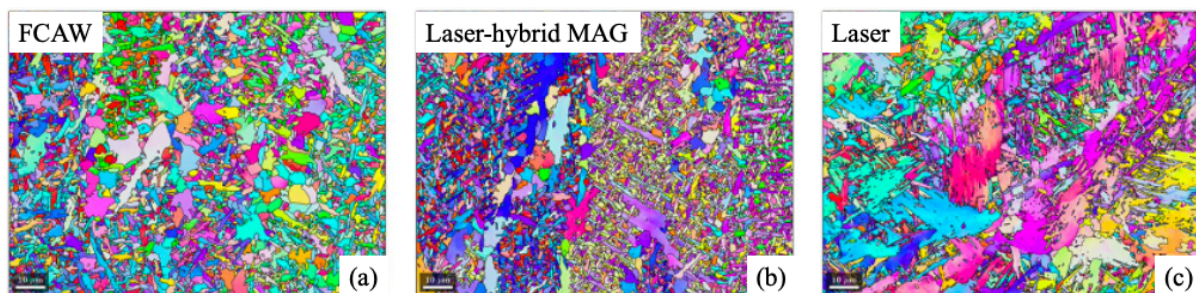


Fig. 2.21 IPF maps from weld metal subjected to different welding process (a) FCAW; (b) Laser-hybrid MAG; (c) Laser (Edited and reprinted from Lehto et al [103])

Grain boundary angle data can utilize to distinguish different microstructures [94, 101, 105]. Gourgues et al. [101] proposed that acicular ferrite and bainite exhibit a significant proportion of high-angle grain boundaries, characterized by two peaks at approximately 50° and 60° . These microstructures also show minimal misorientation angles ranging from 25° to 45° . In contrast, martensite predominantly

displays a strong peak around 60°, accompanied by a secondary at 50°, with a smaller portion of low misorientation angles [105]. Jorge et al. [94] summarized the patterns of misorientation angles for acicular ferrite, polygonal ferrite, bainite, and martensite, as illustrated in Figure 2.22.

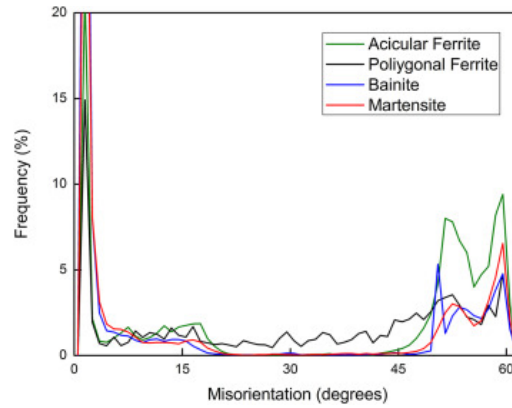


Fig. 2.22 Grain boundary misorientation angle profile of weld metal microstructure. (Reprinted from Jorge et al [94])

The Kernel Average Misorientation (KAM) is a technique utilized to evaluate local strain gradients in materials. By calculating the average misorientation angles between neighboring crystallographic orientations, as indicated by the red line in Figure 2.23. When the misorientation angle exceeds 15°, it is considered a grain boundary and represented by the black line in the figure. On the other hand, misorientation angles ranging from 2° to 15° are considered low-angle grain boundaries, which indicate the presence of stored energy within the grain.

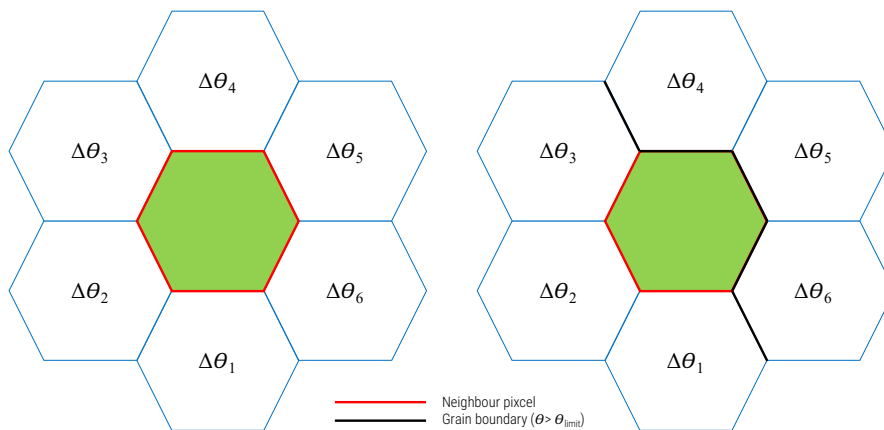


Fig. 2.23 Definition of KAM

The resulting KAM values are depicted in color maps. The different colors represent different levels of misorientation and corresponding different dislocation densities. Shamsujjoha [104] investigated the dislocation density during the deformation of low-lath martensitic steels using KAM maps to analyze the evolution of the substructure, as illustrated in Figure 2.24. The bright shade color represented

the high dislocation density at the coarse laths. This high KAM value also increases with the increase in carbon content. Vogt et al. [106] used the KAM and low-angle grain boundary to characterize the dislocation arrangement in fatigue specimens illustrated in Figure 2.25. The high KAM value represented the more strain generated after being subjected to fatigue loads.

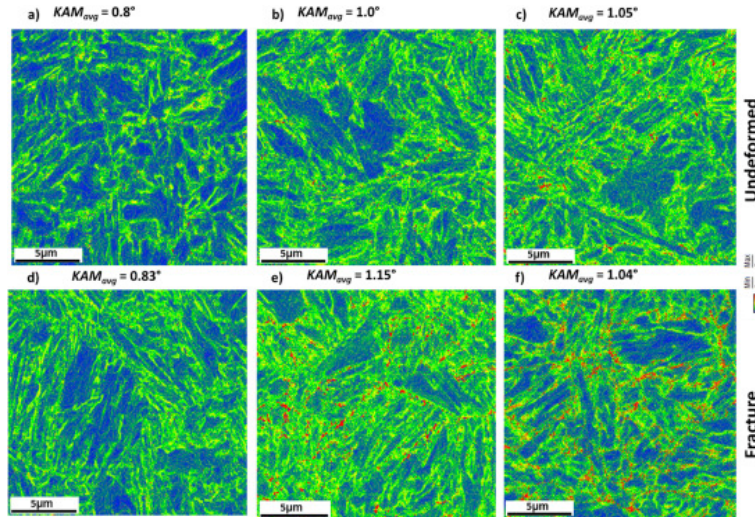


Fig. 2.24 KAM maps of undeformed and fracture of various carbon content in martensitic steel; (a) and (d) 0.18%C; (b) and (e) 0.25%C; (c) and (f) 0.30%C (Reprinted from Shamsujjoha [104])

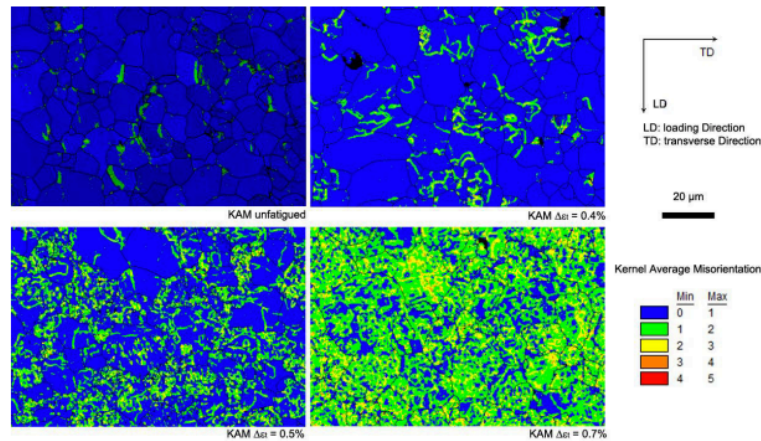


Fig. 2.25 KAM maps after applied fatigue; (a) unfatigued; (b) $\Delta\varepsilon = 0.4\%$; (c) $\Delta\varepsilon = 0.5\%$; (d) $\Delta\varepsilon = 0.7\%$ (Reprinted from Vogt et al [105])

Another objective of this study is to utilize EBSD analysis tools to characterize the microstructure of weld metal produced with varying levels of Ni content using hot-wire insertion. The weld metal cooling profile helps us to investigate the solidification process. In addition to the EBSD data, Vickers hardness, Charpy impact, and tensile test provide detailed insights into the microstructure characterization and its correlation with the mechanical properties, specifically focusing on the Ni content effect.

Chapter 3

A novel approach to single-pass welding of square butt joints without edge preparation

3.1 Introduction

This chapter aims to investigate the limitations of conventional GMAW and optimize the welding conditions of hot-wire GMAW to achieve single-pass welding on a square butt joint using 15-mm thick steel plates. To achieve this goal, the author investigates the effect of hot-wire fraction on the quality of the welded joint. The welding quality is monitored using a high-speed camera, and the welded profile geometry on an etched cross-section is measured in detail. Furthermore, the power consumption and arc time are calculated and compared with the conventional GMAW welded joint in order to demonstrate the significant energy savings and increased productivity associated with the hot-wire GMAW process.

3.2 Materials, machines and methodology

3.2.1 Materials

A square butt joint of JIS-G3101-SS400 with as-cut surfaces of a 350-mm length, an 80-mm width, and a 15-mm thickness was assembled with a 9-mm thick backing plate for the experiment. Two different root gaps, 5-mm and 10-mm as shown in Figure 3.1. The filler metals used for GMAW was a solid wire JIS-Z3312-YGW11 (G49A0UC11), with a diameter of 1.4 mm while the filler wire used for hot-wire had a diameter of 1.2 mm. Chemical compositions of the materials used in the experiment were provided in Table 3.1.

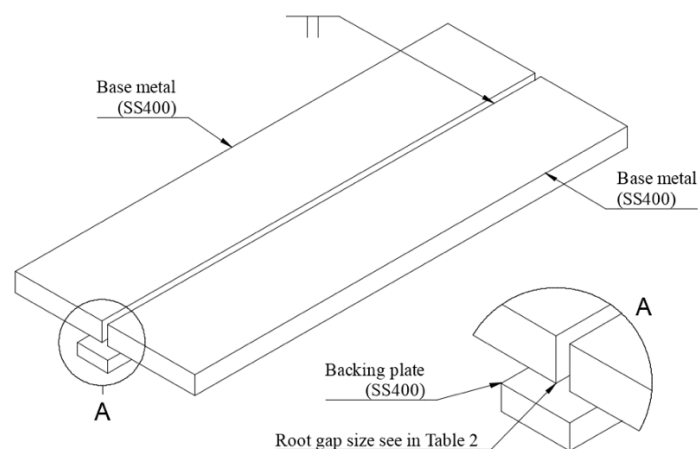


Fig. 3.1 Joint configuration

Table 3.1 Chemical compositions of materials being used in this chapter

Material	Fe	C	Si	Mn	P	S	Cu	Ti+Zr
JIS-G3101-SS400 350mm x 80mm x 15mm	Bal.	0.26	0.40	-	0.04	0.05	-	-
G49A0UC11 (YGW11)	Bal.	0.04	0.73	1.58	0.01	0.01	0.23	0.22

3.2.2 Machines

The welding power source for GMAW is a constant voltage characteristic YD-500CL5 Panasonic with an output current and voltage adjustable range of 60 to 500A and 17 to 39V, respectively. The hot-wire power source is inverter power source YW-35 Power assist (Model: IV1320) Matsumoto-kikai (MAC) with maximum capacity of hot-wire current and hot-wire feeding speed at 200A and 18.8 m/min, respectively.

The travel speed was controlled using an IAI-RCS-2SS8C slider with a limited maximum movement at 500mm, the accuracy within 0.02 mm. A data acquisition system of 5000Hz intervals was used to collect a welding current in A, an arc voltage in V, hot-wire current in A, hot-wire voltage in V, GMAW and hot-wire feeding speed in m/min, and cooling profile of molten pool in °C.

The arc phenomenon and molten pool formation were observed by a MEMRECAM HX-7 NAC high-speed camera. The transmitted wavelength of 810 ± 10 nm of band pass filter was attached to the optical lens. A shutter speed of 1/1000 second and a 500 frame per second were used.

3.2.3 Methodology

Figure 3.2 (a) shows a schematic of experimental setup of solo GMAW process. The 100%CO₂ was used as a shielding gas. The GMAW torch was placed perpendicular to the welding direction and backing plate. Figure 3.2 (b) shows the combination of GMAW and hot-wire with 10-mm delay of hot-wire feeding position in welding direction. The contact tip to work distance and power supplied distance were held constant at 30- and 100-mm. Hot-wire feeding angle was fixed at 70 degree from the backing plate. The arc phenomenon and molten pool formation were observed in detail during welding.

Initially, the GMAW was performed without hot-wire insertion to determine process capabilities and limitations. Table 2 provides the welding conditions that were used in the experiment. In order to investigate the effect of welding current on the weld metal profile and arc position on square butt joint, the welding current was intentionally increased from 300A to 500A by 50A increase, while the other parameters, such as an arc voltage of 38 voltage and travel speed of 0.3 m/min were

held constant and mentioned as initial condition. Wire feeding speed (WFS) was measured and calculated the deposition rate of GMAW at different applied welding currents. Subsequently, additional experiments using a larger gap which increased a gap size from 5- to 10-mm and while remain the same travel speed (larger gap condition) and a faster welding speed which a travel speed was increased from 0.3- to 0.6 m/min while remain the gap size as 5-mm (faster speed condition) were conducted to expose the limitations of the GMAW process.

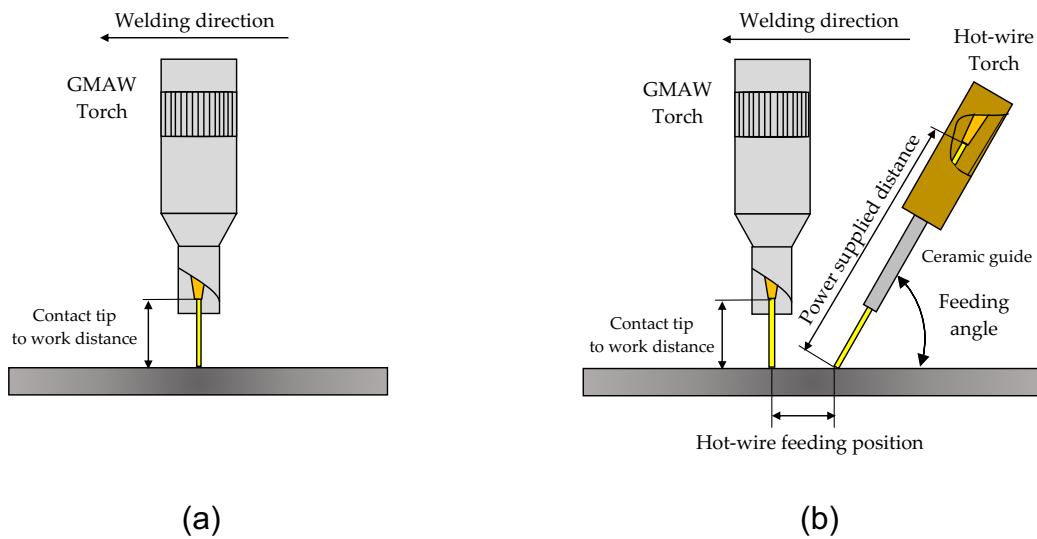


Fig. 3.2 Welding experiment setups: (a) schematic diagram of solo GMAW; (b) schematic diagram of hot-wire GMAW with explained parameters

Table 3.2 Conditions of solo GMAW

Parameters	Initial condition	Larger gap condition	Faster speed condition
Gap size, mm	5	10	5
Travel speed, m/min	0.3		0.6
Welding current, A	300-500		
Arc voltage, V	38		
Gas flow rate, L/min	25		
Contact tip to work distance, mm	30		

Then, the resulting welds were cross-sectional cut, polished and etched with a 3% Nitric acid. Subsequently, the weld geometry was observed. Figure 3.3 shows the weld geometry parameters being measured on the obtained welded cross-sectional such as fusion area (A), depth of penetration (D), maximum width (W) and its height (H).

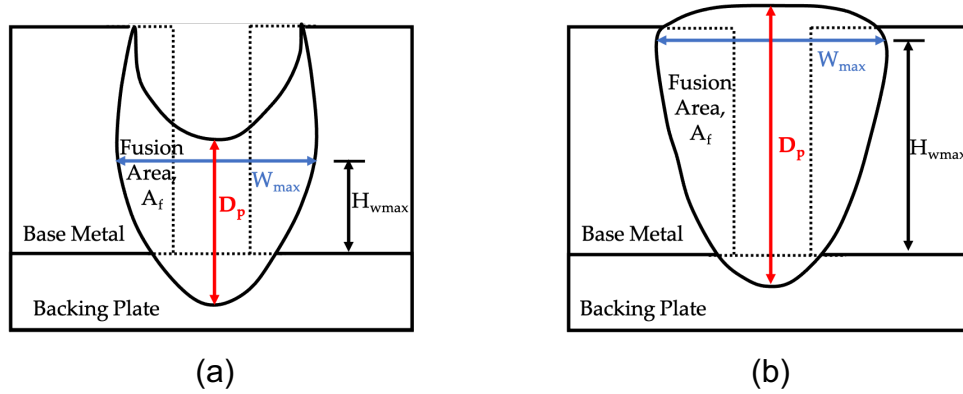


Fig. 3.3 The measured parameters on the obtained welded cross-section:
(a) weld geometry parameters for underfill condition;
(b) weld geometry parameters for full penetration condition

3.3 Calculations

3.3.1 Calculation of optimum hot-wire current

In order to obtain an exactly deposition volume, hot-wire must be smoothly and continuously fed into the molten pool. Several researchers provided simple calculations to derive an optimum hot-wire current which related to the hot-wire feeding speed [25,52]. The power supplied distance of 100 mm was divided into a segment with 0.1 mm. Then, the temperature increment on the segment (ΔT) in degree Celsius is given by Equation (3.1).

$$\Delta T = \frac{Q}{\pi \times r^2 \times L \times C(T) \times m(T)} \quad (3.1)$$

where $C(T)$ is the temperature-dependent specific heat in $J/kg \cdot ^\circ C$, $m(T)$ is the temperature-dependent density in kg/m^3 , r is the radius of the hot wire filler metal in mm

Q is the net heat increase is the different between the generated heat by the Joule heating into the segment (Q_{in}) in J and the heat loss from the segment (Q_{out}) in J, which was calculated using equation (3.2)

$$Q = Q_{in} - Q_{out} \quad (3.2)$$

Where

$$Q_{in} = R(T) \times I^2 \times t \quad (3.3)$$

where $R(T)$ is the temperature-dependent resistance of the filler metal in Ω , I is the hot-wire current in A, and t is the heating time through the segment in s.

The temperature-dependent resistance $R(T)$ of the segment is express as

$$R(T) = (R_c + \rho(T)) \times L / \pi r^2 \quad (3.4)$$

where $\rho(T)$ is the temperature-dependent specific electrical resistivity in $\Omega \cdot m$, R_c is the contact resistant in Ω .

The heating time through a segment is

$$t = D \times 60 \times L / v_{HW} \quad (3.5)$$

where D is the duty cycle of the wire heating (normally set at 50%), v_{HW} is the hot wire feeding speed in mm/s.

The heat loss (Q_{out}) in J is express as

$$Q_{out} = h \times \pi r^2 \times \Delta T \quad (3.6)$$

where h is the comprehensive heat loss coefficient in W/m^2K

The temperature increment on a segment (ΔT) is the different between the temperature of filler metal (T_W) and ambient temperature (T_A) in $^\circ C$ given as

$$\Delta T = T_W - T_A \quad (3.7)$$

Substituting equations (3.2) to (3.7) into equation (3.1), a simple equation is derived to calculate the temperature increment on the hot-wire segment:

$$(T_W - T_A) = \frac{I^2}{v_{HW}} \times \frac{60 \times L \times D \times (R_c + \rho(T))}{\pi^2 \times r^2 \times C(T) \times m(T)} - \frac{h \times (T_W - T_A)}{C(T) \times m(T) \times L} \quad (3.8)$$

Equation (3.8) is used to obtain the optimal hot-wire current (I) when the wire temperature at the tip equals the melting temperature.

3.3.2 Calculation of hot-wire fraction

Hot-wire insertion was used as independent deposition and intentionally increased which contribute to total deposition volume. Thus, the hot-wire fraction was used to represented its effect which is given as follows:

$$\%HW = \frac{V_{HW}}{(V_{HW} + V_{GMAW})} \times 100 \quad (3.9)$$

Where $\%HW$ is the hot-wire fraction in percent, V_{HW} is the deposition rate of hot-wire mm^3/s , and V_{GMAW} is the deposition rate of GMAW in mm^3/s , V_{GMAW} is the wire feeding speed of GMAW in mm/s which given by

$$V_{HW} = \pi \times 1.2^2 \times v_{HW} \quad (3.10)$$

$$V_{GMAW} = \pi \times 1.4^2 \times v_{GMAW} \quad (3.11)$$

Substituting equations (3.10) and (3.11) into equation (3.9) to calculate the percentage of hot-wire fraction of total deposition rate.

3.3.3 Calculation of power consumption

A data acquisition system of 5000Hz intervals was used to collect a welding current in A, an arc voltage in V, hot-wire current in A and hot-wire voltage in V. Then, the total power consumption (P_{total}) using the equation as follows:

$$P_{total} = (P_{GMAW} + P_{HW}) \times t_{arc} \quad (3.12)$$

$$P_{GMAW} = \frac{(I_{GMAW1} \times V_{GMAW1}) + (I_{GMAW2} \times V_{GMAW2}) + \dots + (I_{GMAW5000} \times V_{GMAW5000})}{5000} \quad (3.13)$$

$$P_{HW} = \frac{\left(\sqrt{I_{HW1}^2} \times \sqrt{V_{HW1}^2} \right) + \left(\sqrt{I_{HW2}^2} \times \sqrt{V_{HW2}^2} \right) + \dots + \left(\sqrt{I_{HW5000}^2} \times \sqrt{V_{HW5000}^2} \right)}{5000} \quad (3.14)$$

Here, P_{GMAW} is the power used in GMAW in kJ, P_{HW} is the power used in hot wire insertion (kJ), I_{GMAW} is the welding current (A), V_{GMAW} is the arc voltage (volt), I_{HW} is the hot-wire current (A), and V_{HW} is the hot-wire voltage (volt), and t_{arc} is arc time in s.

3.4 Capability of gas metal arc welding process

3.4.1 Relationship between welding current and wire feeding speed

Figure 3.4 illustrates the relationship between the welding current and measured WFS during solo GMAW. The findings demonstrate that despite fluctuations in welding current, the constant voltage GMAW welding power source maintains a nearly constant arc length, which establishes a proportional relationship between welding current and WFS [6]. The result revealed that increasing welding current is necessary to obtain a larger deposition volume, led to a higher heat input to the joint, ultimately causing grain coarsening adjacent to the fusion line and a reduction in joint properties. This highlights the limitation of conventional GMAW welding in achieving desired deposit volumes and emphasizes the importance of independent supplemental deposition techniques that are not reliant on welding current.

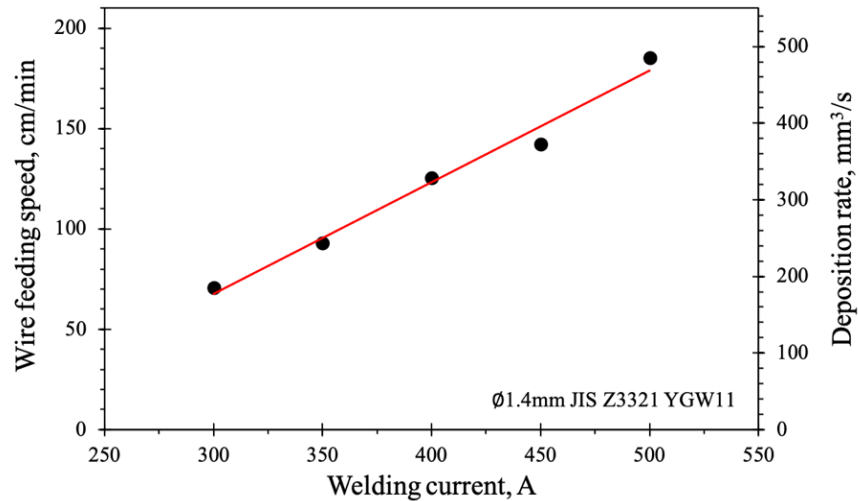
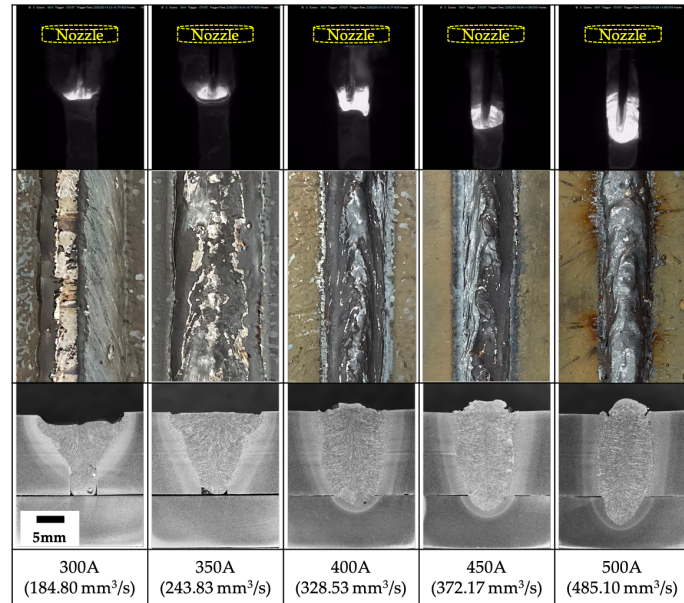


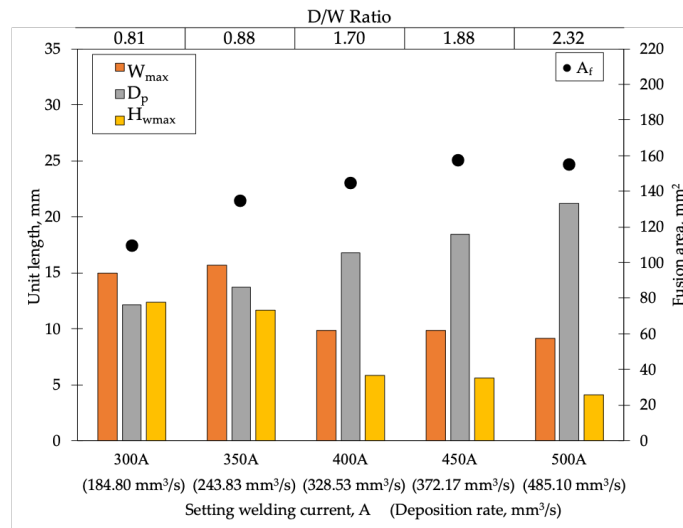
Fig. 3.4 The relationship between welding current, wire feeding speed, and deposition rate.

3.4.2 Arc phenomenon, bead appearance and weld geometry

The study examines the impact of varying welding currents, ranging from 300 to 500A, on three different conditions, as previously outlined. Figure 3.5 (a) displays the captured arc position, weld bead appearance, and the cross-sectional area of the initial conditions are shown when conventional GMAW was applied on a 5 mm gap of square butt joint with a welding speed of 0.3 m/min. The captured arc phenomenon demonstrates the different positions of arc, which are related to the height of molten pool. When the welding current was increased, the arc moved towards the depth direction, resulting in a longer stick-out distance of the filler metal. The regular weld bead shape could not be achieved in this initial condition. Welding currents less than 400A resulted in insufficient depth of penetration, leading to underfill and incomplete fusion with a cone-shaped fusion area. However, increasing the welding current helped to suppress incomplete fusion, leading to a change in the shape of the fusion area from cone to rectangular. Figure 3.5 (b) illustrates that increasing the welding current not only provides a larger deposition volume but also has a significant effect on the weld profile geometry. Increasing the welding current resulted in a narrower maximum weld width (W_{max}) and larger depth of penetration (D_p). The height of maximum weld width (H_{wmax}) represents the arc position in this experiment and indicates that the arc occurred deep down into the thickness direction. Similar behavior was also observed by Nakamura et al. [107].



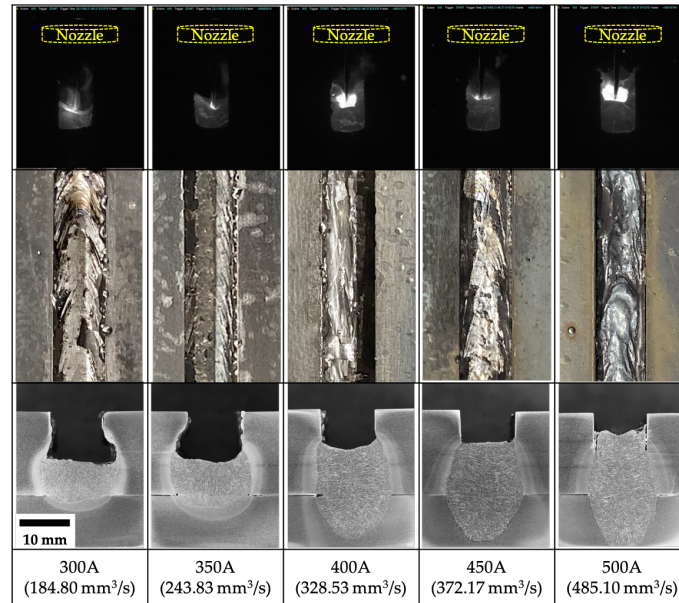
(a)



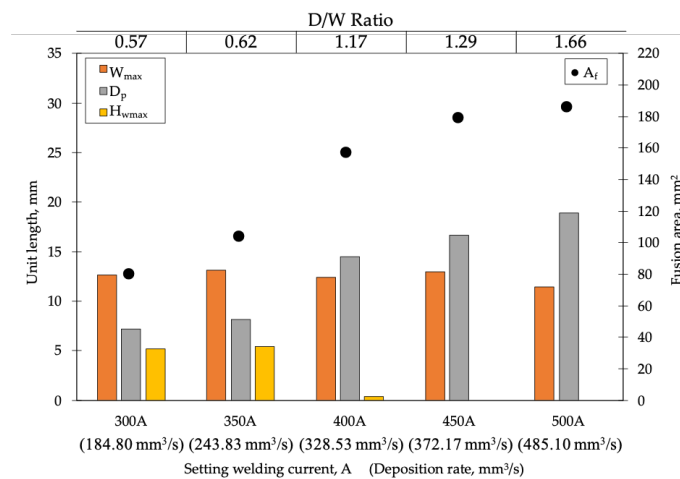
(b)

Fig. 3.5 Influence of welding current on a 5 mm gap at 0.3 m/min travel speed:
 (a) Arc behavior, weld bead appearance and cross-sectional analysis;
 (b) Weld profile measurement.

The depth-to-width ratio (D/W) was used to explain the change in the shape of weld profile and its sensitivity to hot-cracking [22]. Welding current between 400 to 500A provided similar fusion area sizes but with a large difference in D/W. The high D/W obtained can lead to solidification cracking along with the humping bead shape resulting from this and was considered unacceptable. Moreover, the irregular shape of the weld cap was clear evidence that molten metal precedence had occurred [38-40]. Therefore, larger gap conditions and faster welding speed conditions were determined in further experiments.



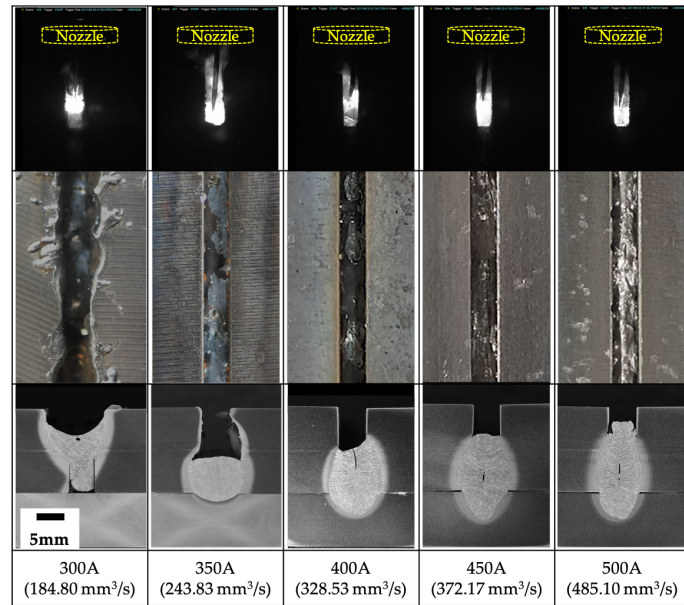
(a)



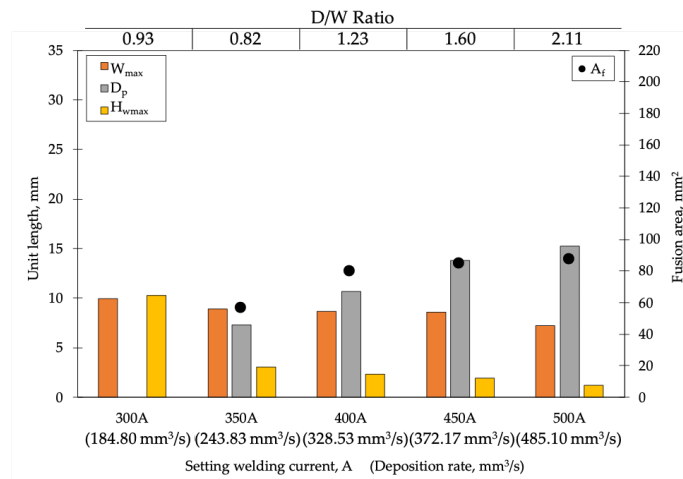
(b)

Fig. 3.6 Influence of welding current on a 10 mm gap at 0.3 m/min travel speed:
 (a) Arc behavior, weld bead appearance and cross-sectional analysis;
 (b) Weld profile measurement.

Similar deposition rates were applied at the same welding speed but with an increased root gap from 5 to 10 mm. Figure 3.6 (a) illustrates the captured motion during welding, the appearance of the weld bead, and the obtained cross-sectional area produced from comparable deposition rates. The larger root gap allowed for a bigger molten pool to be generated at the root, even when using the lowest welding current (300A) in this experiment. Despite increasing only the gap size, sufficient deposition volume to provide a single-pass welding could not be obtained, although it did suppress the molten metal precedence.



(a)



(b)

Fig. 3.7 Influence of welding current on a 5 mm gap at 0.6 m/min travel speed:
(a) Arc behavior, weld bead appearance and cross-sectional analysis;
(b) Weld profile measurement.

Figure 3.6 (b) shows that the H_{wmax} decreased when the welding current was increased, and the arc occurred deep into the thickness direction, which led to a high D/W ratio. However, the yellow bar indicated only the positive value which mean the arc occurred on backing plate region. When a welding current above 450A was applied, the obtained D_p was greater than the thickness of the base metal. The authors believe that if the arc position could be shifted to the upper side of the joint, unnecessary penetration could be reduced, and a single-pass welded joint could be obtained.

Another approach was attempted in which a similar deposition rate was used on a 5 mm root gap, but the travel speed was increased from 0.3 to 0.6 m/min. Figure 3.7 (a) illustrates the captured arc phenomenon, weld bead shape, and macro-etched cross-sectional area. Unfortunately, when using a welding current of 300A, the molten pool was generated at the upper side of the gap, leading to incomplete fusion at the bottom side. Thus, the D/W ratio and D_p could not be determined for this parameter. Travel speed is the most dominant factor in heat input [7, 56]. The half-heat input due to doubling the welding speed provided smaller molten pool size which indicated in the captured arc phenomenon. In this experiment, all welding currents provided underfill weld bead (insufficient deposition volume) and poor weld geometry (high D/W ratio) which also results in solidification cracks at the center of the weld metal perpendicular to the solidified direction. Figure 3.7 (b) depicted the similar trend of H_{wmax} , which decreased when increasing welding current compared to both prior experiments. Similar behavior was observed with W_{max} , which decreased when the welding current was increased.

In conclusion, these three experiments reveal the limitations of conventional GMAW, where the deposition rate is restricted by the amount of welding current. This series of experiments shows that single-pass welding on a square butt-joint of 15-mm thick steel plate could not be achieved using solo conventional GMAW. To overcome this drawback, an independent additional volume from hot-wire was used in further investigation.

3.5 Capability of hot-wire gas metal arc welding process

3.5.1 Relationship between hot-wire current and hot-wire feeding speed

To ensure continuous feeding from hot-wire insertion, the appropriate hot-wire current was determined based on the wire feeding speed. Figure 3.8 depicts the behaviors observed for a 1.2 mm diameter hot-wire with a feeding speed of 10 m/min. The calculated hot-wire current presented in the red circle which provided an appropriate feeding. If the hot-wire current is insufficient, it can result in the formation of unmelted products, which can cause inclusions or unmelted regions in the weld metal. Conversely, excessive hot-wire current can lead to wire feeding interruption and explosions, which can negatively affect the deposition rate and weld quality. The correlation between the optimum hot-wire currents and hot-wire feeding speed was established and used in subsequent experiment. This correlation is essential for achieving a stable wire feeding and maintaining the desired weld quality for single-pass welding.

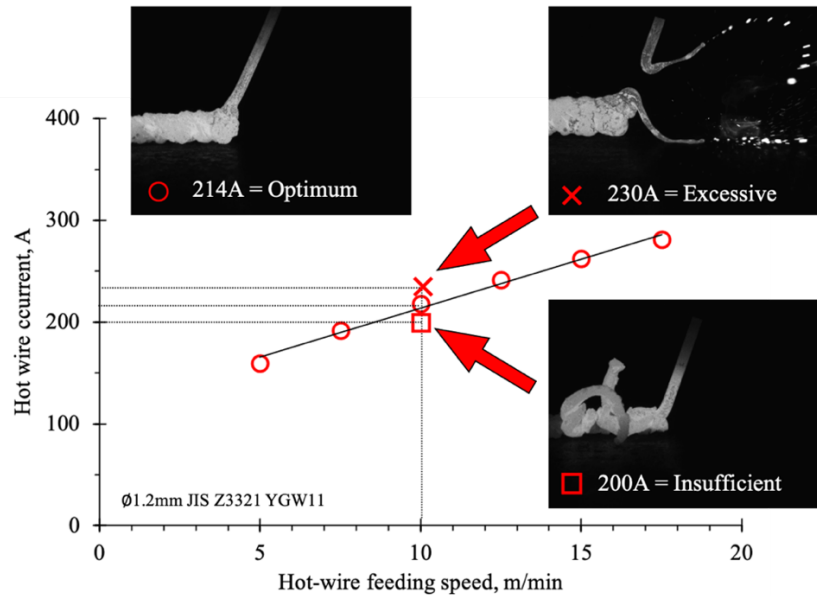
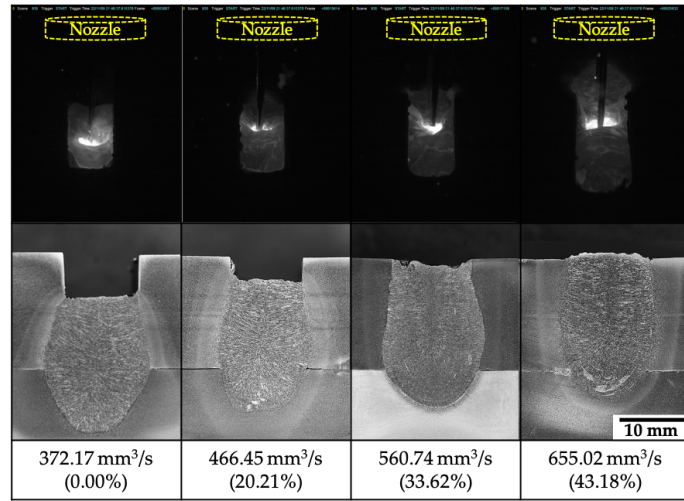


Fig. 3.8 The correlation between optimum hot-wire current and hot-wire feeding speed.

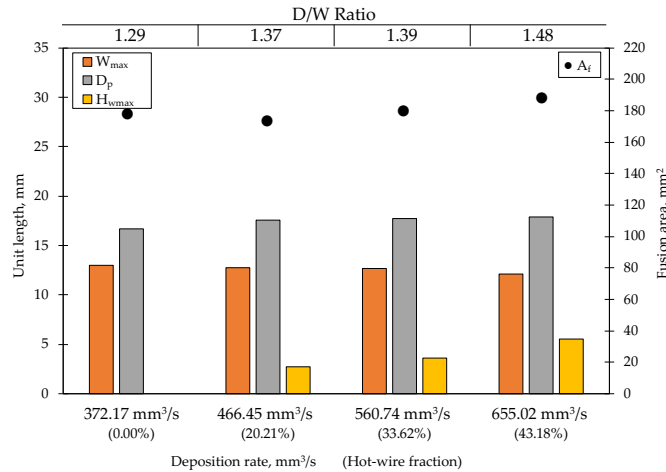
3.5.2 Effect of hot-wire fraction on weld formation and weld geometry

Hot-wire insertion in this study was used as an independent fraction volume that did not depend on welding current but effect to the total deposition volume. The hot-wire fraction was intentionally increased to achieve sufficient deposition rates for larger gap and faster welding speed conditions. Based on the result from conventional GMAW in prior session, welding currents of 500A were excluded from the experiment due to excessive deposition volume and a wild arc, while currents below 400A provided insufficient deposition volume that could not be compensated with hot-wire insertion. Therefore, a constant welding current of 450A was chosen to optimize the single-pass welding condition. The hot-wire fraction was used to explain the weld pool formation and the obtained weld geometry. Increasing its fraction in the total deposition volume allowed for successful single-pass welding under the specified conditions.

Figure 3.9 (a) shows the arc position and weld profiles obtained at a welding speed of 0.3 m/min. Increasing the hot-wire fraction lifted the positioning of the weld profile towards the weld surface, resulting in the generation of the molten pool at the upper side of the gap. Although the total deposition volume increased significantly when hot-wire fraction was increased, the arc force was sufficient to maintain the molten pool shape. Figure 3.9 (b) illustrates the geometry of the welded profile, such as W_{max} and D_p which remained similar, except for an increase in H_{wmax} , representing the arc position. The D/W ratios emphasized the similarity of the weld geometry. Therefore, hot-wire fraction can be used to adjust the position of the weld profile and reduce unnecessary penetration. A sound joint condition was achieved at 43.18% hot-wire fraction.



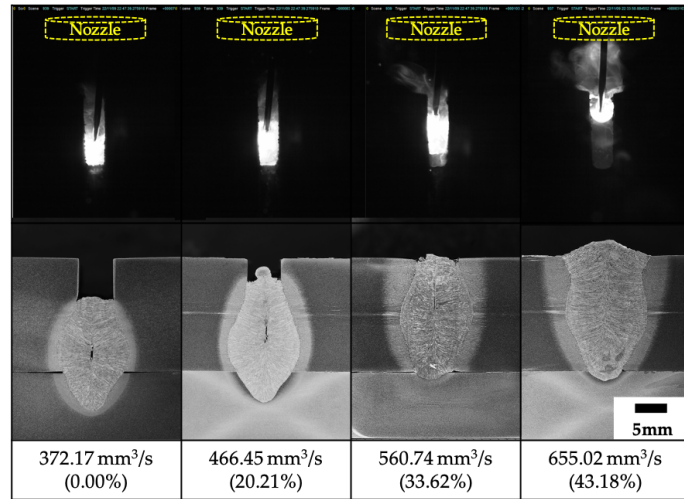
(a)



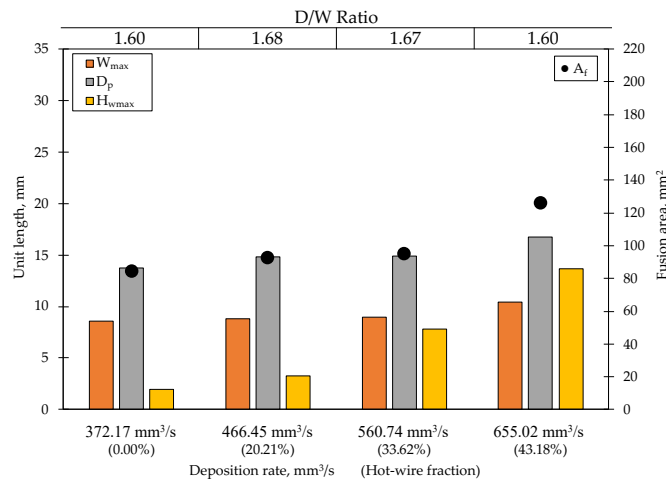
(b)

Fig. 3.9 Influence of hot-wire fraction on a 10 mm gap at 0.3 m/min travel speed: (a) Arc behavior and cross-sectional analysis; (b) Weld profile measurements.

Similarly, parameters were applied to a 5 mm gap size with a travel speed of 0.6 m/min. Figure 3.10 (a) shows that the position of the arc changed when the hot-wire fraction was increased. While the GMAW fraction remained constant, the arc occurred at the top surface by increasing the hot-wire fraction up to 43.18%. This is strong evidence that hot-wire fraction could be used to control the arc position and enlarge the process tolerance. Thus, a single-pass welding of a 15-mm square butt joint could be achieved, even when the travel speed was increased to 0.6 m/min. Figure 3.10 (b) illustrates a similar trend in weld geometry to the prior experiment, with an obvious increase in H_{wmax} . Surprisingly, solidification cracks that first occurred when conventional GMAW was applied changed their position when the hot-wire fraction was increased. At 43.18% hot-wire fraction, the cracks disappeared, providing a sound joint.



(a)



(b)

Fig. 3.10 Influence of hot-wire fraction on a 5 mm gap at 0.6 m/min travel speed: (a) Arc behavior and cross-sectional analysis; (b) Weld profile measurements.

In conclusion, a single pass welding using hot-wire GMAW has successfully developed at both travel speed of 0.3 and 0.6 m/min, respectively. However, effect of hot-wire fraction on cooling profile and weld metal structure will be further investigated.

3.6 Effect of hot-wire on cooling behavior and weld metal properties

The formation of the molten pool in arc welding is influenced by factors such as welding current, arc voltage, and travel speed. However, limited research has explored the impact of hot-wire fraction during GMAW on molten pool formation. In this study, the author employed thermocouples to measure the cooling profile during

hot-wire GMAW at various hot-wire fractions and travel speeds of 0.3 and 0.6 m/min. Detailed observation of the weld metal microstructure was conducted, and Vickers hardness testing was performed to identify the optimized welding condition for the new approach of single-pass welding using hot-wire GMAW.

3.6.1 Cooling profile and obtained weld metal structure

Figure 3.11 (a) illustrates the cooling profile for various hot-wire fraction at different travel speeds. At 0.3 m/min of travel speed, similar cooling profiles were obtained regardless of the hot-wire fraction whereas the red bolt line represented the 43.18% of hot-wire fraction. However, at 0.6 m/min of travel speed, the cooling profile varied significantly with different hot-wire fraction whereas the green bolt line represented the 43.18% of hot-wire fraction at this travel speed. Effect of the hot-wire fractions were obviously seen in Figure 3.11 (b), where the cooling time from 800 to 500°C was delayed regarding to increasing hot-wire fraction for the both travel speed. However, the faster travel speed condition, the cooling time was double when hot-wire fraction was increased from 0.00% to 43.18% Figure 3.11 (c) depicted the effect of hot-wire fraction on cooling rate and obtained weld metal microstructure. At 0.3 m/min of travel speed, the microstructure predominantly consisted of grain boundary ferrite (GBF) and side plate ferrite (SPF). The fraction of GBF increased as increasing hot-wire fraction (decrease cooling rate) as illustrated in red square of Figure 3.11 (c). At 0.6 m/min of travel speed, the effect of hot-wire fraction show even more obvious as illustrated in the green square of Figure 3.11 (c). The cooling rate from 800 to 500°C was reduced from 38.31°C/s to 16.07°C/s when hot-wire fraction was increased from 0.00% to 43.18%. However, the obtained acicular ferrite (AF) fraction also high compared with slower travel speed condition. The obtained microstructure was predominantly consisted of AF with SPF inside the thin GBF network. Based on this result, the obtained microstructure was preferred. Figure 3.12 illustrated the different size and width of the heat-affected zone (HAZ) when the travel speed was increased from 0.3 m/min (squared red) to 0.6 m/min (squared green) which emphasizing that faster speed is the optimal condition in this experiment. The effect of the cooling rate on the obtained microstructure using hot-wire insertion similar to the reported from Kou [7] and Xie et al [108], whereas the higher cooling rate provides finer grain and reduces the GBF fraction.

3.6.2 Weld metal hardness

Vickers hardness testing was performed using a 10 kgf load with a 10-second dwell time. The hardness distribution was measured at 8 mm from the bottom side, perpendicular to the welding direction. Figure 3.13 demonstrates that a travel speed of 0.6 m/min resulted in hardness similar to that achieved by the conventional method. This suggests that the AF fraction ratio plays a dominant role in determining the hardness property. In contrast, a slower travel speed led to slightly lower hardness, as shown by the red line in Figure 3.13.

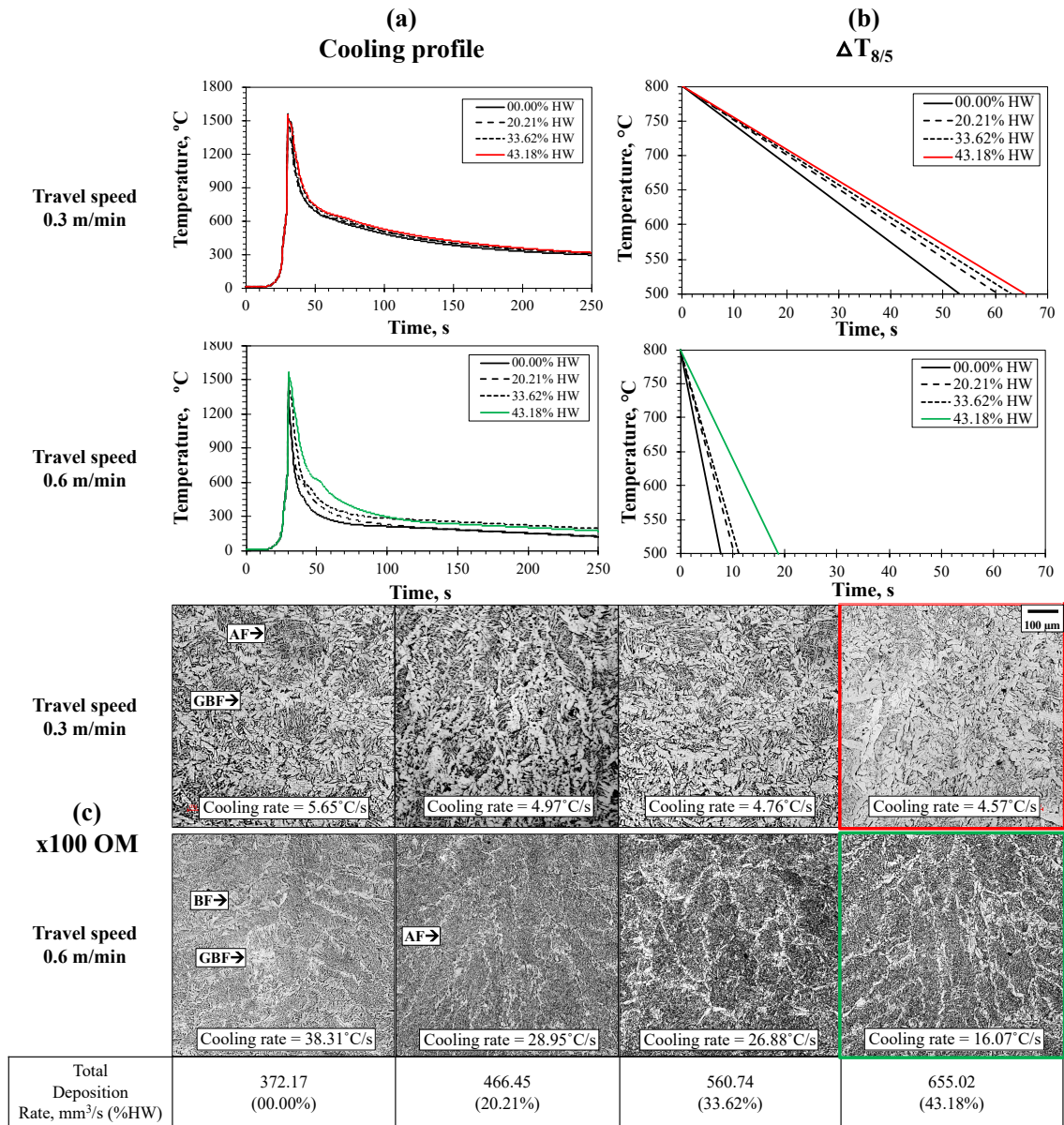


Fig. 3.11 Effect of hot-wire fraction: (a) Cooling profile; (b) $\Delta T_{8/5}$; (c) Microstructure.

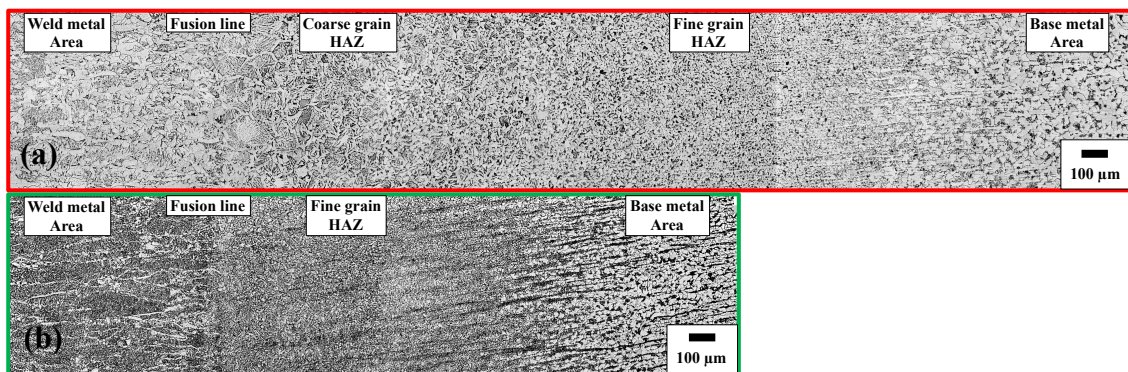


Fig. 3.12 Influence of travel speed on HAZ width: (a) 0.3 m/min; (b) 0.6 m/min.

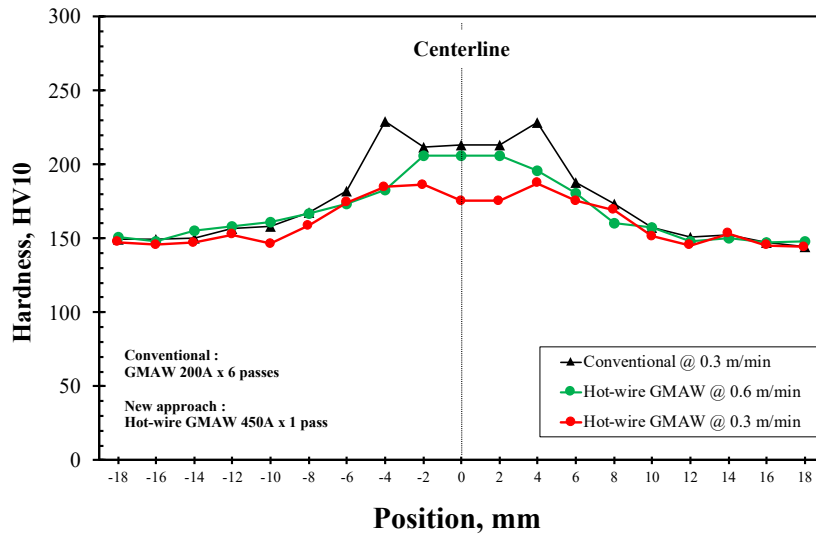


Fig 3.13 Hardness distribution from soundness condition of single-pass welding compare with conventional GMAW

3.7 Production efficiency and power consumption

3.7.1 Production efficiency

Figure 3.14 demonstrates a significant reduction in arc time achieved with the use of hot-wire insertion compared to conventional GMAW. The new approach process resulted in an 83.33% reduction in arc time at the same travel speed. At a travel speed of 0.6 m/min, single pass welding achieved a remarkable 91.67% reduction in arc time. These reductions in arc time can be considered as a measure of production efficiency, which is represented in the gradient bar. The use of hot-wire insertion led to a noticeable increase in production efficiency. By reducing the required number of weld passes from 6 to a single pass, production efficiency increased by up to 500% at the same travel speed of 0.3 m/min. Furthermore, under optimized conditions with a 5 mm gap and a travel speed of 0.6 m/min, the new method increased production efficiency by 1100% compared to conventional GMAW.

3.7.2 Power consumption

Figure 3.15 demonstrates the relationship between deposition rate and power consumption of various welding processes. Conventional GMAW exhibits limited process tolerance, with the deposition volume being dependent on the applied welding current and filler metal diameter [16, 20]. However, a proposal for high current CO₂ arc welding resulted in a high deposition rate, but it requires similar power consumption as submerged arc welding (SAW) [3]. Increasing the diameter of the filler metal improves the deposition rate of SAW as observed in previous study [8], but it inevitably results in high-power consumption. However, the innovative approach of hot-wire insertion has led to a significant reduction of 52% in power

consumption at a similar deposition volume compared to SAW. This represents a sustainable development method of achieving high deposition volume while minimizing power consumption. The optimized hot-wire current and fraction provide a stable hot-wire feeding during the arc and maximize the deposition rate, making it a promising method for welding applications that require high productivity and energy efficiency.

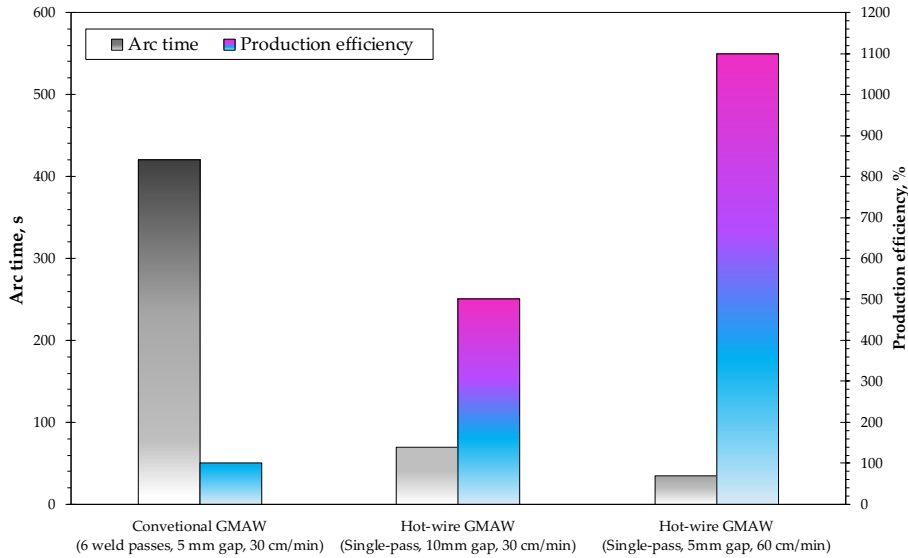


Fig. 3.14 The comparison of arc time and production efficiency between conventional GMAW and a new approach hot-wire GMAW.

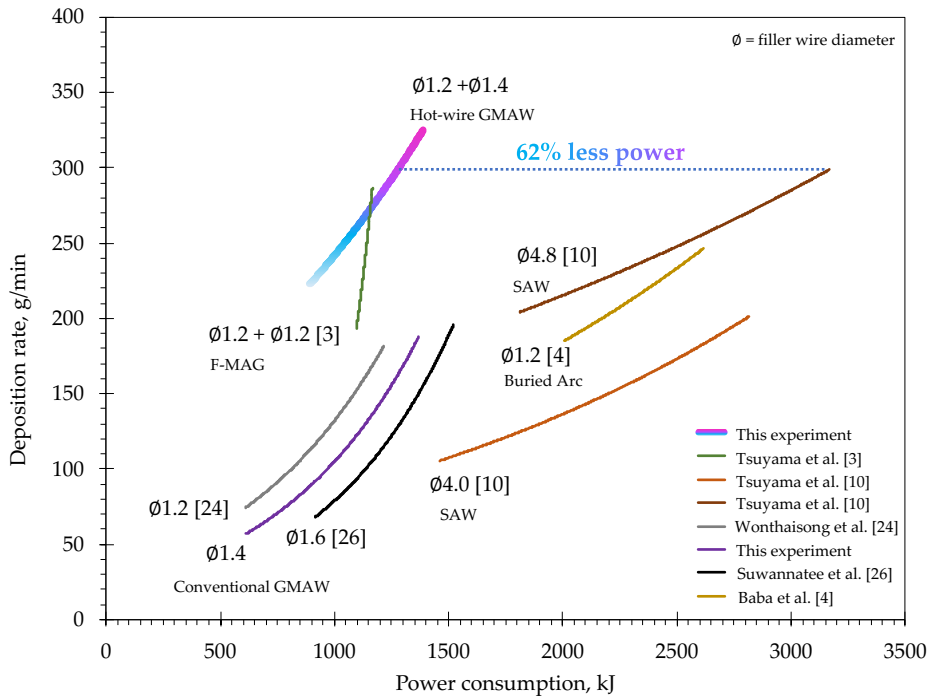


Fig. 3.15 The relationship between deposition rate and power consumption in various welding processes.

3.8 Conclusion

This study investigated the limitation of conventional GMAW and the use of hot-wire fraction as a parameter for controlling the desired position of weld metal. The results showed that the new approach provided a promising sound joint when optimized conditions were applied. The conclusion are as follows:

(1) The limited process tolerance of GMAW process to achieve single pass welding was shown. To obtain more deposition volume, high heat input to the joint is inevitable.

(2) By increasing the hot-wire fraction, the molten pool tends to generate at the upper side of the joint. Unnecessary penetration was decreased, desired position could be obtained, particularly for large gap sizes and high travel speeds

(3) The simplify joint configuration could be used to achieve a single pass welding using a proposed process.

(4) For a single-pass condition, faster welding speed at 0.6 m/min provided a better obtained microstructure with predominantly acicular ferrite content.

(5) Independent deposition volume from hot-wire insertion increased total deposition volume while not required more welding current. A single-pass welding using a welding speed of 0.6 m/min provided 81.25% decreased of power consumption.

(6) The productivity was obviously increased by decreasing the arc time, this new approach provided 91.67% saving up the arc time compare to conventional GMAW.

(7) The use of hot-wire can help reduce the occurrence of solidification cracks in the welded joint.

However, further research is needed to optimize the hot-wire fraction and other process parameters to achieve the best possible welding results for specific applications.

Chapter 4

Optimizing hot-wire fraction for enhance quality and precision of weld formation in GMAW process

4.1 Introduction

The chapter aims to investigate the impact of hot-wire fraction on weld metal properties in hot-wire GMAW process. The investigation was planned and conducted in three stages. In the first stage, hot-wire was used to compensate for the deposition rate while minimizing the GMAW fraction and compared to a similar deposition rate using only conventional GMAW. The second stage determined the maximum hot-wire fraction without causing welding defects or detrimental effects on weld metal properties. In the third stage, the fraction of hot-wire and GMAW was optimized at the highest deposition rate to achieve a sound joint condition with the lowest energy consumption. This systematic approach shows that the hot-wire GMAW process offers a sustainable alternative to conventional GMAW.

4.2 Materials and methodology

4.2.1 Materials

A single-V butt joint was created using K36E-TM (490 MPa-class) as the base material and backing plate. The joint was prepared with a groove angle of 30° and a root gap of 4 mm as depicted in Figure 4.1. For both GMAW and hot-wire filler metal, a solid wire G49A0UC11 (JIS Z3312 YGW11) with a diameter of 1.2 mm was utilized. The chemical composition of materials used in this experiment can be found in Table 4.1.

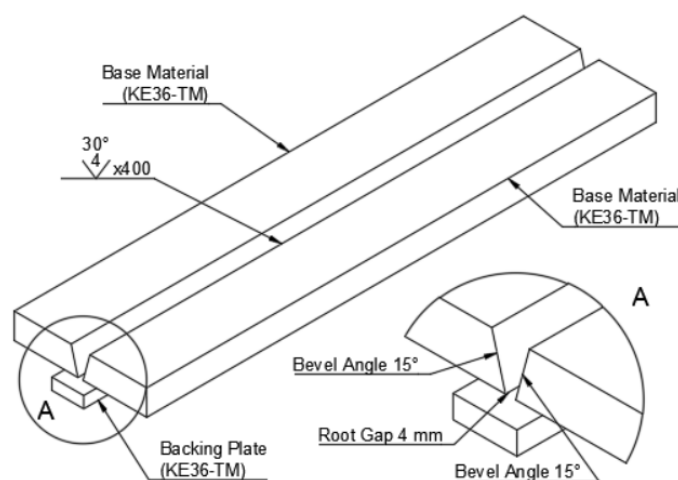


Fig. 4.1 Joint configuration

Table 4.1 Chemical compositions of materials being used in this chapter

Material	Fe	C	Si	Mn	P	S	Cu	Ti+Zr
K36E-TM 400mm x 40mm x 20mm	Bal.	0.12	0.20	1.41	0.014	0.004	-	-
G49A0UC11 (YGW11) ø1.2mm	Bal.	0.04	0.73	1.58	0.01	0.01	0.23	0.22

4.2.2 Methodology

The experiment setup illustrates in Figure 4.2, where the hot-wire torch is positioned 10 mm behind the GMAW torch in the welding direction. The solo GMAW process uses a constant deposition rate of 114.95 g/min (equivalent to a welding current of 300A) on the root pass of all conditions for the baseline conditions. The investigation was conducted in 3 stages.

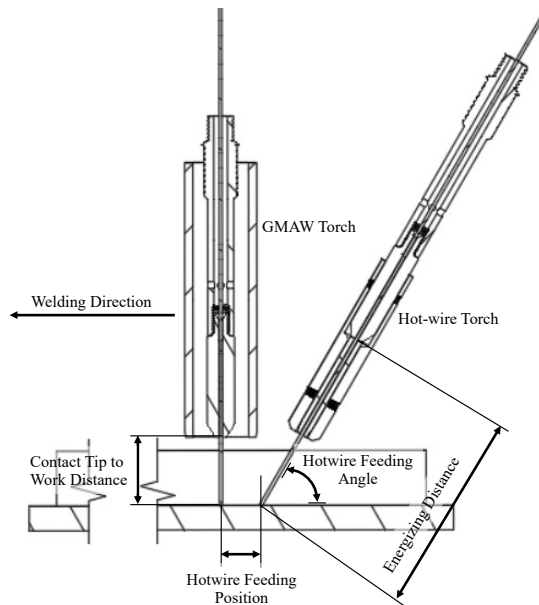


Fig. 4.2 Schematic illustration of hot-wire gas metal arc welding

In the first stage, the solo GMAW process was performed using a deposition rate of 180.12 and 193.70 g/min (equivalent to welding currents of 400A and 500A, respectively) on the second pass to establish two master conditions, referred to as Master A and Master B. The next step involved using the hot-wire insertion technique to increase the deposition rate while minimizing the GMAW fraction. The compensatory condition was achieved by maintaining a constant deposition rate of GMAW at 114.95 g/min, with hot-wire insertion requiring deposition rates of 65.17 and 78.75 g/min for the compensatory condition, referred to as Compensation A and Compensation B. The calculated hot-wire currents from a simplified equation [25, 52] are used to create the exact deposition rates.

In the second stage, the hot-wire fractions of 36.18% and 40.65% were used instead of the previous Master A and B conditions. Subsequently, increasing the hot-wire fractions to 44.05%, 49.60%, and 54.15% by adjusting the hot-wire deposition rates to 90.51 g/min, 113.14 g/min, and 135.57 g/min, respectively. The highest total deposition rate of 250.72 g/min allowed for a 20-mm single-V joint within two weld passes. The weld metals were then examined to assess any detrimental effects of the hot-wire fraction on the properties of the weld metal.

In the third stage, the hot-wire and GMAW fractions were optimized to achieve the highest total deposition rate of 250.72 g/min. This optimization aimed to ensure a sound joint condition while minimizing energy consumption.

Table 4.2 Welding conditions

State 3				Optimized Conditions						
State 2		Hot-wire Fraction and Limitation								
State 1		Hot-wire Compensated Weld Formation								
Process(es) Parameters		GMAW	GMAW	Hot-wire GMAW	Hot-wire GMAW	Hot-wire GMAW	Hot-wire GMAW	Hot-wire GMAW	Hot-wire GMAW	Hot-wire GMAW
	Hot-wire	Hot-wire Current (A)	-	-	188	205	218	241	262	232
Wire Feeding Speed (m/min)		-	-	7.2	8.7	10.0	12.5	15.0	11.4	7.8
Deposition rate (g/min)		-	-	65.17	78.75	90.51	113.14	135.57	103.19	70.60
GMAW	Welding Current (A)	400	500	300				350	400	
	Wire Feeding Speed (m/min)	19.90	21.40	12.70				16.30	19.90	
	Deposition rate (g/min)	180.12	193.70	114.95				147.54	180.12	
Summary	Total deposition rate (g/min)	180.12	193.70	180.12	193.70	205.47	228.10	250.72	250.72	250.72
	Hot-wire Fraction (%)	0	0	36.18	40.65	44.05	49.60	54.15	41.16	28.16
Conditions		(1) Master A	(2) Master B	(3) Compensation A	(4) Compensation B	(5)	(6)	(7)	(8)	(9)
Constant parameters:		GMAW arc voltage 38V Travel Speed 0.3 m/min Contact Tip to Work Distance 25 mm GMAW Torch Waving 3 Hz Energizing Distance 70 mm, Hotwire Feeding Position 10 mm Hot-wire Feed Angle 70° 100%CO ₂ Gas Shielding Flow Rate 25 LPM (GMAW Nozzle) Root pass: Gap 4 mm, Cap pass: Bead width 8-9mm								

Table 4.2 provides the hot-wire fraction of welding condition for all three stages of this experiment. In order to isolate the effect of hot-wire fraction, the following welding and related parameters were held constant shown in the footnote of table 4.2. The molten pool formation and arc phenomenon were observed in detail using a MEMRECAM HX-7 high speed camera with an 810±10 nm band pass filter. The captured condition uses a resolution of 500 fps and a shutter speed was 1/1000 s. The temperature of the molten pool was measured using an R-type contact thermocouple directly placed in the molten pool during welding. The actual current and voltage were determined using a data acquisition system of 5 kHz intervals for collecting from both GMAW and hot-wire. Then, determine the power consumptions.

After the welding process, cross-sectional specimens were prepared for microstructure observation. The specimens were mechanically polished using abrasive papers from 80 to 2000 grits, then final polishing diamond suspension. The

prepared surface was treated with a 2% Nitric acid solution and observed at the center of the weld metal area by an optical microscope (OM), represented in Figure 4.3 (a). For EBSD observations, the specimens were polished using the same as OM method but polishing by a 0.04 μm OPS suspension is required. SEM imaging was conducted at 15 kV with a step size of 0.5 μm . The weld profile geometry, including the fusion area, effective height (H), weld width (W), and weld height (D), was measured to calculate the D/W ratio. The measurement points are shown in Figure 4.3 (a). Vickers hardness test was conducted on the etched surface of the weld metal area. The hardness test was performed using a load of 10 kgf, and the measurement points are indicated by red dot lines in Figure 4.3 (b). For the Charpy impact test, specimens with a thickness and width of 10 mm perpendicular to the welding direction were prepared, as shown in Figure 4.3 (c). The impact test was performed at a temperature of zero degrees Celsius using a hammer speed of 5.5 m/s. The absorbed energy was determined, and liquid nitrogen was used to control the temperature of the specimens during testing. The maximum capacity of the testing machine used was 300J.

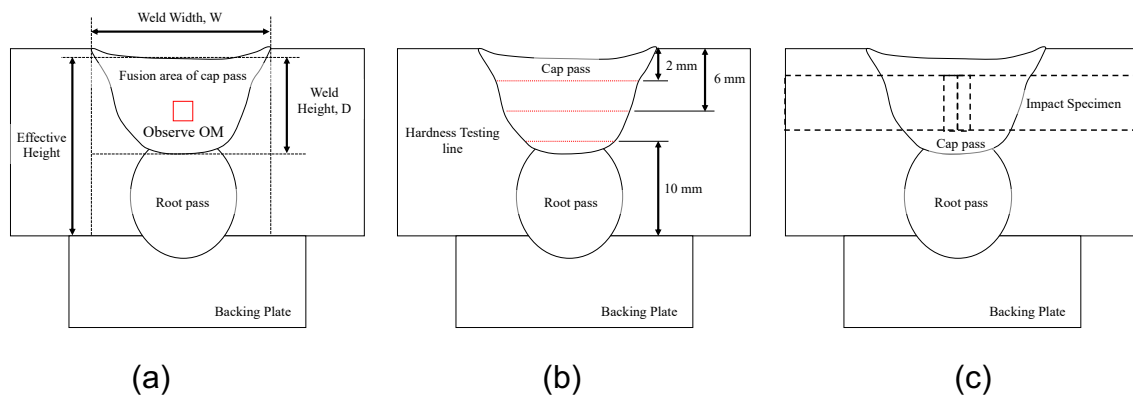


Fig. 4.3 Schematic illustration of (a) weld profile parameters, (b) location of Vickers hardness testing, (c) location of Charpy impact testing

4.3 Calculations

4.3.1 Calculation of hot-wire fraction

Hot-wire insertion was used as independent deposition and intentionally increased which contribute to total deposition volume. Thus, the hot-wire fraction was used to represented its effect which is calculated using equation followed:

$$\%HW = \frac{V_{HW}}{(V_{HW} + V_{GMAW})} \times 100 \quad (4.1)$$

Where %HW is the hot-wire fraction in percent, V_{HW} is the deposition rate of hot-wire mm^3/s , and V_{GMAW} is the deposition rate of GMAW in mm^3/s , V_{GMAW} is the wire feeding speed of GMAW in mm/s which given by

$$V_{HW} = \pi \times 1.2^2 \times v_{HW} \tag{4.2}$$

Substituting equations (4.2) into equation (4.1) to calculate the percentage of hot-wire fraction of total deposition rate.

For the first stage, Figure 4.4 (a) illustrate the hot wire fraction and GMAW fraction in orange and blue areas, respectively. Figure 4.4 (b) depicted the increasing of hot-wire fraction while GMAW fraction remain constant in stage 2 of this experiment. After that, similar total deposition rate at 250.72 g/min while the various fraction between hot-wire and GMAW was shown in Figure 4.4 (c).

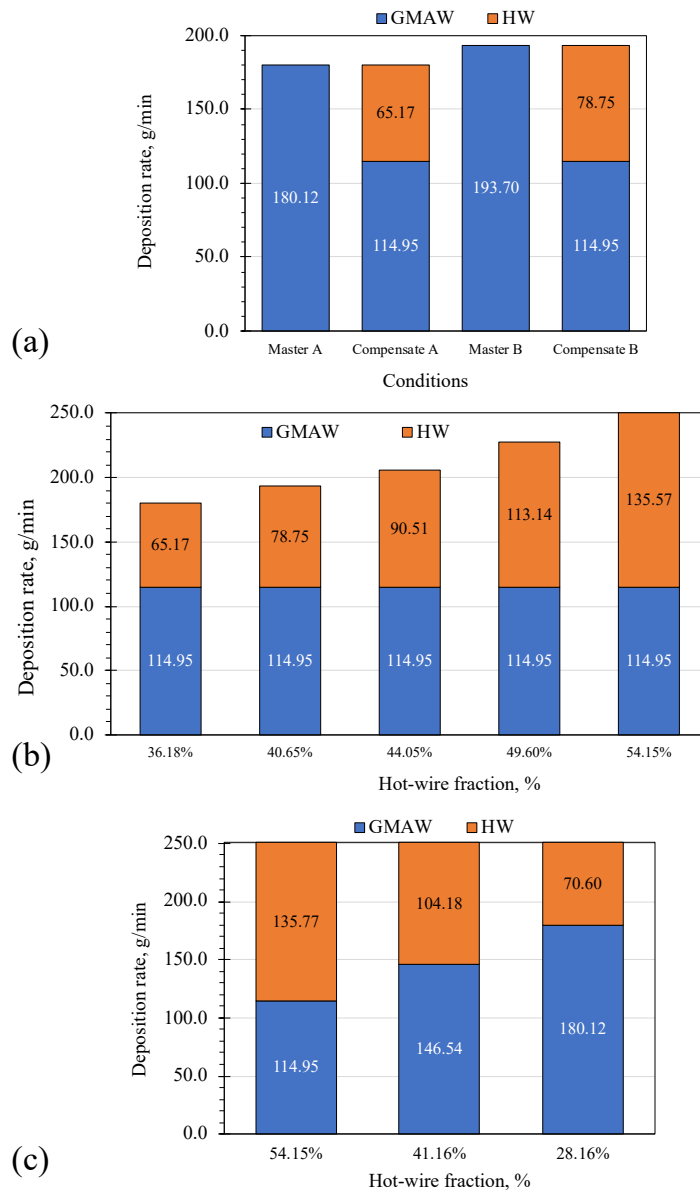


Fig. 4.4 Schematic illustration of hot-wire fraction in gas metal arc welding conditions; (a) First state compensation; (b) Second state limitation; (c) Third state optimization.

4.3.2 Calculation of power consumption

The current and voltage data delivered from an acquisition system of 5000Hz interval. Thus, the benefit using hot-wire insertion will be exposed in term of energy to determine the most efficiency condition. The power consumption will be determined using the equation as followed:

$$P_{total} = (P_{GMAW} + P_{HW}) \times t_{arc} \quad (4.3)$$

$$P_{GMAW} = \frac{(I_{GMAW1} \times V_{GMAW1}) + (I_{GMAW2} \times V_{GMAW2}) + \dots + (I_{GMAW5000} \times V_{GMAW5000})}{5000} \quad (4.4)$$

$$P_{HW} = \frac{\left(\sqrt{I_{HW1}^2} \times \sqrt{V_{HW1}^2} \right) + \left(\sqrt{I_{HW2}^2} \times \sqrt{V_{HW2}^2} \right) + \dots + \left(\sqrt{I_{HW5000}^2} \times \sqrt{V_{HW5000}^2} \right)}{5000} \quad (4.5)$$

Where P_{GMAW} is the power used in GMAW in kJ, P_{HW} is the power used in hot wire insertion (kJ), I_{GMAW} is the welding current (A), V_{GMAW} is the arc voltage (volt), I_{HW} is the hot-wire current (A), and V_{HW} is the hot-wire voltage (volt), and t_{arc} is arc time in s.

4.4 Compensatory condition

4.4.1 Arc phenomenon, bead appearance and weld geometry

The high-speed images in Figure 4.5 demonstrate the effect of hot-wire fraction on the position and shape of molten pool during arc welding. As the hot-wire fraction was increased, the position of the GMAW filler metal tip shifted upward, leading to a larger accumulation of molten metal at the front of molten pool. Additionally, this shift suppressed the penetration of the arc, resulting in a spread of the molten pool to the both sides perpendicular to the welding direction, which yielded a wider bead width. The macro cross-section of the etched surface further demonstrated changes in the shape and geometry of the weld metal resulting from the application of hot-wire.

By applying hot-wire at a similar total deposition rate as conventional GMAW process, the molten pool position shifted upward resulting in a shallower weld depth and wider weld width, as illustrated by the orange and grey bars in Figure 4.6. This led to a reduction in the D/W ratio and fusion area. However, the yellow bar in Figure 5 indicates that a similar effective height could be achieved with hot-wire at the same deposition rate. The author has explained the effect of welding and hot-wire parameters in chapter 3. However, the welding and hot-wire parameters influencing the weld shape was also reported by Tsuyama et al [37] and Wonthaisong et al [38]. This suggests that hot-wire can influence the molten pool formation behavior, which in turn affects the geometry of the resulting weld.

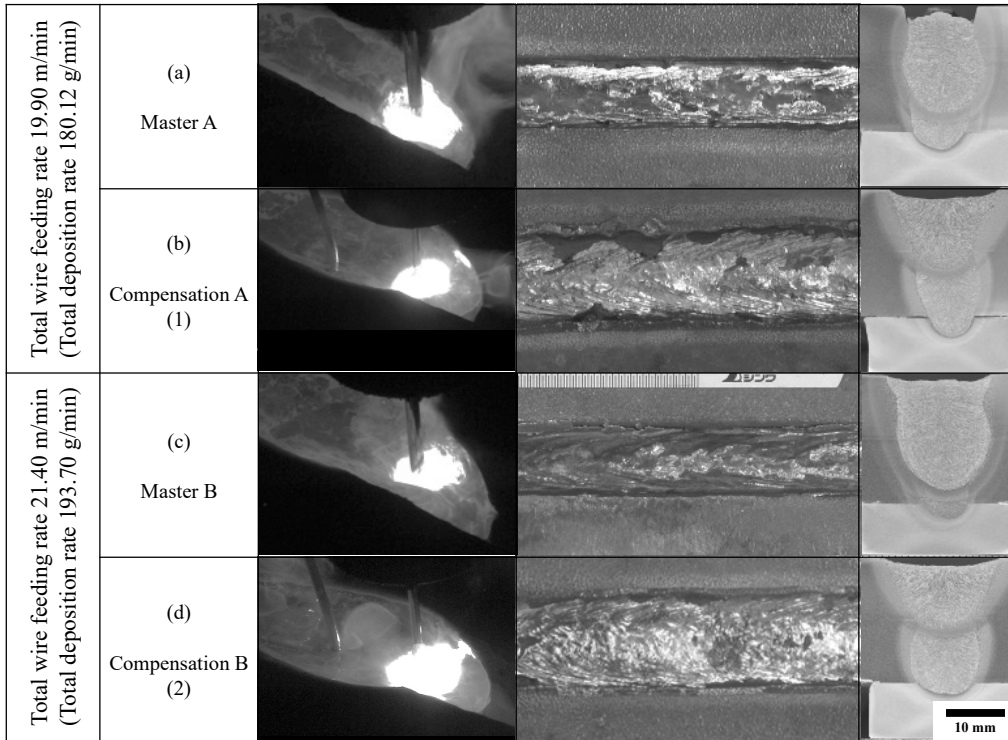


Fig. 4.5 Captured arc observation, bead appearances, and macro cross-sectional of the welds (a) Master A (b) Compensate A (c) Master B and (d) Compensate B

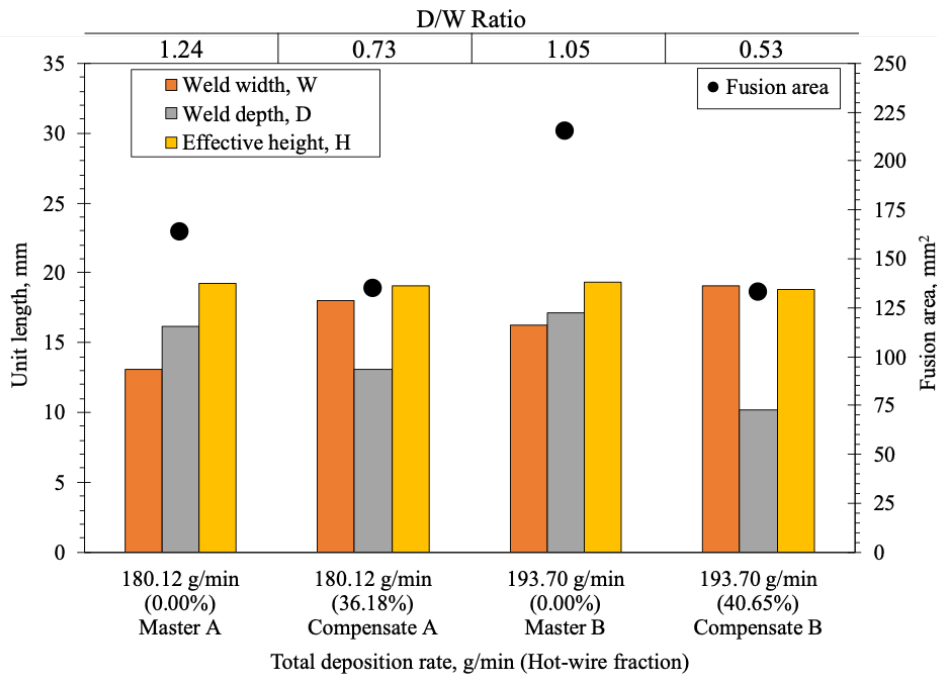


Fig. 4.6 Weld geometry measurement of compensatory stage

4.4.2 Cooling profile and obtained weld metal structure

The cooling profile analysis revealed differences in the cooling behavior of weld metals under two compensation conditions which influences their microstructure variations. Both hot-wire application conditions resulted in faster cooling rates over conventional GMAW, as illustrated in Figure 4.7. Specifically, at a total deposition rate of 180.12 g/min, the cooling rate increased from 14.02 to 22.69 °C/s, while at 193.70 g/min, it increased from 9.38 to 19.25 °C/s. The faster cooling rates resulted in a lower fraction of grain boundary ferrite (GBF) and Widmanstätten ferrite or side plate ferrite (SPF) but a higher fraction of acicular ferrite (AF), consistent with previous reports [7,37,69, 109-111].

However, the comparison between compensation A and B showed that the increasing hot-wire fraction while the GMAW fraction remains constant, resulting in extended cooling time because the total deposition volume rose. Consequently, the microstructure obtained from hot-wire GMAW consisted of predominates AF with a little more GBF and SPF at a higher hot-wire fraction.

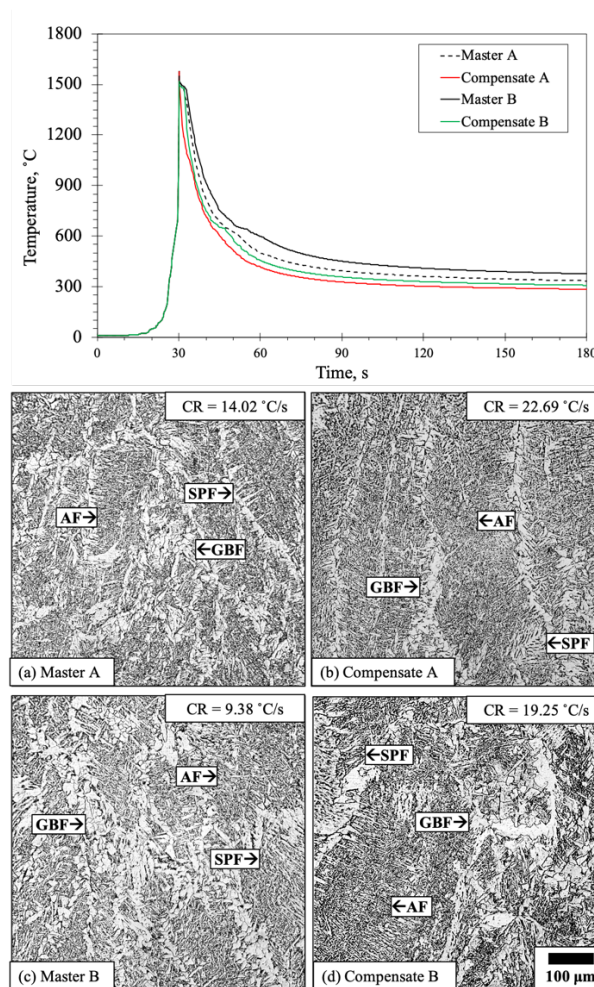


Fig. 4.7 Cooling profile and weld metal microstructure
(a) Master A (b) Compensation A (c) Master B (d) Compensation B

4.4.3 Mechanical properties of joint and power consumption

The use of hot-wire GMAW in welding showed significant improvements in the hardness and absorption energy of the resulting weld metal, as seen in Figure 4.8 (a). These enhancements are attributed to the increasing AF in the weld metal, supported by previous research [7, 109-111]. The higher proportion of AF enables the weld metal to withstand applied loads and deformation. It's worth noting that the as-welded mechanical properties achieved with hot-wire GMAW surpass those obtained with conventional GMAW, eliminating the need for additional post-weld heat treatment. These findings suggest that hot-wire insertion can effectively compensate for the total deposition rate and enhance the mechanical properties of the weld metal.

Moreover, the compensated fraction allows obtaining a similar deposition rate with less power consumption, as seen in Figure 4.8 (b) At 180.12 g/min of total deposition rate, power consumption was reduced by approximately 24%. Additionally, power consumption can be saved up to 39% at 193.70 g/min of total deposition rate, highlighting the advantage of hot-wire insertion. However, it is important to investigate the occurrence of grain boundary ferrite fraction when applying the hot-wire technique to ensure the desired weld metal structure, while also minimizing power consumption for sustainable development.

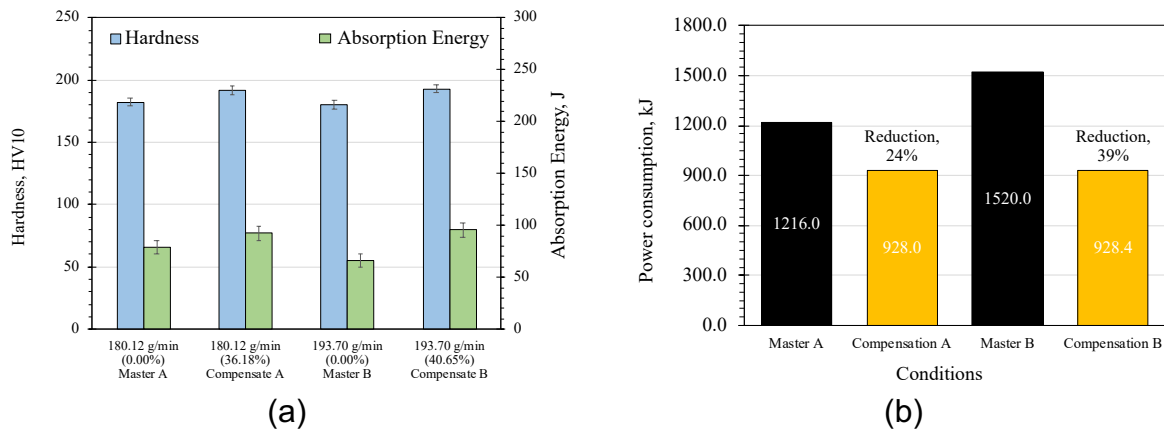


Fig. 4.8 Joint properties and their power consume; (a) Vickers hardness and absorbed energy; (b) Power consumption

4.5 Limitation of hot-wire fraction

4.5.1 Arc phenomenon and bead appearance

Figure 4.9 demonstrates the motion capture during hot-wire GMAW process. Increasing hot-wire fraction while GMAW fraction held constant lead more accumulated molten metal at the molten pool front and cause a shift in the arc position upwards. A high-speed camera can detect the occurrence of molten metal precedence when hot-wire fraction reached 54.15% of the total deposition rate. This

result conformed to the reported limit of using the hot-wire GMAW on a 7-mm gap size of a single-v butt joint whereas the molten metal precedence occurred when the hot-wire fraction was over 51.22% [40]. Bead appearances also showed irregular bead shapes which is obvious evidence of molten metal precedence [38,39].

Figure 4.10 illustrates the visual presentation of the development of molten metal behavior at a hot-wire fraction of 54.15%. Initially, the molten pool was raised due to the additional deposit volume from the hot-wire insertion (a). Subsequently, more molten metal accumulated at the front of the molten pool (b). The molten pool front extended and flowed ahead of the arc position (c). Eventually, the lifted molten pool collapsed at the front, resulting in a long molten metal precedence, while the arc shifted downward (d).

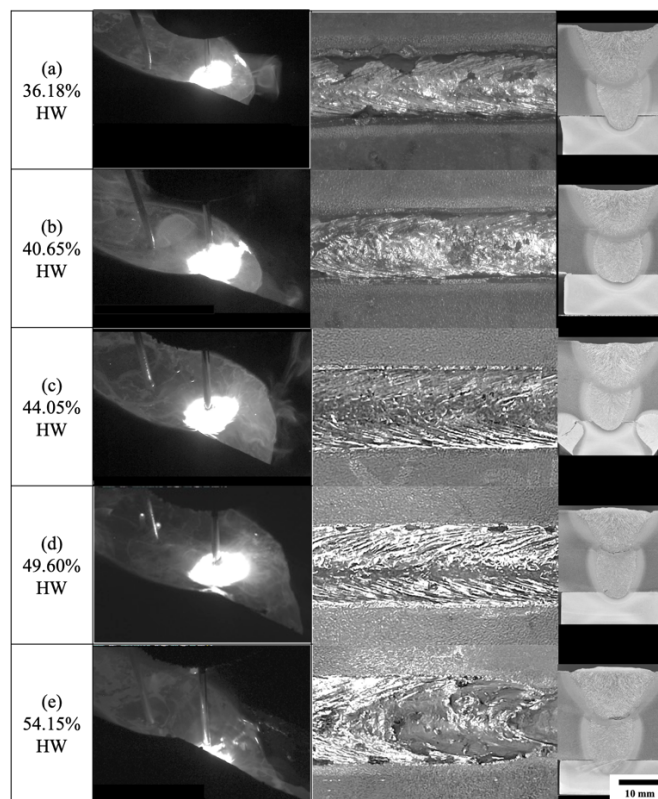


Fig. 4.9 Captured arc observation and bead appearances (a) 36.18%HW (b) 40.65%HW (c) 44.05%HW (d) 49.60%HW (e) 54.15%HW

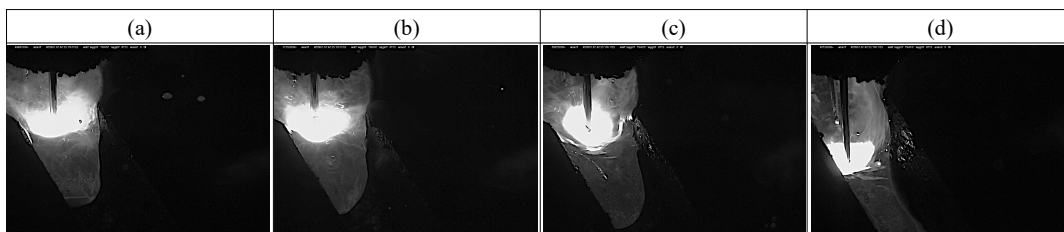


Fig. 4.10 Molten metal development: (a) molten pool rose; (b) accumulated molten pool front; (c) extended molten pool front; (d) collapsed

4.5.2 Cooling profile and obtained weld metal geometry and microstructure

Increasing the hot-wire fraction in Figure 4.11 (a) extended the cooling time, leading to a decrease in the cooling rate from 22.69°C/s (36.18% hot-wire fraction) to 13.16°C/s (54.15% hot-wire fraction) because of the increased total deposition volume (hot-mass). Macro-etching of the cross-section revealed a lack of fusion (LOF) at the interlayer of the weld metal produced using a 49.60% hot-wire fraction, which cannot be detected by a high-speed camera. This unexpected LOF raises concerns about the limitations and the assurance of soundness. Figures 4.11 (b), (c), and (d) display the microstructure development at different hot-wire fractions: 44.05%, 49.60%, and 54.15%, respectively. As the cooling rate decreased, the fraction of AF reduced. The microstructure fractions underwent changes, with SPF and GBF becoming the predominant fractions. The extended cooling time due to hot-wire insertion resulted in an increased driving force for planar growth inward of GBF within the temperature range of 650 to 600°C [7, 69-72, 75]. Simultaneously, the lack of fusion led to a decrease in non-metallic inclusions, thereby significantly decreasing the nucleation sites for AF. However, further investigation is required to determine the nucleation density in the weld metal influenced by the hot-wire fraction.

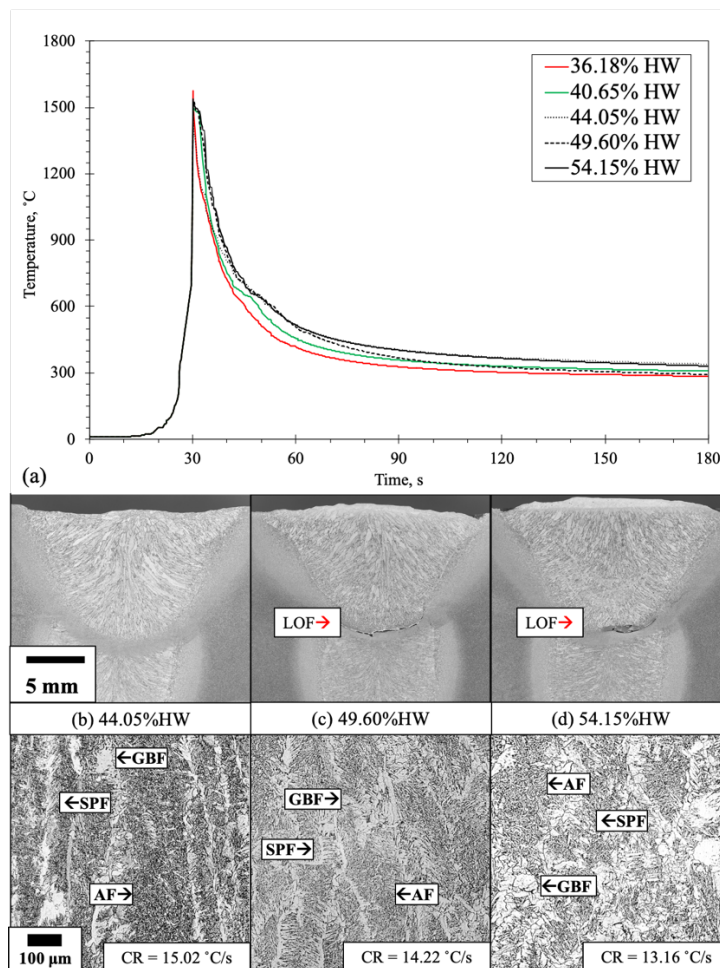


Fig. 4.11 Cooling profile and weld metal microstructure
(a) 44.05%HW (b) 49.60%HW (c) 54.15%HW

Figure 4.12 demonstrates the measured weld geometry at various hot-wire fractions while maintaining a constant GMAW fraction. The yellow bars indicate the effective height, showing that only 49.60% and 54.15% of hot-wire fractions resulted in weld reinforcement. However, due to incomplete fusion at the interlayer, the precise weld depth under these conditions cannot be determined. Thus, the red bars represent the weld height from the weld cap to the end of the fusion zone in the thickness direction.

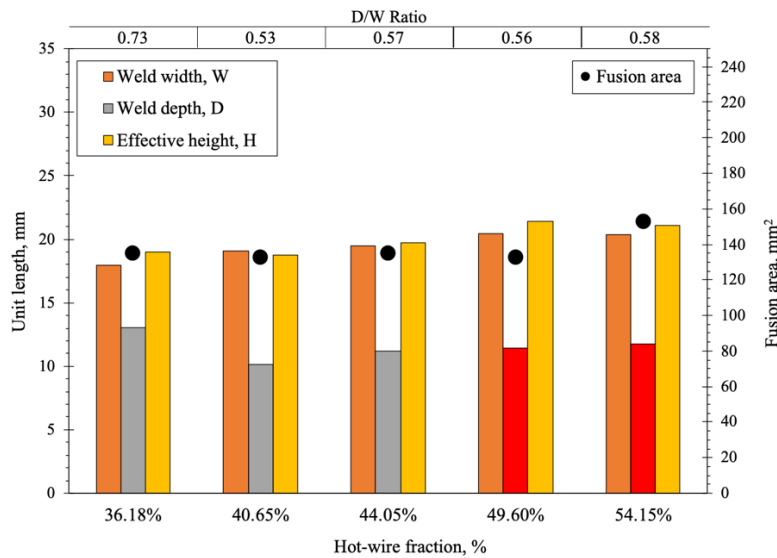


Fig. 4.12 Weld geometry measurement of limitation stage

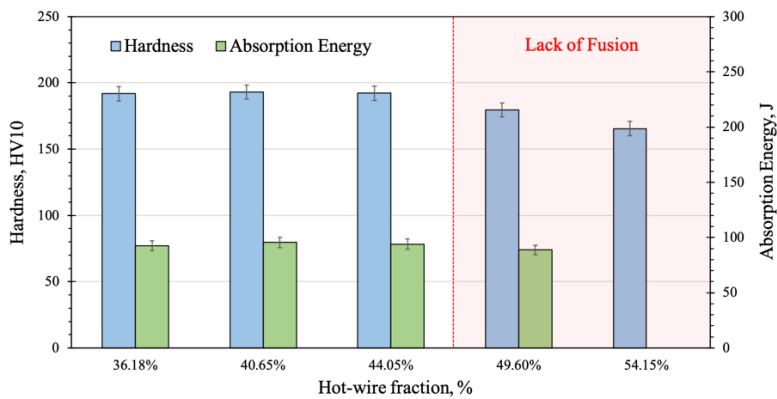


Fig. 4.13 Hardness and absorption energy from limitation stage

4.5.3 Mechanical properties of joint

Figure 4.13 shows the results of the Vickers hardness test conducted on the etched surface of the weld metal area, represented by the blue bars. Within the hot-wire fractions ranging from 36.18% to 44.05%, similar hardness values were observed. Beyond this range, the hardness decreased. The green bars represent the absorption energy obtained from the Charpy impact test, which exhibited a similar

value for hot-wire fractions ranging from 36.18% to 44.05%. These mechanical properties correspond to the predominant microstructures discussed earlier. Increasing GBF and SPF fractions typically result in lower toughness compared to AF. The unique needle-like morphology of AF provides good resistance to crack propagation [7, 69-72, 75]. The larger grain sizes of GBF and SPF were obtained due to the slow cooling rate caused by excessive hot-wire fractions leading to undesirable impact toughness.

Unfortunately, the condition with a 54.15% hot-wire fraction could not be tested due to significant incomplete fusion. As a result, the 49.60% hot-wire fraction exhibited the lowest absorption energy in this subsequent experiment. In conclusion, the author recommended limiting the hot-wire fraction to 44.05% of the total deposition rate. For the same wire diameter, the wire feed speed ratio between GMAW and hot wire should be 1:0.787. These parameters were found to optimize the mechanical properties of the weld metal.

4.6 Optimization condition

4.6.1 Arc phenomenon and bead appearance

The author proposed a solution to address the lack of fusion and irregular bead shape issues resulting from excessive hot-wire fraction while maintaining a constant total deposition rate of 250.72 g/min. In this approach, single-V butt joints of 20-mm thick steel plates can be welded using only two weld passes. Arc observation using a high-speed camera revealed a downward shift in the arc position, as shown in Figure 4.14. These adjustments successfully corrected the irregular bead shape problem.

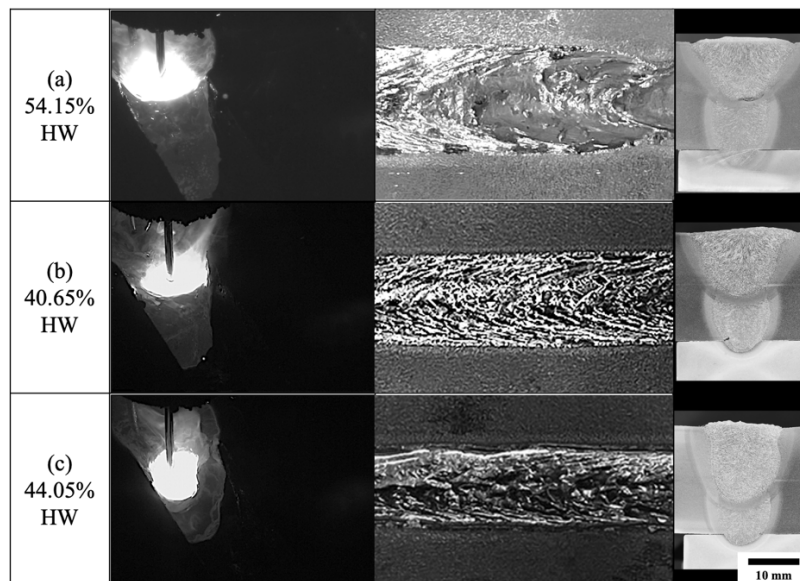


Fig. 4.14 Captured arc observation and bead appearances
(a) 54.15%HW (b) 41.16%HW (c) 28.16%HW

4.6.2 Cooling profile and obtained weld metal geometry and microstructure

Increasing the GMAW fraction led to an increase in the welding current. Consequently, heat input was increased and affected the cooling profile and the cooling time from 800°C to 500°C. Figures 4.15 (b), (c), and (d) illustrate the microstructures of the weld metal obtained with hot-wire fractions of 54.15%, 41.16%, and 28.16% of the total deposition rate of 250.72 g/min, respectively. Without experiencing a lack of fusion, the predominant presence of GBF and SPF transformed into a predominantly acicular ferrite (AF), even at a slower cooling rate.

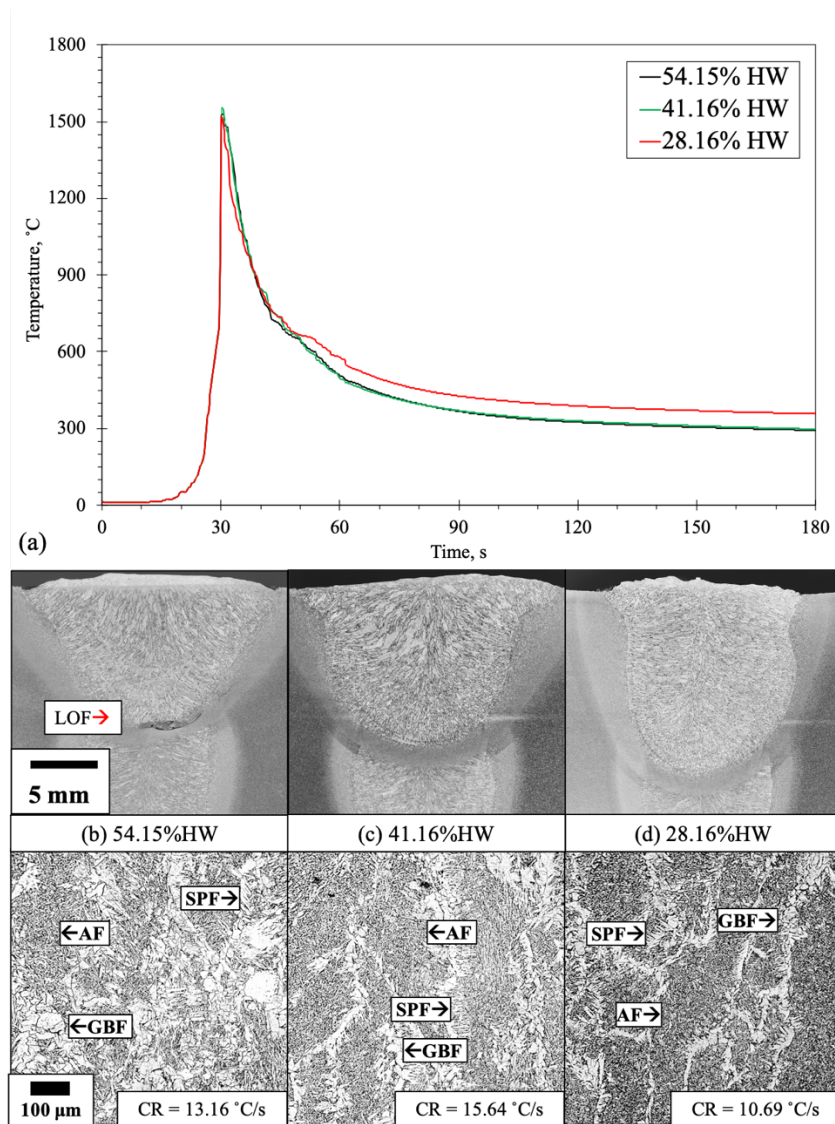


Fig. 4.15 Cooling profile and weld metal microstructure
 (a) 54.15%HW (b) 41.16%HW (c) 28.16%HW

All these three conditions at 250.72 g/min of total deposition rate provided a similar effective height with a reinforcement at the weld cap as indicated with the yellow bar in Figure 4.16. Moreover, reduced hot-wire fraction while the total

deposition rate was held constant, provided narrower weld width and deeper weld depth compare to the original hot-wire fraction at 54.15%HW. This increases the obtained D/W ratio and fusion area. Optimizing the ratio between GMAW and HW not only achieved the desired deposition rate, but also modified the shape and position of the weld metal in the thickness direction.

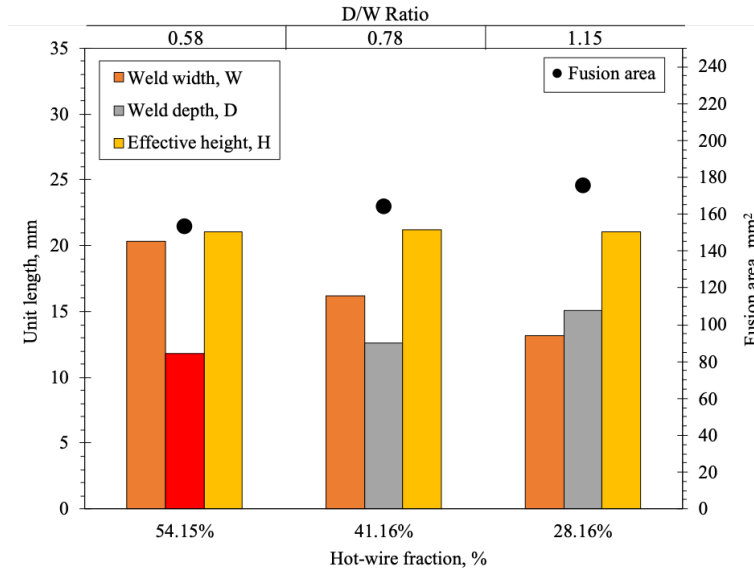


Fig. 4.16 Weld geometry measurement of hot-wire optimized condition stage

In summary, by carefully adjusting the hot-wire fraction and employing the proposed methodology, the issues of lack of fusion and irregular bead shape were effectively addressed, resulting in improved weld bead appearances and the desired microstructures.

4.6.3 Mechanical properties of joint and power consumption

The optimized ratio between hot-wire and GMAW fractions yielded significant improvements in hardness value and absorption energy. Figure 4.17 (a) demonstrates that a hot-wire fraction of 41.16% resulted in enhanced absorption energy, indicated by the green bar. The power consumption for solo GMAW, providing a deposition rate of 250.72 g/min, is shown by the black bar in Figure 4.17 (b). The power consumptions for the three optimized conditions are presented. The condition with a 54.15% hot-wire fraction, which led to a lack of fusion, is represented by the red bar. Notably, the 41.16% hot-wire fraction exhibited the lowest power consumption, with approximately a 62% reduction compared to solo GMAW at a similar deposition rate. In conclusion, the findings identify the best-optimized condition for achieving a sound 20-mm single-V butt joint, accompanied by a substantial 62% reduction in power consumption, while maintaining desired joint properties.

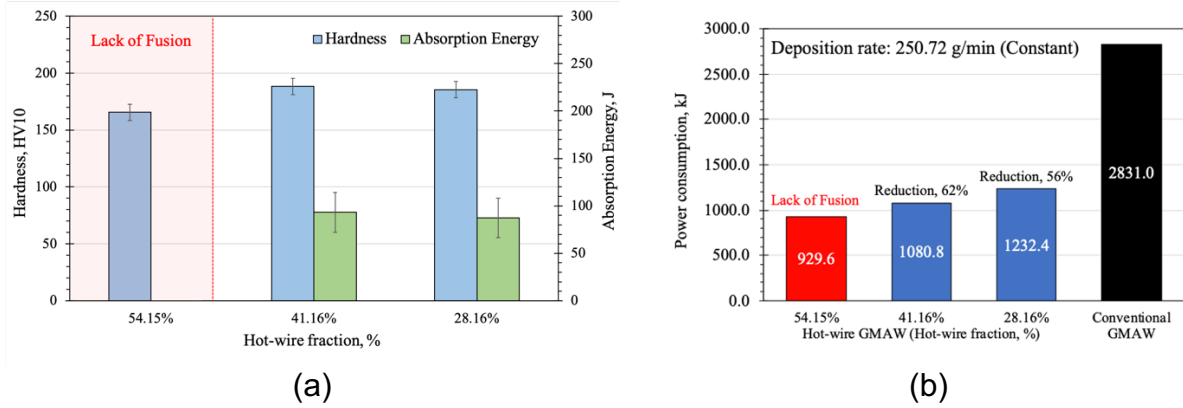


Fig. 4.17 Joint properties and their power consume; (a) Vickers hardness and absorbed energy; (b) Power consumption

4.7 Advance microstructure evaluation

In the previous section, using a hot-wire fraction of 41.16% resulted in the lowest energy consumption while achieving a single-V butt joint on a 20-mm thick steel plate with only two weld passes. However, the absorption energy of the weld metal produced with a 54.15% hot-wire fraction is null due to significant incomplete fusion. Electron backscatter diffraction (EBSD) analysis was conducted to gain insight and emphasize the lowest energy consumption condition on weld metal samples with 54.15% and 41.16% hot-wire fractions.

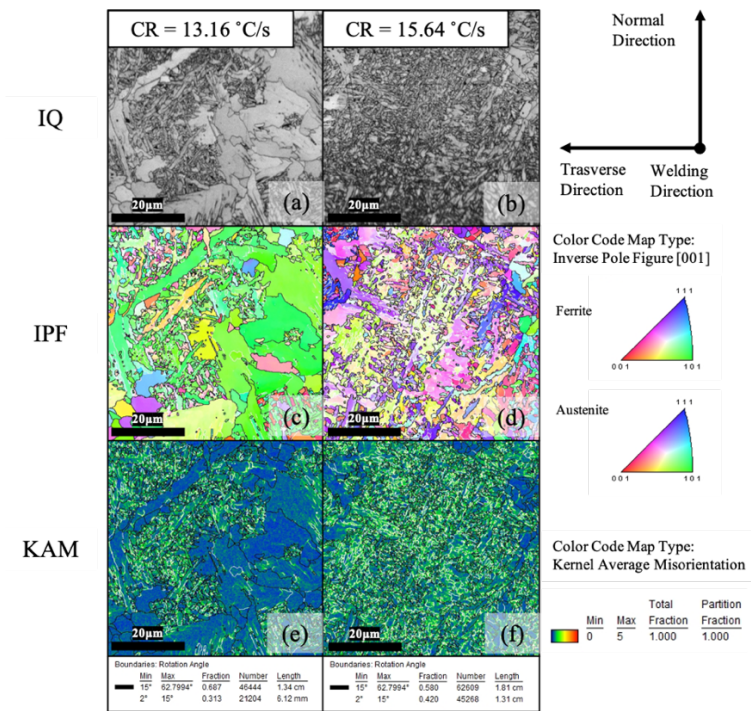


Fig. 4.18 Comparison of EBSD results: IQ maps (a) and (b); IPF maps (c) and (d); KAM map (e) and (f).

EBSD image quality maps revealed a mixture of ferrite morphologies. Figure 4.18 (a) shows predominantly GBF and SPF in the weld metal with a 54.15% hot-wire fraction, while Figure 4.17 (b) depicts a predominantly AF in the weld metal with a 41.16% hot-wire fraction. The image pole figure maps demonstrated a greater variety of AF orientations and an increased total grain boundary length, indicating enhanced resistance to deformation and crack propagation, thereby leading to improved mechanical properties. Figure 4.18 (e) and (f) present the kernel-average misorientation (KAM) maps, where the needle-like shape of AF resulted in higher KAM values compared to polygonal ferrite, GBF, and PSF. The brighter shade represents a higher dislocation density in the AF region.

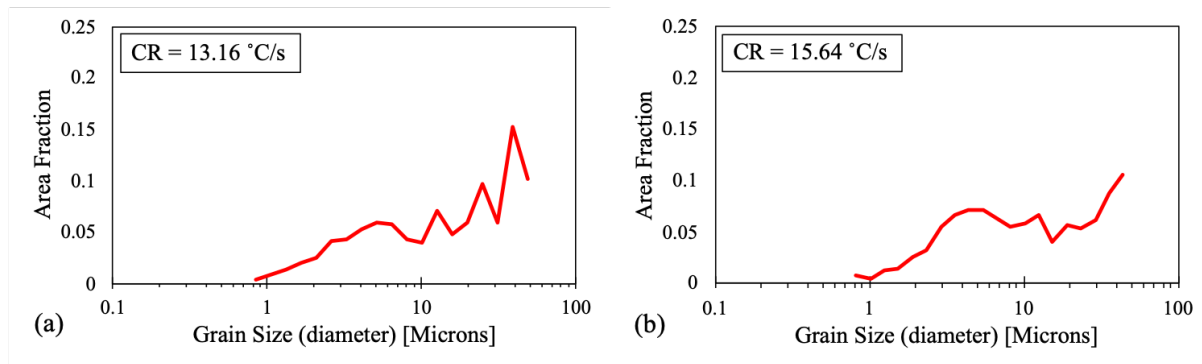


Fig. 4.19 Average grain size fraction from weld metal produced from; (a) 54.15% hot-wire; (b) 41.16% hot-wire.

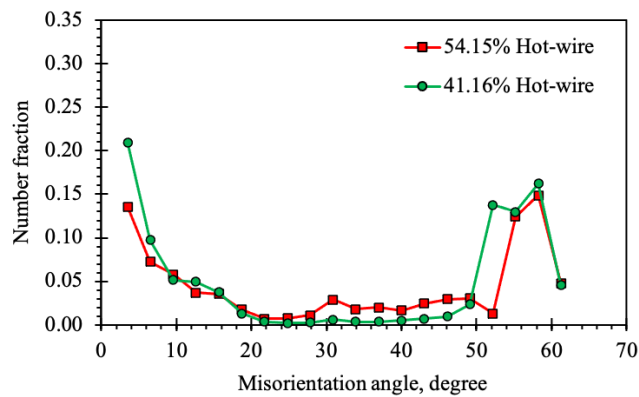


Fig. 4.20 Average grain size fraction from weld metal produced from 54.15% and 41.16% hot-wire fraction.

Figure 4.19 shows the average grain size fraction, with the weld metal from the 41.16% hot-wire fraction exhibiting a larger proportion of smaller grain sizes compared to the weld metal from the 54.15% hot-wire fraction. The misorientation angle profile also revealed distinct differences between the two conditions. Figure

4.20 demonstrates the average misorientation angle, with a high fraction of misorientation angles similar to 50 and 60 degrees [94,101,112]. Misorientation angles between 25 and 45 degrees were also detected, indicating the presence of mixed polygonal ferrite with AF in the weld metal area [94,101,112]. The weld metal produced with a 41.16% hot-wire fraction exhibited a higher fraction of AF and a predominant presence of misorientation angles at 50 and 60 degrees. These findings align with previous reports by Gourgues et al. [101], Diaz-Fuentes et al. [102], Jorge et al. [94], and Shrestha et al. [112]. In conclusion, the EBSD analysis provided valuable complementary information to optical microscopy and mechanical properties analysis, emphasizing the optimized condition with a 41.16% hot-wire fraction.

4.8 Conclusion

The effect of hot-wire fraction on the butt joint of 20-mm thick steel plate was systematically investigated. The study employed a high-speed camera to monitor the welding process, which detected the molten metal precedence leading to lack of fusion. The cooling profiles and microstructure analysis helped determine the limitations of hot-wire fraction and establish the optimal fraction to enhance joint quality. The conclusions are as follows:

(1) Hot-wire insertion improves weld metal properties and can compensate for desired deposition rate compared to conventional GMAW.

(2) Motion analysis using a high-speed camera identified the molten metal precedence, which can be avoided with the proper deposition rate.

(3) When the GMAW deposition rate was held constant at 114.95 g/min, exceeding 44.05%HW led to lack of fusion and larger GBF fraction, resulting in poor joint properties.

(4) The optimized condition between GMAW and HW fraction provided a soundness joint with improved mechanical properties using a 250.72 g/min with a 41.16%HW.

(5) Soundness condition for 20-mm thick steel plate can be achieved using only 2 weld passes with a 62% reduction in power consumption.

(6) The EBSD analysis highlighted the optimized condition with a 41.16% hot-wire fraction, which not only ensured joint soundness but also resulted in a predominantly acicular ferrite (AF) microstructure, contributing to higher mechanical properties.

Chapter 5

An improvement of weld metal properties with selective hot-wire filler metal during GMAW process

5.1 Introduction

The previous chapter clarified the controllability of hot-wire application during the Gas Metal Arc Welding (GMAW) process. This chapter aims to investigate the impact of selective hot-wire on welded joint properties. In this study, different filler wires with varying Ni content were intentionally selected to evaluate their effect on microstructure evolution, material characteristics, and fracture behavior. The welding quality was monitored using a high-speed camera, and the welded profile geometry on an etched cross-section was measured in detail. The results showed that an increase in Ni content significantly increased the fraction of acicular ferrite in the weld metal, which improved joint properties such as hardness and absorption energy.

5.2 Materials and methods

5.2.1 Materials

A single-v butt joint of K36E-TM (490MPa-class) having a length of 400 mm, width of 40 mm, and thickness of 20 mm was assembled with a backing plate having a length of 420 mm, width of 25 mm and thickness of 9 mm. A butt joint has 30 degree of groove angle with a root gap of 4 mm as shown in Figure 5.1. The filler metal used for GMAW was ER70S-G (AWS A5.18, JIS Z3312 G49A0UC11), solid wire with a diameter of 1.2 mm. whereas the filler wires with different Ni content were used as hot-wire filler metal are following: 0.00% Ni of ER70S-G (AWS A5.18, JIS Z3312 G49A0UC11), 0.98%Ni of ER80S-G (AWS A5.28, JIS Z3312 G57AP6MN2MIT), and 2.87%Ni of ER110S-G (AWS A5.28). Chemical composition of the materials used in this experiment are given in table 5.1.

Table 5.1 Chemical compositions of materials being used in this chapter

Materials		Chemical composition (%wt)										
		C	Si	Mn	P	S	Cu	Ni	Cr	Ti+Zr	Mo	Fe
Base metal K36E-TM		0.12	0.20	1.21	0.140	0.04	0.01	0.01	0.02	0.00	0.00	Bal.
Filler metal	0.00%wt Ni wire ER70S-G	0.04	0.73	1.58	0.010	0.01	0.23	0.00	0.00	0.22	0.00	Bal.
	0.98%wt Ni wire ER80S-G	0.05	0.39	1.10	0.007	0.005	0.01	0.98	0.00	-	0.22	Bal.
	2.87%wt Ni wire ER110S-G	0.07	0.28	1.36	0.006	0.003	0.01	2.87	0.47	-	0.29	Bal.

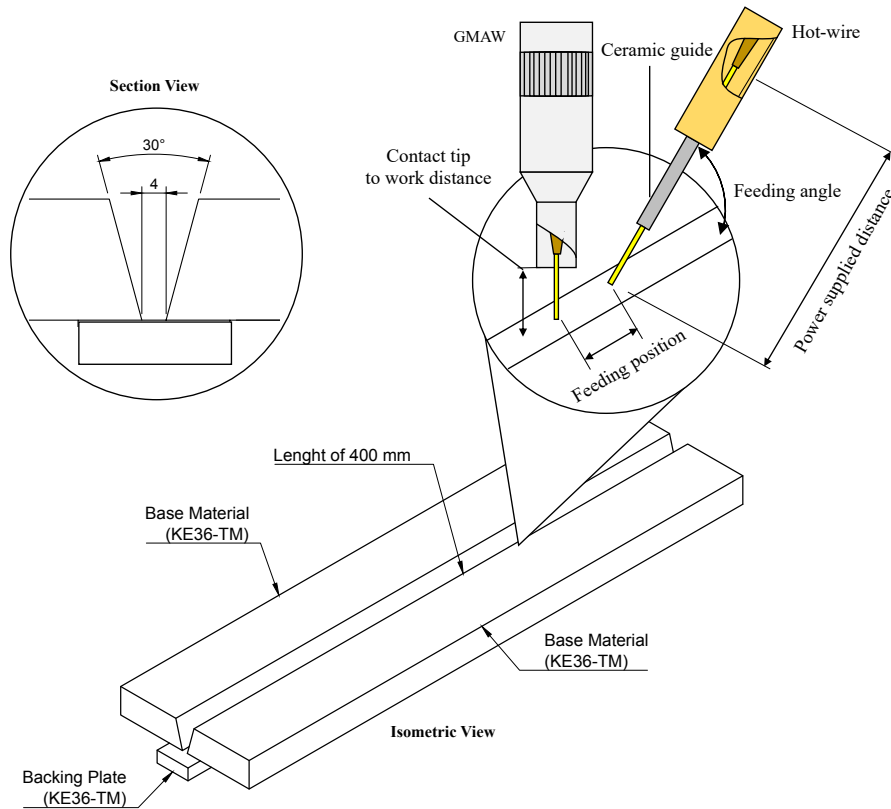


Fig. 5.1 Joint configuration

The hot-wire GMAW with 100% CO₂ shielding gas was installed by placing the GMAW torch perpendicular to the welding direction and backing plate with a 10-mm delay of the hot-wire feeding position in the welding direction. The contact tip to work distance and power supply distance were held constant at 25 and 100 mm, respectively. The hot-wire feeding angle were maintained at 70 degree relative to the backing plate.

5.2.2 Methodology

Initially, GMAW was performed without hot-wire insertion to create a baseline condition, using a deposition rate of 114.95 g/min (equivalent to a welding current of 300A) on the root pass. After that, a solo GMAW was applied using a deposition of 193.70 g/min (equivalent to a welding current of 500A) to create a Master condition. The next step involved using the 78.75 and 114.95 g/min of hot-wire and GMAW feeding rate, respectively, to create a weld pass on second layer. The different Ni content of filler wires were used as a hot-wire filler metal. Table 5.2 gives the welding conditions in this experiment. The subsequent samples, HW-1, HW-2, and HW-3, were created by using hot-wire filler metals with Ni contents of 0.00%wt, 0.98%wt, and 2.87%wt, respectively. Figure 5.2 shows the relationship between hot-wire feeding speed and hot-wire current calculated from equation 3.4.

Table 5.2 Chemical compositions of materials being used in this chapter

Process	Parameters	1 st Layer	2 nd Layer			
		Root pass	Conventional	0.00% Ni	0.98% Ni	2.87% Ni
Hot-wire	Hot-wire Current (A)	-	-	205	195	185
	Wire Feeding Speed (m/min)	-	-	8.7		
	Deposition rate (g/min)	-	-	78.75		
GMAW	Welding Current (A)	300	500	300		
	Wire Feeding Speed (m/min)	12.70	21.40	12.70		
	Deposition rate (g/min)	114.95	193.70	114.95		
Summary	Total deposition rate (g/min)	114.95	193.70	193.70		
	Hot-wire Fraction (%)	-	0	40.65		
Constant parameters:						
GMAW arc voltage 38V		Energizing Distance 70 mm, Hotwire Feeding Position 10 mm				
Travel Speed 0.3 m/min		Hot-wire Feed Angle 70°				
Contact Tip to Work Distance 25 mm		100%CO ₂ Gas Shielding Flow Rate 25 LPM (GMAW Nozzle)				
GMAW Torch Waving 3 Hz		Root pass: Gap 4 mm, Cap pass: Bead width 8-9mm				

The arc phenomenon and molten pool formation were observed using a MEMRECAM ACS1 NAC high-speed camera. A band pass filter with a transmission wavelength of 810 ± 10 nm was attached to an optical lens. A shutter speed of 1/1000 s and a frame rate of 500 fps were adopted. The resulting welds were cross-sectionally cut, polished with abrasive paper up to 3000 grit, then by a final polishing with 6 μ m and 1 μ m diamond suspension, and etched with 3% nitric acid. Subsequently, the weld geometry was observed. Figure 5.3 (a) shows measured parameter of the weld geometry, such as the fusion area (A), effective height (H), weld depth (D), and weld width (W), on the obtained welded cross-section.

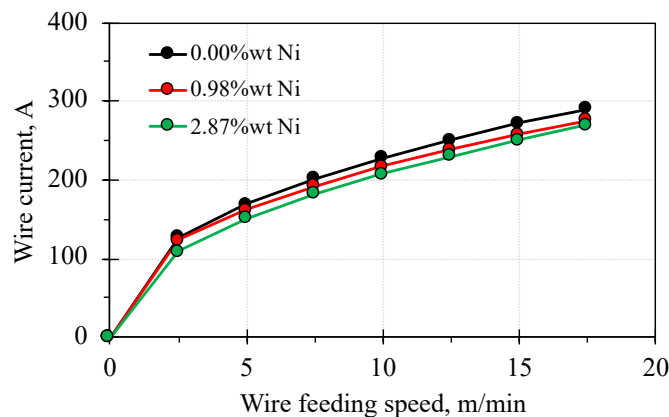


Fig. 5.2 Appropriated hot-wire currents

After that the cross-section of the obtained joints was observed by optical microscope (OM) and scanning electron microscope (SEM), equipped with electron backscatter diffraction (EBSD) as illustrated the observed position in Figure 5.3 (b). For the EBSD observations, the specimens were polished with the same mentioned method but the 0.04 μ m OPS suspension is required without etching, the SEM was operated at 15 kV, and the step size was 0.5 μ m. Figure 5.2 (c) illustrates testing

positions of Vickers hardness test was performed on the cross-section specimens and a horizontal direction perpendicular to the welding direction at a load of 9.8 N for a holding time of 10 s. The interval of the measurement was 2 mm. The impact test was carried out at a hammer speed of 5.5 m/s at the temperature of 0 °C (maximum energy capacity of 300J). The temperature of the specimen was controlled using liquid nitrogen. After the impact test, the fracture surfaces of the specimens fabricated with the different filler wires were examined by SEM.

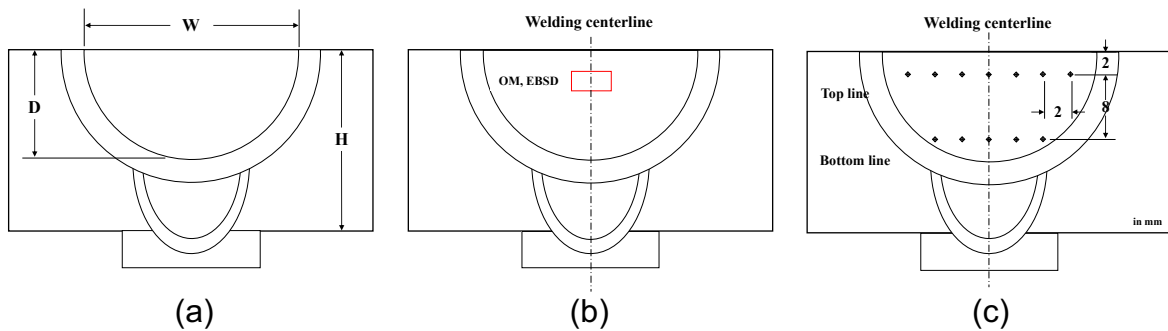


Fig. 5.3 Observation position:
 (a) weld profile geometry; (b) OM, SEM, and EBSD; (c) Vickers hardness

5.3 Effect of welding process on welded specimens

5.3.1 Arc phenomenon, bead appearance and weld geometry

The high-speed images in Figure 5.4 demonstrate the arc observation during welding. The arc can be generated smoothly without arc blow or stubbing arc. The molten pool was shifted upward in thickness direction and suppressed the penetration of arc during hot-wire GMAW, similar behavior as in chapter 4. Thus, the top-view of bead appearances show wider bead width. The macro cross-section of the etched surface further demonstrated changes in the shape and geometry between conventional GMAW and hot-wire GMAW.

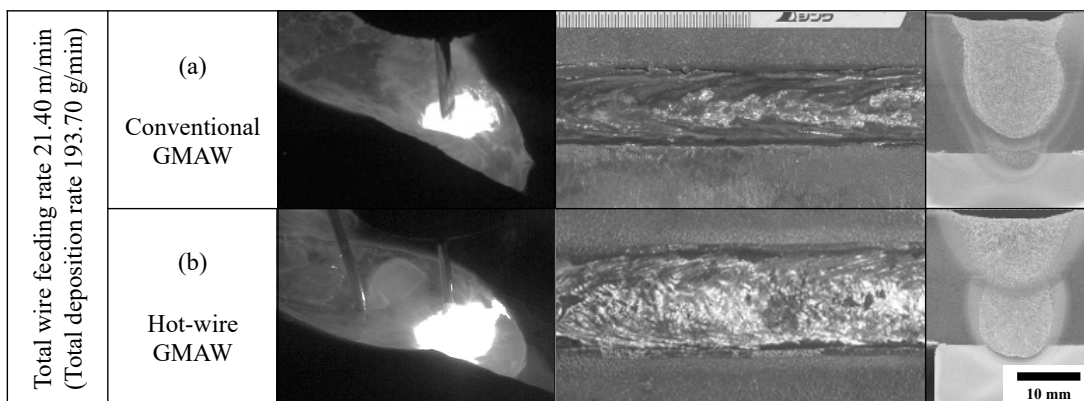


Fig. 5.4 Arc observation, bead appearance, and weld profile:
 (a) Conventional GMAW; (b) Hot-wire GMAW

By applying hot-wire at a similar total deposition rate, the reduction in the D/W ratio and fusion area similar to the previous chapter could be obtained. Moreover, a similar effective height confirmed the high controllability of hot-wire insertion system as illustrated in Figure 5.5.

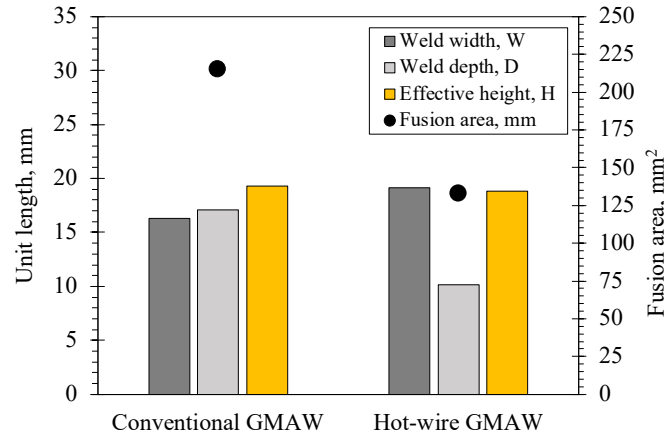


Fig. 5.5 Measured weld profiles geometry

5.3.2 Cooling profile and obtained weld metal structure

Figure 5.6 (a) compares the cooling profiles obtained from conventional GMAW and hot-wire GMAW at the same total deposition rate. The results indicate that hot-wire GMAW leads to a faster cooling rate due to the primary heat source of GMAW requiring less power. Figures 5.6 (b) and (c) reveal the heterogeneous microstructures associated with different cooling rates. In conventional GMAW, the weld metal mainly consists of grain boundary ferrite (GBF) and a mixture of acicular ferrite (AF), polygonal ferrite, Widmanstätten ferrite, or side plate ferrite (SPF) as shown in Figure 5.6 (b). However, when the cooling rate is increased from 9.38 to 19.25 °C/s with hot-wire application, the proportion of GBFs decreases, and SPFs replace them, as depicted in Figure 5.6 (c). The needle-like AFs randomly formed and distributed within the grains. The formation of AFs, which requires a higher degree of undercooling, is facilitated under lower heat input conditions. These findings are consistent with previous studies [7, 69-71, 79, 108].

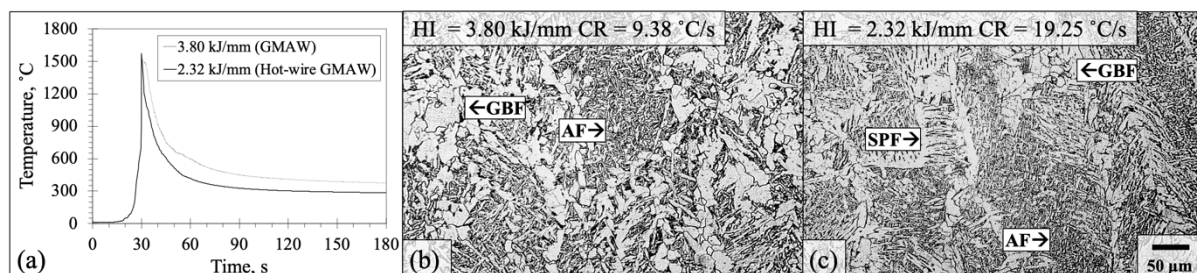


Fig. 5.6 Cooling profile and obtained microstructure:
(a) Cooling profile; (b) Conventional GMAW; (c) Hot-wire GMAW

Figure 5.7 compares the acicular ferrite (AF) fraction obtained from conventional GMAW (Figure 5.7 (a)) and hot-wire GMAW (Figure 5.7 (d)) using image quality maps from EBSD results. Conventional GMAW produces more fraction of non-needle AF, while hot-wire GMAW results in a significant amount of needle-like AF. The use of hot-wire insertion and the resulting faster cooling rate contribute to a higher grain boundary density and enhance resistance to deformation [78,80] because the grain boundaries act as obstacles to dislocation movement, enhancing the strength and toughness of a material. More grain boundaries provide more barriers for dislocations to interact with, leading to increased strength and improved resistance to deformation. Additionally, higher grain boundary density can promote grain refinement, resulting in smaller grain sizes. The inverse pole figure (IPF) maps in Figure 5.7 (b) and (e) revealed the crystallographic orientation of the grains, where similar shades of color indicated similar orientations [67,103]. The needle-like AFs are distributed throughout the weld metal, exhibiting various crystal orientations.

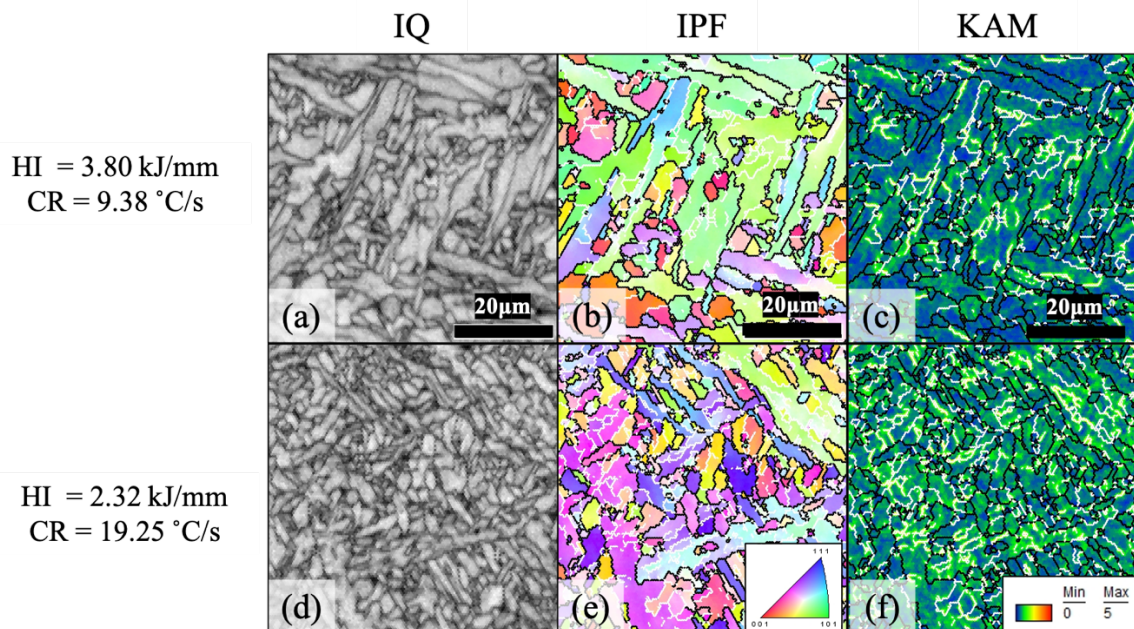


Fig. 5.7 Comparison of EBSD results: (a) and (d) IQ maps; (b) and (e) IPF maps; (c) and (f) KAM maps; from conventional and hot-wire GMAW respectively.

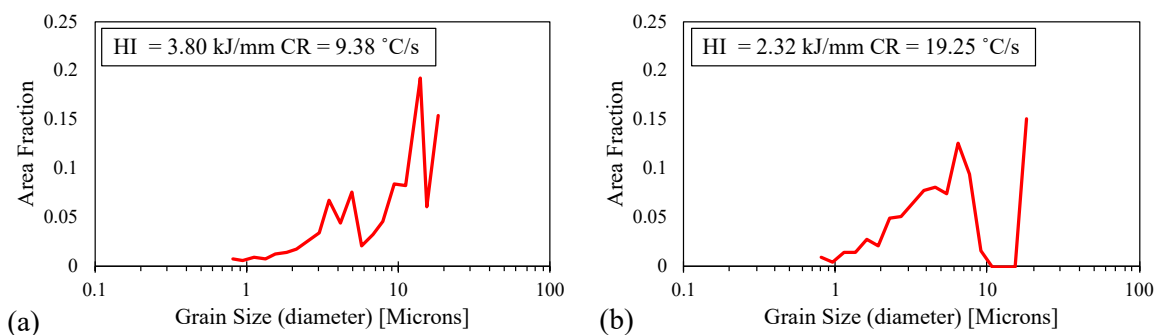


Fig. 5.8 Grain size fraction distribution: (a) Conventional GMAW; (b) Hot-wire GMAW

The KAM maps in Figure 5.7 (c) and (f) reveal that needle-like AFs, more prevalent in weld metal produced from hot-wire GMAW, exhibit higher KAM values compared to other regions. These higher KAM values indicate a greater dislocation density, enhancing resistance to deformation and crack propagation, resulting in improved mechanical properties [108, 109, 112]. Figure 5.8 demonstrates the distribution of grain size fractions, showing an increase in the smaller grain sizes fractions when utilizing hot-wire GMAW. The results align with the assumption made earlier. Additionally, the CCT diagram for low-carbon steel weld metal in Figure 2.12 indicates that faster cooling speeds lead to smaller grain sizes [7, 69, 71]. To validate these findings, it is essential to conduct mechanical testing, such as Vickers hardness and Charpy impact tests, based on the results from optical microscopy (OM) and EBSD analysis.

Figure 5.9 presents the plots of Vickers hardness and Charpy impact toughness values of the weld metal. The transition from conventional GMAW to hot-wire GMAW leads to a gradual increase in both hardness and impact toughness. Specifically, the hardness values rise from 180 ± 3 to 193 ± 7 HV10, and the impact toughness values increase from 55 ± 10 to 80 ± 13 J. These improvements in mechanical properties align with the changes observed in the microstructure from OM and EBSD. By reducing the heat input while maintaining the same deposition rate, the weld metal exhibits a higher fraction of AF and SPF. This increase in AF and SPF contributes to enhanced resistance against crack propagation and increased toughness [108, 110, 111].

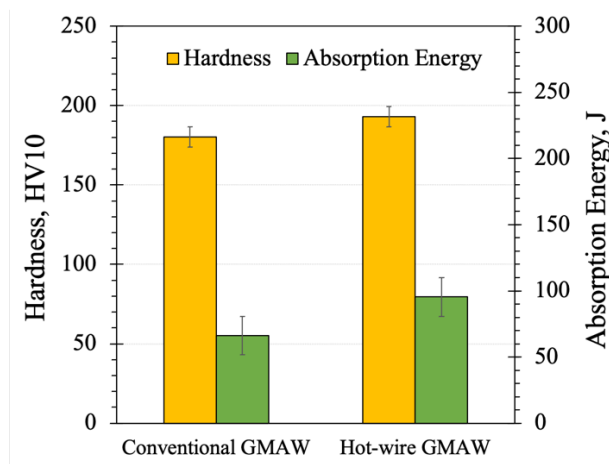


Fig. 5.9 Vickers hardness and Charpy impact toughness values in weld metal

Figure 5.10 presents schematic diagrams illustrating the microstructure evolution in the weld metal during different welding processes. The author utilizes a CCT diagram of low-carbon and low-alloyed steel [71] to explain the influence of cooling rate changes. In the conventional GMAW process, the slow cooling rate results in the predominant growth of GBF from columnar austenite grain boundaries, takeover space and affecting the formation of other structures. As the temperature further decreases, a smaller amount of needle-like AF is randomly formed within the

space surrounded by SPF and blocky GBF, as shown in Figure 5.10 (a). However, with an increased cooling rate due to hot-wire application, the proportion of GBF decreases because lower driving force to mobilize in planar growth, allowing for the growth of SPF. Needle-like AFs are then randomly formed and distributed within the grains, as depicted in Figure 5.10 (b).

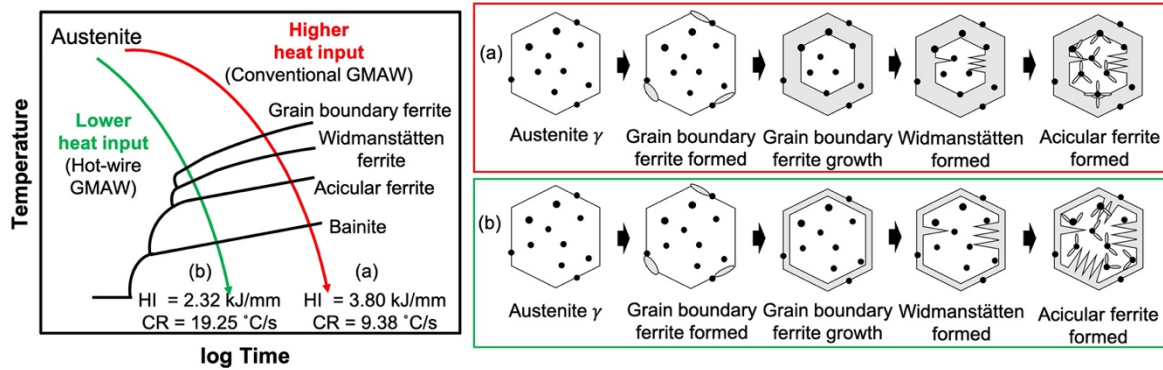


Fig. 5.10 Microstructure evolution under different welding process

5.4 Effect of Ni content from hot-wire insertion on welded specimens

5.4.1 Bead appearance and weld geometry

The impact of nickel (Ni) content in hot-wire GMAW on the appearance and weld geometry of the welded specimens was investigated in this section. Figure 5.11 presents macro cross-sectional images of the samples with different Ni content: sample HW-1 (0.00%wt Ni), sample HW-2 (0.98%wt Ni), and sample HW-3 (2.87%wt Ni). All samples exhibit sound weld conditions. Additionally, Figure 5.11(d) provides the measured weld geometry for the varying Ni content, indicating the consistent deposited volume of the molten pool across the three conditions.

5.4.2 Cooling profile and obtained weld metal structure

The weld metals exhibit complex microstructures with variations in grain size dispersion due to different cooling profiles and chemical composition, resulting in distinct phase volume fractions. The cooling rates from 800 to 500 °C of HW-1 (0.00wt% Ni), HW-2 (0.98wt% Ni), and HW-3 (2.87wt% Ni) are measured as 19.25, 17.98, and 14.58 °C/s, respectively. The microstructure of all three weld metals primarily comprises acicular ferrite (AF) and ferrite side plate (FSP), with minimal grain boundary ferrite (GBF) fractions. Figure 5.12(a) presents fine AFs within grains while mixed coarse grains of FSP and GBF, with widths above 10 μm, grow inward. Although there is a slight change in Ni content, the variation in microstructure within the weld metal remains noticeable. The fractions of FSPs and GBFs decrease with increasing Ni content, particularly in sample HW-3, which possesses the highest Ni content compared to samples HW-2 and HW-1.

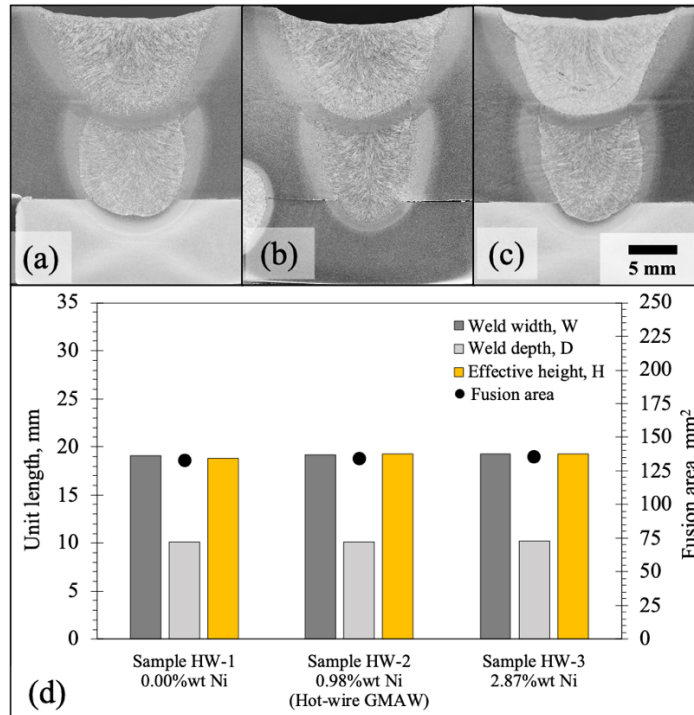


Fig. 5.11 Measured weld profiles geometry

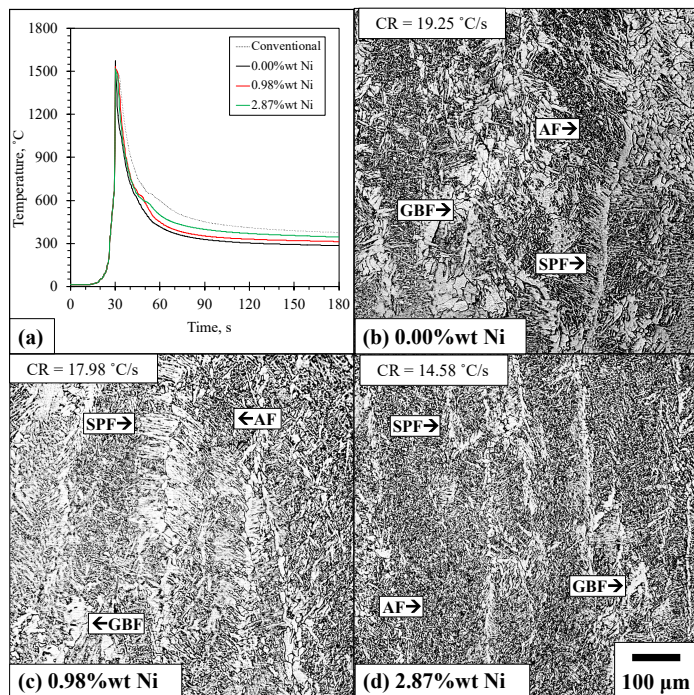


Fig. 5.12 Cooling profile and obtained microstructure: (a) cooling profile (b) WM-1; (c) WM-2; (d) WM-3.

The higher Ni content in sample HW-3 significantly suppresses the formation of GBFs and SPFs because of the decrease in the austenite-to-ferrite transformation temperature [89-92]. GBF has a detrimental effect on weld metal properties, particularly toughness, as its coarse grain structure facilitates crack propagation [69-71]. Quantitative analysis of the weld metal microstructure in Figure 5.13 (a) confirms

that increasing the Ni content decrease in the volume fraction of GBFs and SPFs, while the amount of acicular ferrite (AF) increases. Sample HW-3 exhibits a remarkable AF volume fraction of up to 75%, surpassing that of sample HW-2 (53%) and HW-1 (42%). The higher Ni content in the hot-wire filler metal results in a slower cooling rate and a reduced presence of GBFs, as observed. Figure 5.13 (b) shows the average prior austenite grain sizes regarding the Ni content raised. Kou. [7] explained that larger prior austenite grain sizes induces the phase transformation of the WM to predominantly AF.

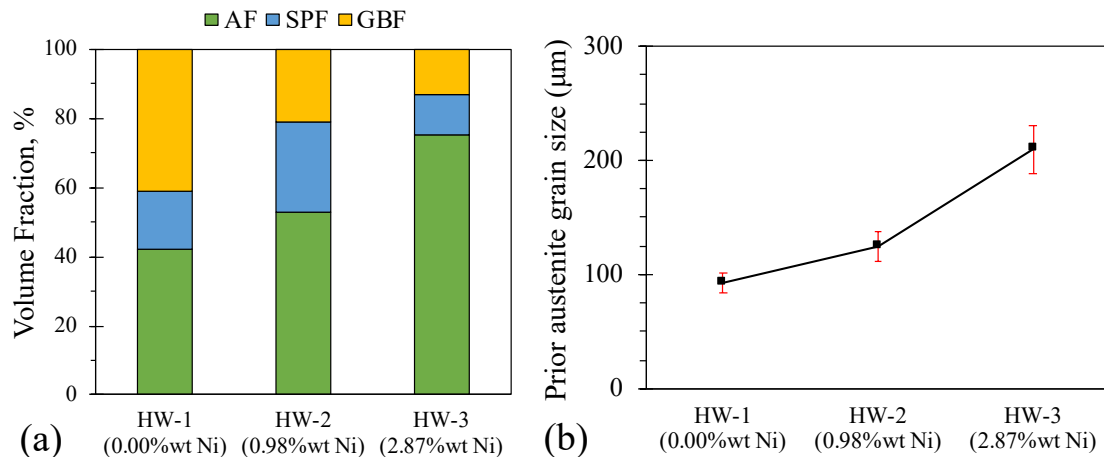


Fig. 5.13 Volume fraction of weld metals

Figures 5.14 (a), (d), and (e) provide image quality maps obtained through EBSD analysis, showing a decrease in the fractions of GBF and SPF with increasing nickel content, aligning with the qualitative volume fraction results. The observation areas reveal that the total grain boundary length of HW-1, HW-2, and HW-3 are 1.26 cm, 1.37 cm, and 191 cm, respectively, indicating a decrease in average grain size and improved mechanical properties as Ni content increases. Figures 5.14 (b), (e), and (h) present IPF maps, illustrating the more complex crystallographic orientation of AF with higher Ni content. The KAM images in Figure 5.14 (c), (f), and (g) demonstrate that AF regions exhibit higher KAM values and a greater number of sub-grain boundaries compared to other regions, indicating improved mechanical properties associated with Ni content. Figure 5.15 shows the distribution of grain size fractions, revealing a trend towards smaller grain sizes as Ni content increases. The misorientation angle distribution in Figure 5.16 can distinguish between different structure morphologies. Gourgues et al. [101] proposed that AF provided a significant proportion of high-angle grain boundaries at 50° and 60° with minimal misorientation angle from 25° to 45° . Jorge et al. [94] reported that the misorientation angle from 25° to 45° raised due to the presence of polygonal ferrite. Consequently, the decrease in misorientation angles between 25° and 45° with increasing Ni content can be attributed to the dominance of AF in the weld metal.

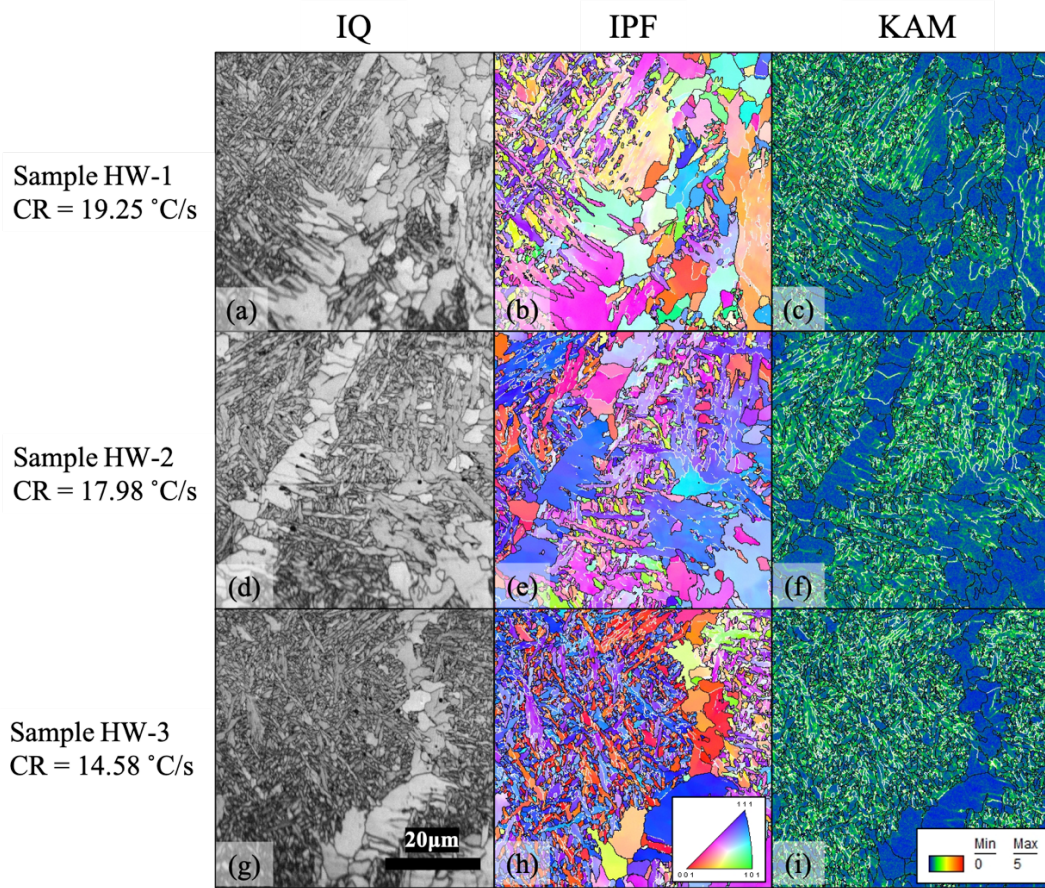


Fig. 5.14 Comparison of SEM, EBSD and KAM results produced from:
 (a) 0.00%wt Ni; (b) 0.98%wt Ni; (c) 2.87%wt Ni

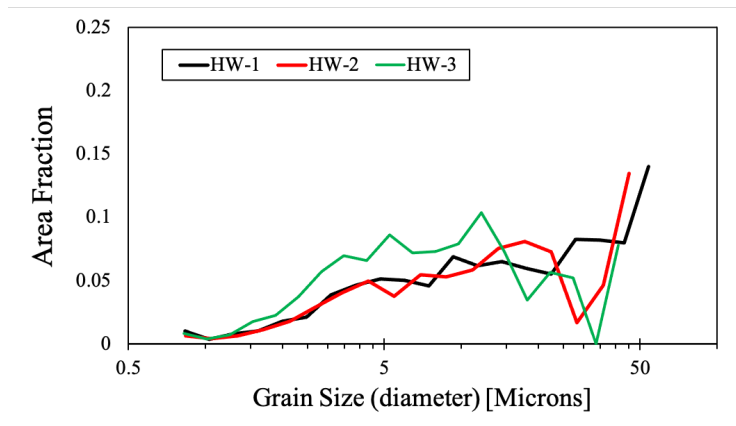


Fig. 5.15 Schematic diagrams describing the effect of the cooling rate.

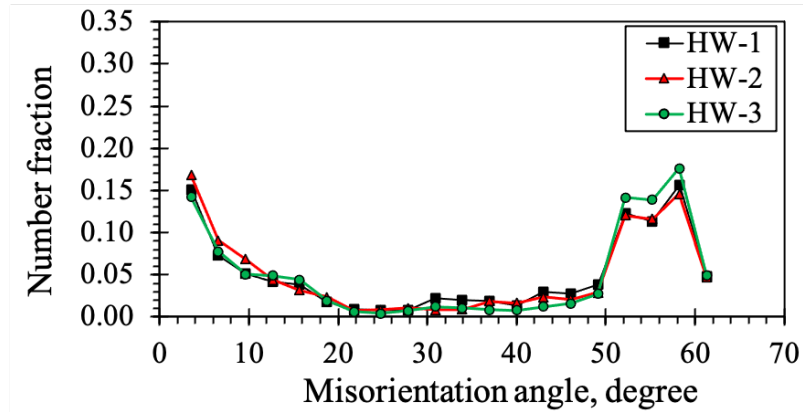


Fig. 5.16 Schematic diagrams describing the effect of the cooling rate.

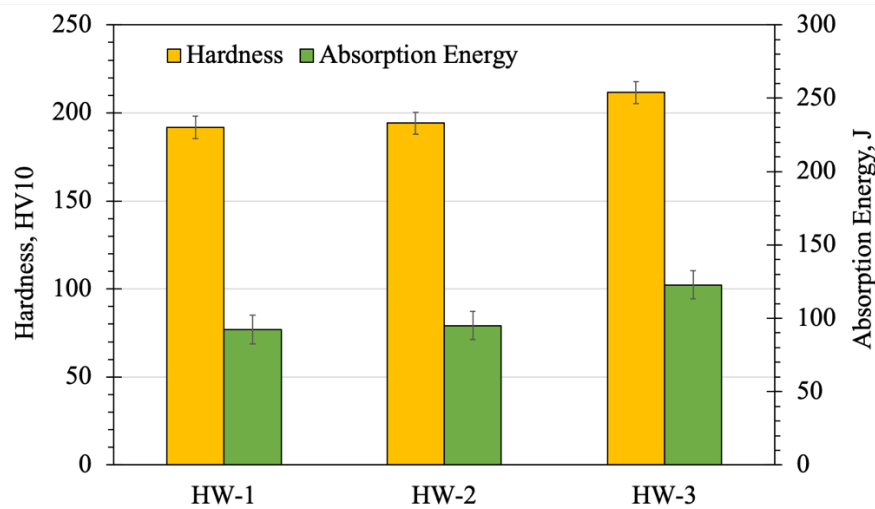


Fig. 5.17 Schematic diagrams describing the effect of the cooling rate.

The mechanical properties of the samples with incremental Ni content are presented in Figure 5.17. The results indicate that absorption energy and hardness were influenced by the obtained microstructures. Sample HW-3 exhibited significantly better performance than sample HW-2 and HW-1, clearly demonstrating the benefits of additional Ni using hot-wire insertion. The average hardness value raises from 193 ± 7 to 195 ± 7 HV10, and 211 ± 5 HV10 and the average of impact toughness values increase from 80 ± 13 J to 83 ± 11 J, and 120 ± 5 J from sample HW-1, HW-2, and HW-3, respectively. These improvement in mechanical properties align with the changes observed in the microstructure from OM and EBSD. By increasing the Ni content while maintaining the same deposition rate, the weld metal exhibits a higher fraction of AF. Considering the outstanding mechanical properties across different Ni content and the primary microstructures of AF, FSP, and GBF, we can expect no notable changes in these fractures, which are likely to be primarily ductile fractures.

To determine the impact of nickel addition on the phase transformation temperature, the AC1 and AC3 temperatures, which signify the points of phase transformation from austenite to ferrite, were calculated using Andrew's equations [90-91]. The results, depicted in Figure 5.18 (a), demonstrate that increasing Ni content reduces the transformation temperature. Kou [7] explained that alloying elements shift the CCT curves towards longer times and lower temperatures, influencing the phase transformation of the weld metal from predominantly GBF and SPF to predominantly AF. Additionally, Mohrbacher et al. [89] provided strong evidence supporting the shift in the CCT diagram with increased Ni content. Figure 5.18 (b) presents schematic diagrams illustrating the microstructure evolution during post solidification, with reference to the CCT diagram of low-carbon and low-alloyed steel [7,78,89] to elucidate the effect of Ni content. The combination between a faster cooling rate and larger prior austenite grain sizes contribute to an increased fraction of randomly interlocking distributed AF in the weld metal.

However, other studies discuss different AF formation mechanisms. During phase transformation, AFs nucleate heterogeneously on non-intermetallic inclusions [69,79,80]. The preference for intragranular nucleation increases with a larger austenite grain size or a higher number of inclusions [69,75,76]. By reducing the number of inclusions, the nucleation sites for AF decreased [78-81]. Therefore, the variation in AF fractions might get affected by these mechanisms. Further investigation, including austenite grain size, inclusion size, and their distribution in AF regions, is necessary to gain deeper insights into the impact of increasing nickel content using hot-wire insertion.

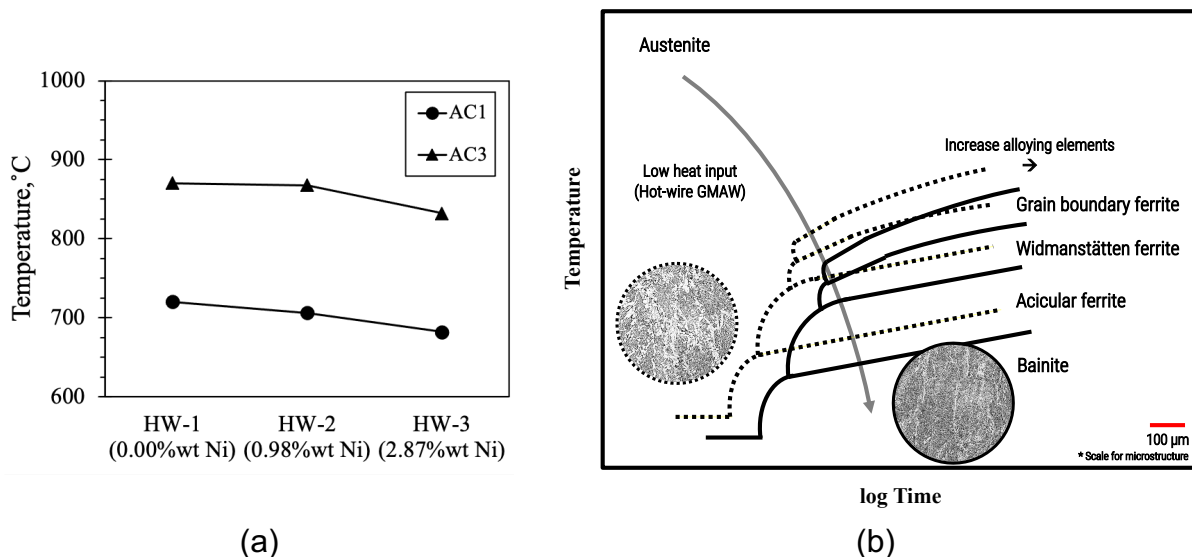


Fig. 5.18 Schematic diagrams describing the effect of the cooling rate.

5.5 Conclusion

In this study, hot-wire GMAW was used to successfully produce a soundness weld metal with similar deposition rate as conventional GMAW but achieved better joint properties. Moreover, this study also demonstrates the potential adjusting Ni content in weld metals using hot-wire insertion as a means to optimize their microstructure and enhance mechanical properties, particularly hardness and impact toughness. The conclusions were drawn as follows:

(1) Hot-wire GMAW provided a lower heat input process resulting in faster cooling rate which led to finer grain and reduced the GBF fraction at similar deposition rate while maintaining the effective height of the joint.

(2) The addition of Ni has a positive effect on phase transformation, stabilizing the austenite grain and reducing the austenite-to-ferrite transformation temperature which can promote the formation of AF.

(3) The higher Ni content also reducing the presence of SPF and GBF which is detrimental to strength, hardness, and impact toughness, is effectively suppressed with higher Ni content, while AF, known for its positive impact on these properties, becomes the dominant microstructure.

(4) The results indicate that Ni content plays a crucial role in determining the microstructure and mechanical properties of the weld metal, highlighting the importance of Ni addition through hot-wire insertion for achieving superior weld performance.

(5) Further investigation such as the effect of austenite grain size, inclusion size and distribution in AF regions will give more insight of the impact on increasing Ni using hot-wire insertion.

Chapter 6

Summary and Future plan

6.1 Summary

The hot-wire GMAW process offers exceptional deposition volume without excessive power consumption, reducing the number of weld passes required and increasing process tolerance. In light of these benefits, three main objectives were highlighted and presented with outstanding results as follows:

Firstly, the aim of chapter 3 was to develop a single-pass welding method using hot-wire GMAW on 15-mm thick steel plate square butt joints without edge preparation. In this chapter, the small process tolerance of GMAW was exposed with the remedy. Hot-wire insertion is not only increase the process tolerance by independent additional deposition volume while not required more power consumption but its ability to create a single pass welding for a square butt joint of 15-mm thick steel plate without edge preparation was highlighted. Effect of hot-wire fraction and travel speed on cooling behavior revealed that hot-wire fraction decreased the cooling rate and more grain boundary ferrite could be obtained. However, within 43.18% of hot-wire fraction provided non-significant effect to the weld metal properties. In conclusion for this chapter, a new approach of single-pass welding was successfully developed, at 60 cm/min of welding speed, 62% less power consumption could be achieved but provided similar deposition volume as submerged arc welding.

Secondly, the aim of chapter 4 was to conduct a systematic study on hot-wire insertion to determine the impact of hot-wire fraction and maximum deposition efficiency during GMAW. The study employed a high-speed camera to monitor the welding process, which detected the molten metal precedence leading to lack of fusion. Cooling profiles were analysed alongside the obtained microstructure. Three stages of experiment were conducted and show the following results: In the first stage, the compensatory condition was successfully achieved, where hot-wire was used to increase deposition rate while minimizing GMAW fraction and compare to the similar deposition rate using only conventional GMAW. The second stage determined the maximum hot-wire fraction that could be used without causing welding defects or detrimental effects on weld metal properties, 44.05% was the limitation of hot-wire fraction in total deposition rate. In the third stage, the fraction of hot-wire and GMAW was optimized at the highest deposition rate to achieve a sound joint condition with the lowest energy consumption. The optimized condition between GMAW and HW fraction provided a soundness joint with improved mechanical properties using a 250.72 g/min with a 41.16%HW and 62% less power consumption compared with conventional GMAW.

Chapter 5 aimed to enhance joint properties in GMAW by using selective hot-wire filler metal. Increasing the nickel (Ni) content through hot-wire insertion, resulting in sound weld metal with improved mechanical properties. The advantages

of hot-wire GMAW, including lower heat input and faster cooling rate, contributed to the grain refinement and reduction of grain boundary ferrite (GBF) fraction. Additionally, the added Ni suppresses the fractions of side plate ferrite (SPF) and GBF and promotes the formation of acicular ferrite (AF). Weld metals produced with 2.87%wt Ni wire exhibited a predominance of AF, improving impact toughness and hardness. These findings have significant implications for advancing hot-wire GMAW technology and its practical applications in welding. However, further investigations focusing on austenite grain size, inclusion size, and their distribution in AF regions will provide valuable insights into the influence of increasing Ni content through hot-wire insertion.

In conclusion, hot-wire technology showed outstanding efficiency in combination with GMAW. Hot-wire GMAW enables the deposition rate over submerged arc welding while consuming 62% less power consumption. The author proposed the hot-wire fraction limitation on the processing and metallurgical side. Excessive hot-wire fraction led to molten metal precedence and provided large GBF and SPF fractions, resulting in the degradation of weld metal. Nickel addition as hot-wire filler metal provided better hardness and toughness of weld metal due to acicular ferrite enrichment. Therefore, hot-wire insertion enlarges the GMAW process tolerance in a sustainable way of development.

6.2 Future plan

Recently, the author investigated the weld metal produced using YGT9Ni-2 and MGS308 as hot-wire insertion to clarify the impact of Ni content on weld metal properties. The first observation revealed the dissimilar interlayer weld metal with stainless steel characteristics. Moreover, the obtained grain refinement regions need further investigation.

In nearly future, increasing Ni content to enhance weld metal properties using hot-wire insertion have to investigate the impact of austenite grain size, size, and distribution of non-metallic inclusion. To identify and characterize the AF formation during hot-wire GMAW. Additionally, the optimization of process parameter to achieve higher production speed while minimizing power consumption enable sustainable development. In the far future, a deep understanding of solidification and phase transformation will insight into and enable the hot-wire GMAW of other materials such as stainless steel and aluminum.

Acknowledgements

I express my deep gratitude to my parents, Chatree and Sommana (Wanna) Suwannatee, whose unwavering strength (financially), unwavering encouragement (emotionally), and unwavering inspiration (humorously) have been instrumental in shaping my life and academic journey. Special thanks for my all-rounder support, my commander, my everything, Squadron Leader Phanintra Soonthornharuethai.

I extend my heartfelt appreciation to my advisor, Professor Motomichi Yamamoto, whose exceptional guidance and motivation have been instrumental in my academic success. I am also grateful to Professor Kenji Shinozaki for his invaluable comments and guidance.

I would like to thank Mr. Shinichiro Shinohara from Tsuneishi Shipbuilding Co., Ltd. for his support in providing materials and specimens throughout my research. My heartfelt thanks to all current and former members of the Setsugo Laboratory for their support. Specifically, Mr. Kimura Hayato, Mr. Ozeki Yuma, and Mr. Marumoto Keita.

I am grateful to Asst. Prof. Rittichai Phaoniam, Asst. Prof. Pariyasuit Wattanatham, Asst. Prof. Sittipong Sang-in, Assoc. Prof. Bovornchok Poopat, Professor Asa Pratepasen, Professor Hatung Fritz, Professor Lothar Kroll and my favorite life professor Harald Pfeffer for giving me the opportunity to pursue my research.

I would like to express my respect and gratitude to my exceptional research assistants, Mr. Kanon Nakamura, Mr. Adhitya Nathella Baskar, and Mr. Jukkaphan Greebmalai, whose support and assistance have been indispensable to the completion of this Neo Armstrong Cyclone Jet Armstrong thesis. I am honored to have them as part of my research team and acknowledge that their contributions to my work have been invaluable.

Last but not least, I would like to express my sincerest gratitude to Professor Jeong-Won Choi. As my mentor, colleague, and now my big brother by choice, I am fortunate to have his unwavering commitment and friendship in my life. I am deeply grateful for his unwavering support and the profound impact he has had on my personal and professional growth.

References

- 1) Imai, S. Recent progress and future trends for shipbuilding steel, *Welding International*, (2008) 22(11):755-761. <https://doi.org/10.1080/09507110802550661>
- 2) Liu, D., Li, Q., Emi, T. Microstructure and mechanical properties in hot-rolled extra high-yield-strength steel plates for offshore structure and shipbuilding, *Metallurgical and materials transactions A*, (2011) 42(5):1349-1361. <https://doi.org/10.1007/s11661-010-0458-1>
- 3) Nishioka, K., Kazutoshi I. Progress in thermomechanical control of steel plates and their commercialization, *Science and Technology of Advanced Materials*, (2012) 13(2):023001. <https://doi.org/10.1088/1468-6996/13/2/023001>
- 4) Nemani, A. V., Ghaffari, M., Nasiri, A. Comparison of microstructural characteristics and mechanical properties of shipbuilding steel plates fabricated by conventional rolling versus wire arc additive manufacturing, *Additive Manufacturing*, (2020), 32:101086. <https://doi.org/10.1016/j.addma.2020.101086>.
- 5) Vukelic, G., Vizentin, G., Brnic, J., Brcic, M., Sedmak, F. Long-Term Marine Environment Exposure Effect on Butt-Welded Shipbuilding Steel, *Journal of Marine Science and Engineering*, (2021) 9:491. <https://doi.org/10.3390/jmse9050491>.
- 6) Holliday, D.B.; Dull, R.M.; Hartman, D.K.; Wright, D.A. Chapter 4—Gas Metal Arc Welding. In *Welding Handbook*, 9th ed.; O'Brien, A., Ed.; American Welding Society: Miami, FL, USA, (2004), Volume 2, pp. 148–197.
- 7) Kou, S. *Welding metallurgy*. 2nd edition, John Wiley & Sons, Inc.: Hoboken, New Jersey, USA (2003).
- 8) James F. Lincoln Arc Welding Foundation. *The procedure handbook of arc welding*. 12th edition, The Lincoln Electric Company, Cleveland, Ohio (2000).
- 9) Lippold, John C., Damian J. Kotecki. *Welding metallurgy and weldability of stainless steels*. , John Wiley & Sons, Inc.: Hoboken, New Jersey, USA (2005).
- 10) Sun, L., Li, H., Zhu, L., Liu, Y., Hwang, J. Research on the evolution mechanism of pinned particles in welding HAZ of Mg treated shipbuilding

steel, *Materials & Design*, (2020) 192:108670.
<https://doi.org/10.1016/j.matdes.2020.108670>

- 11) Li, B., Liu, Q., Jia, S., Ren, Y., Yang, P. Effect of V Content and Heat Input on HAZ Softening of Deep-Sea Pipeline Steel, *Materials* (2022) 15(3):794.
<https://doi.org/10.3390/ma15030794>
- 12) Goldak, J., Bibby, M., Moore, J., House, R., Patel, B. Computer modeling of heat flow in welds, *Metallurgical transactions B*, (1986) 17: 587-600.
<https://doi.org/10.1007/BF02670226>
- 13) Teng, T. L., Chang, P. H., Tseng, W. C. Effect of welding sequences on residual stresses. *Computers & structures*, (2003) 81(5): 273-286.
[https://doi.org/10.1016/S0045-7949\(02\)00447-9](https://doi.org/10.1016/S0045-7949(02)00447-9)
- 14) Colegrove, P., Ikeagu, C., Thistlethwaite, A., Williams, S., Nagy, T., Suder, W., Pirling, T. Welding process impact on residual stress and distortion, *Science and Technology of Welding and Joining*, (2009) 14(8): 717-725.
<https://doi.org/10.1179/136217109X406938>
- 15) Liu, G., Han, S., Tang, X., Cui, H. Effects of torch configuration on arc interaction behaviors and weld defect formation mechanism in tandem pulsed GMAW, *Journal of Manufacturing Processes*, (2021) 62:729-742.
<https://doi.org/10.1016/j.jmapro.2021.01.007>
- 16) Hammad, A., Churiaque, C., Sánchez-Amaya, J. M., Abdel-Nasser, Y. Experimental and numerical investigation of hybrid laser arc welding process and the influence of welding sequence on the manufacture of stiffened flat panels, *Journal of Manufacturing Processes*, (2021) 61:527-538.
<https://doi.org/10.1016/j.jmapro.2020.11.040>
- 17) Elmesalamy, A., Francis, J. A., Li, L. A comparison of residual stresses in multi pass narrow gap laser welds and gas-tungsten arc welds in AISI 316L stainless steel, *International Journal of Pressure Vessels and Piping*, (2014) 113:49-59. <https://doi.org/10.1016/j.ijpvp.2013.11.002>
- 18) Cui, H. C., Jiang, Z. D., Tang, X. H., Lu, F. G. Research on narrow-gap GMAW with swing arc system in horizontal position, *The International Journal of Advanced Manufacturing Technology*, (2014) 74: 297-305.
<https://doi.org/10.1007/s00170-014-5984-3>
- 19) Liu, G., Tang, X., Han, S., Cui, H. Influence of interwire distance and arc length on welding process and defect formation mechanism in double-wire

- pulsed narrow-gap gas metal arc welding, *Journal of Materials Engineering and Performance*, (2021) 30(10): 7622-7635. <https://doi.org/10.1007/s11665-021-05888-w>
- 20) Masmoudi, F., Bouaziz, Z., Hachicha, W. Computer-aided cost estimation of weld operations, *The International Journal of Advanced Manufacturing Technology* (2007) 33(3-4): 298-307. <https://doi.org/10.1007/s00170-006-0463-0>
 - 21) Chayoukhi, S., Bouaziz, Z., Zghal, A. Cost estimation of joints preparation for GMAW welding process using feature model, *Journal of materials processing technology*, (2008) 199.1-3: 402-411. <https://doi.org/10.1016/j.jmatprotec.2007.08.024>
 - 22) Phaoniam, R., Shinozaki, K., Yamamoto, M., Kadoi, K., Nishijima, A., & Yamamoto, M. Solidification cracking susceptibility of modified 9Cr1Mo steel weld metal during hot-wire laser welding with a narrow gap groove, *Welding in the World*, (2014) 58:469-476. <https://doi.org/10.1007/s40194-014-0130-2>
 - 23) Dak, G., Khanna, N., & Pandey, C. Study on narrow gap welding of martensitic grade P92 and austenitic grade AISI 304L SS steel for ultra-supercritical power plant application, *Archives of Civil and Mechanical Engineering*, (2022) 23(1):14. <https://doi.org/10.1007/s43452-022-00540-3>
 - 24) Yu, J., Cai, C., Xie, J., Huang, J., Liu, Y., & Chen, H. Weld formation, arc behavior, and droplet transfer in narrow-gap laser-arc hybrid welding of titanium alloy, *Journal of Manufacturing Processes*, (2023) 91:44-52. <https://doi.org/10.1016/j.jmapro.2023.02.022>
 - 25) Shinozaki, K., Yamamoto, M., Mitsuhata, K., Nagashima, T., Kanazawa, T., Arashin. H. Bead formation and wire temperature distribution during ultra-high-speed GTA welding using pulse-heated hot-wire, *Welding in the World*, (2011) 55:12-18. <https://doi.org/10.1007/BF03321281>
 - 26) Cicero M. D. Starling, Paulo V. Marques, Modenesi J. P. Statistical modeling of narrow-gap GTA welding with magnetic arc oscillation, *J. Materials Processing Technology*, (1995) 51:37-49. [https://doi.org/10.1016/0924-0136\(94\)01356-6](https://doi.org/10.1016/0924-0136(94)01356-6)
 - 27) Shinoda, T., Hoshino, K., Yamashita, R., Ono, H. Development of solidification cracking test for MAG narrow gap welding - Effect of boron

contents on solidification cracking, Quarterly Journal of the Japan Welding Society, (1990) 8(1):21-25. <https://doi.org/10.2207/qjwjs.8.21>

- 28) Tsushima, S., Horii, Y., Yurioka, N. Development of AC-MIG welding process (Report 5). Application of AC-MIG narrow gap welding process for butt joints of 980MPa high strength steels, Quarterly Journal of the Japan Welding Society (1994) 12(1):51-57. <https://doi.org/10.1080/09507119409548641>
- 29) Bao, Y., Xue, R., Zhou, J., Liu, H., Xu, Y. The Influence of Oscillation Parameters on the Formation of Overhead Welding Seams in the Narrow-Gap GMAW Process, Applied Sciences, (2023) 13(9):5519. <https://doi.org/10.3390/app13095519>
- 30) Wang, J., Jiang, Y., Zhu, J., Liu, D., Xu, G., Li, W. Development of swing arc narrow gap GMAW process assisted by swaying wire, Journal of Materials Processing Technology, (2023) 118004. <https://doi.org/10.1016/j.jmatprotec.2023.118004>
- 31) Yang, Z., Chen, Y., Zhang, Z., Fang, C., Xu, K., He, P., Zhang, Z. Research on the sidewall penetration mechanisms of cable-type welding wire narrow gap GMAW process, The International Journal of Advanced Manufacturing Technology, (2022) 120(3-4):2443-2455. <https://doi.org/10.1007/s00170-022-08866-1>
- 32) Ni, Z., Hu, F., Li, Y., Lin, S., Cai, X. Microstructure and Mechanical Properties of the Ternary Gas Shielded Narrow-Gap GMA Welded Joint of High-Strength Steel, Crystals, (2022) 12(11):1566. <https://doi.org/10.3390/cryst12111566>
- 33) Persson M. Fully automation welding of thick walled pressure vessel by the narrow gap subarc welding process, Journal of Materials and Design, (1985) 6(5):244-247. [https://doi.org/10.1016/0261-3069\(85\)90107-4](https://doi.org/10.1016/0261-3069(85)90107-4)
- 34) Wu, Y., Yuan, X., Kaldre, I., Zhong, M., Wang, Z., Wang, C. TiO₂-assisted microstructural variations in the weld metal of EH36 shipbuilding steel subject to high heat input submerged arc welding, Metallurgical and Materials Transactions B, (2023) 54(1):50-55. <https://doi.org/10.1007/s11663-022-02697-x>
- 35) Abe, Y., Fujimoto, T., Nakatani, M., Shigeta, M., Tanaka, M. Development of a welding condition optimization program for narrow gap SAW, Quarterly Journal of the Japan Welding Society, (2020) 38(2):98s-102s. <https://doi.org/10.2207/qjwjs.38.98s>

- 36) Coetsee, T., De Bruin, F. J. Improved Titanium Transfer in Submerged Arc Welding of Carbon Steel through Aluminum Addition, *Mineral Processing and Extractive Metallurgy Review*, (2022) 43(6):771-774. <https://doi.org/10.1080/08827508.2021.1945595>
- 37) Tsuyama, T., Yuda, M., Nakai, K. Effects of hot wire on mechanical properties of weld metal using gas-shielded arc welding with CO₂ gas, *Welding in the World*, (2014) 58:77-83. <https://doi.org/10.1007/s40194-013-0094-7>
- 38) Wonthaisong, S., Shinohara, S., Shinozaki, K., Phaoniam, R., Yamamoto, M. Evaluation of Butt Joint Produced by a Hot-Wire CO₂ Arc Welding Method, *Quarterly Journal of the Japan Welding Society*, (2021) 39(1):96-103. <https://doi.org/10.2207/qjjws.39.96>
- 39) Wonthaisong, S., Development of hot-wire welding process for butt joint of thick steel plate, Doctoral Dissertation, Hiroshima University, (2021).
- 40) Wonthaisong, S., Shinohara, S., Shinozaki, K., Phaoniam, R., Yamamoto, M. High-Efficiency and Low-Heat-Input CO₂ Arc-Welding Technology for Butt Joint of Thick Steel Plate Using Hot Wire, *Quarterly Journal of The Japan Welding Society*, (2020) 38(3):164-170. <https://doi.org/10.2207/qjjws.38.164>
- 41) Tsuyama, T., Nakai, K., Noumaru, K., Sakamoto, T., Kobayashi, S. Effect of hot-wire on microstructure and mechanical property in weld metal formed with CO₂ gas shielded arc welding method, *Welding International*, (2015) 29(6):409-416. <https://doi.org/10.1080/09507116.2014.921065>
- 42) Devaney, R. J., O'Donoghue, P. E., Leen, S. B. Effect of welding on microstructure and mechanical response of X100Q bainitic steel through nanoindentation, tensile, cyclic plasticity and fatigue characterisation, *Materials Science and Engineering: A*, (2021) 804:140728. <https://doi.org/10.1016/j.msea.2020.140728>
- 43) Song, S., Dong, P., Zhang, J. A full-field residual stress profile estimation scheme for pipe girth welds. In *Pressure Vessels and Piping Conference*, 2012, July Vol. 55089, pp.109-120. American Society of Mechanical Engineers. <https://doi.org/10.1115/PVP2012-78560>
- 44) Kartal, M. E., Kang, Y. H., Korsunsky, A. M., Cocks, A. C. F., Bouchard, J. P. The influence of welding procedure and plate geometry on residual stresses in thick components, *International Journal of Solids and Structures*, (2016) 80: 420-429. <https://doi.org/10.1016/j.ijsolstr.2015.10.001>

- 45) Tsuyama, T., Nakai, K. Tsuji, T. Development of submerged arc welding method using hot wire. *Welding in the World*, (2014) 58:713–718 <https://doi.org/10.1007/s40194-014-0153-8>
- 46) El-Batahgy, Abdel-Monem. Laser beam welding of austenitic stainless steels– Similar butt and dissimilar lap joints, *Welding Process*, (2012) :93-116. <http://dx.doi.org/10.5772/48756>
- 47) Feng, J., Guo, W., Francis, J., Irvine, N., Li, L. Narrow gap laser welding for potential nuclear pressure vessel manufacture, *Journal of Laser Applications*, (2016) 28(2):022421. <https://doi.org/10.2351/1.4943905>
- 48) Grünenwald, S., Seefeld, T., Vollertsen, F., Kocak, M. Solutions for joining pipe steels using laser-GMA-hybrid welding processes, *Physics Procedia*, (2010) 5:77-87. <https://doi.org/10.1016/j.phpro.2010.08.032>
- 49) Tóth, T., Krasnorutskyi, S., Hensel, J., Dilger, K. Electron beam welding of 2205 duplex stainless steel using pre-placed nickel-based filler material, *International Journal of Pressure Vessels and Piping*, (2021) 191:104354. <https://doi.org/10.1016/j.ijpvp.2021.104354>
- 50) Elmer, J.W., Vaja, J., Gibbs, G. Reduced pressure laser weld comparison to electron beam welds in Ti-6Al-4 V, *Welding in the World*, (2022) 66:2053–2071. <https://doi.org/10.1007/s40194-022-01356-8>
- 51) Balakrishnan, J., Vasileiou, A. N., Francis, J. A., Smith, M. C., Roy, M. J., Callaghan, M. D., Irvine, N. M. Residual stress distributions in arc, laser and electron-beam welds in 30 mm thick SA508 steel: a cross-process comparison, *International Journal of Pressure Vessels and Piping*, (2018) 162: 59-70. <https://doi.org/10.1016/j.ijpvp.2018.03.004>
- 52) Zhu, S., Nakahara, Y., Yamamoto, M., Shinozaki, K., Aono, H., Ejima, R. Additive manufacturing phenomena of various wires using a hot-wire and diode laser, *Welding in the World*, (2022) 66(7):1315-1327. <https://doi.org/10.1007/s40194-022-01273-w>
- 53) H. baba, T. Era, T. Ueyama, M. Tanaka: Single pass full penetration joining for heavy plate steel using high current GMA process, *Welding in the World*, (2017) 61:963-969. <https://doi.org/10.1007/s40194-017-0464-7>
- 54) Kadoi, K., Shinozaki, K., Yamamoto, M., Owaki, K., Inose, K., Takayanagi, D. Development of high-efficiency/high-quality hot-wire laser fillet welding

- process, Quarterly Journal of the Japan Welding Society, (2011) 29(3):62s-65s. <https://doi.org/10.2207/qjws.29.62s>
- 55) Kim, J. Y., Lee, J., Lee, S. H. Effect of reverse-polarity hot wire on the tandem arc welding process, Engineering Science and Technology, an International Journal, (2022) 36:101168. <https://doi.org/10.1016/j.jestch.2022.101168>
- 56) Marumoto, K., Tamata, H., Fujinaga, A., Takahashi, T., Yamamoto, H., Choi, J., Yamamoto, M. Bead shape control in high-speed fillet welding using hot-wire GMA laser hybrid welding technology, Welding in the World, (2023) 67(5):1259-1266. <https://doi.org/10.1007/s40194-023-01496-5>
- 57) Ming, H., Zhang, Z., Wang, J., Han, E. H., Wang, P., Sun, Z. Microstructure of a safe-end dissimilar metal weld joint (SA508-52-316L) prepared by narrow-gap GTAW, Materials Characterization, (2017) 123:233-243. <https://doi.org/10.1016/j.matchar.2016.11.029>
- 58) Wang, J., Sun, Q., Zhang, T., Zhang, S., Liu, Y., Feng, J. Arc characteristics in alternating magnetic field assisted narrow gap pulsed GTAW, Journal of Materials Processing Technology, (2018) 254:254-264. <https://doi.org/10.1016/j.jmatprotec.2017.11.042>
- 59) Traidia, A., Roger, F., Schroeder, J., Guyot, E., Marlaud, T. On the effects of gravity and sulfur content on the weld shape in horizontal narrow gap GTAW of stainless steels, Journal of Materials Processing Technology, (2013) 213(7):1128-1138. <https://doi.org/10.1016/j.jmatprotec.2013.01.010>
- 60) Guo, W., Li, L., Dong, S., Crowther, D., Thompson, A. Comparison of microstructure and mechanical properties of ultra-narrow gap laser and gas-metal-arc welded S960 high strength steel, Optics and Lasers in Engineering, (2017) 91:1-15. <https://doi.org/10.1016/j.optlaseng.2016.11.011>
- 61) Kim, J. S., Yi, H. J. Characteristics of GMAW narrow gap welding on the armor steel of combat vehicles, Applied Sciences, (2017) 7(7):658. <https://doi.org/10.3390/app7070658>
- 62) Abe, Y., Fujimoto, T., Nakatani, M., Shigeta, M., Tanaka, M. Study on proper welding condition for ultranarrow gap submerged arc welding, Welding International, (2021) 35(7-9):369-381. <https://doi.org/10.1080/09507116.2021.1980298>
- 63) Murayama, M., Oazamoto, D., Ooe, K. Narrow gap gas metal arc (GMA) welding technologies, JFE Technol. Rep, (2015) 20:147-153.

- 64) Iwata, S., Murayama, M., Kojima, Y. Application of narrow gap welding process with high speed rotating arc to box column joints of heavy thick plates, Jef Technical Report, (2009) 14(14):16-21.
- 65) Sumi, H., Kataoka, T., Kitani, Y. Application of narrow gap welding process with J-STARTM welding to shipbuilding and construction, JFE Tech. Rep, (2015) 20:112-117.
- 66) Funderburk, R. S. A look at input, Welding Innovation, (1999) 16(1), 359.
- 67) Peng, Y., Zhang, Y., Zhao, L., Ma, C., Tian, Z. Effect of heat input and heat treatment on microstructure and mechanical properties of welded joint of TMCP890 steel, Welding in the World, (2018) 62:961-971. <https://doi.org/10.1007/s40194-018-0587-5>
- 68) David, S. A., DebRoy, T. Current issues and problems in welding science, Science, (1992) 257(5069):497-502. <https://doi.org/10.1126/science.257.5069.497>
- 69) Babu, S. S. The mechanism of acicular ferrite in weld deposits, Current opinion in solid state and materials science, (2004) 8(3-4):267-278. <https://doi.org/10.1016/j.cossms.2004.10.001>
- 70) Grong, O., Matlock, D. K. Microstructural development in mild and low-alloy steel weld metals, International metals reviews, (1986) 31(1):27-48. <https://doi.org/10.1179/imtr.1986.31.1.27>
- 71) Onsøien, M. I., Liu, S., Olson, D.L. Shielding gas oxygen equivalent in weld metal microstructure optimization, Welding Journal, (1996) 75(7):216-s-224-s.
- 72) Aaronson, H.I., Wells, C. Sympathetic Nucleation of Ferrite, Journal of the Minerals, (1956) 8:1216–1223. <https://doi.org/10.1007/BF03377853>
- 73) Smith, Y. E., Coldren, A. P., Cryderman, R. L. Manganese molybdenum-niobium acicular ferrite steels with high strength and toughness, Proceedings of Conference on ‘Toward Improved Ductility and Toughness’, (1971) 119–142.
- 74) Davenport, E.S. Some Observations on Ferrite-Carbide Aggregates in Alloy Steels, Journal of the Minerals, (1957) 9:677–688 <https://doi.org/10.1007/BF03377922>
- 75) Shao, Y., Liu, C., Yan, Z., Li, H., Liu, Y. Formation mechanism and control methods of acicular ferrite in HSLA steels: A review. Journal of Materials

Science & Technology, (2018) 34(5):737-744.
<https://doi.org/10.1016/j.jmst.2017.11.020>

- 76) Wang, B., Zhang, Y., Qiu, F., Cai, G., Cui, W., Hu, Z., Zhang, H., Tyrer, N., Barber, G. C. Role of trace nanoparticles in manipulating the widmanstatten structure of low carbon steel, *Materials Letters*, (2022) 306:130853.
<https://doi.org/10.1016/j.matlet.2021.130853>
- 77) Cho, L., Tselikova, A., Holtgrewe, K., De Moor, E., Schmidt, R., Findley, K. O. Critical assessment 42: acicular ferrite formation and its influence on weld metal and heat-affected zone properties of steels, *Materials Science and Technology*, (2022) 38(17):1425-1433.
<https://doi.org/10.1080/02670836.2022.2088163>
- 78) Loder, D., Michelic, S. K., Bernhard, C. Acicular ferrite formation and its influencing factors—A review, *Journal of Materials Science Reserach*, (2017) 6(1):24. <http://dx.doi.org/10.5539/jmsr.v6n1p24>
- 79) Bhadeshia, H. K. D. H., Svensson, L. E. Modelling the evolution of microstructure in steel weld metal, *Mathematical modelling of weld phenomena*, (1993) 1:109-182.
- 80) Rees, G.I., Bhadeshia, H.K.D.H. Thermodynamics of acicular ferrite nucleation, *Materials Science and Technology*, (1994) 10(5):353-358.
<https://dx.doi.org/10.11179/mst.1994.10.5.353>
- 81) Lv, S., Wu, H. H., Wang, K., Wang, S., Wu, G., Gao, J., Yang, X.S., Zhu, J., Mao, X. The microstructure evolution and influence factors of acicular ferrite in low alloy steels, *Computational Materials Science*, (2023) 218:111989.
<https://doi.org/10.1016/j.commatsci.2022.111989>
- 82) Shao G, Liu Z, Fan J, Guo Y, Xu Q, Zhang J. Evaluation of Flux Basicity Concept Geared toward Estimation for Oxygen Content in Submerged Arc Welded Metal, *Metals*, (2022) 12(9):1530.
<https://doi.org/10.3390/met12091530>
- 83) Xu J, Zhou X, Zhu D. Effect of Arc Length on Oxygen Content and Mechanical Properties of Weld Metal during Pulsed GMAW. *Crystals*, (2022) 12(2):176. <https://doi.org/10.3390/cryst12020176>
- 84) Talaş, Ş. The assessment of carbon equivalent formulas in predicting the properties of steel weld metals. *Materials & Design* (1980-2015), (2010) 31(5):2649-2653. <https://doi.org/10.1016/j.matdes.2009.11.066>

- 85) CODE–STEEL, Structural Welding. AWS D1. 1/D1. 1M. American Welding Society 2020, 2020.
- 86) Wang, W. The great minds of carbon equivalent. Part I, EWI. org. (2015).
- 87) Ito, Y. Weldability formula for high strength steels related to heat affected zone cracking. Doc. IIW IX-576-68. (1968).
- 88) Yurioak, N, Oshita, S. and Tamehiro, H., Determination of necessary preheating temperature in steel welding, *Welding Journal*, (1983) 6:147-s – 153-s.
- 89) Mohrbacher H, Kern A. Nickel Alloying in Carbon Steel: Fundamentals and Applications, *Alloys*, (2023) 2(1):1-28. <https://doi.org/10.3390/alloys2010001>
- 90) Wang, Z. Q., Wang, X. L., Nan, Y. R., Shang, C. J., Wang, X. M., Liu, K., Chen, B. Effect of Ni content on the microstructure and mechanical properties of weld metal with both-side submerged arc welding technique, *Materials Characterization*, (2018) 138:67-77. <https://doi.org/10.1016/j.matchar.2018.01.039>
- 91) Andrews, K. W. Empirical formulae for the calculation of some transformation temperatures, *J Iron Steel Inst.*, (1965) :721-727.
- 92) Bhadeshia, H. K. D. H. *Bainite in steels: theory and practice*, CRC press. (2019).
- 93) Capdevila, C., García-Mateo, C., Chao, J., Caballero, F. G. Effect of V and N precipitation on acicular ferrite formation in sulfur-lean vanadium steels, *Metallurgical and Materials Transactions A*, . (2009). 40:522-538. <https://doi.org/10.1007/s11661-008-9730-z>
- 94) Jorge, J. C. F., De Souza, L. F. G., Mendes, M. C., Bott, I. S., Araújo, L. S., Dos Santos, V. R.,Rebello, J.M.A., Evans, G. M. Microstructure characterization and its relationship with impact toughness of C–Mn and high strength low alloy steel weld metals—a review, *Journal of Materials Research and Technology*, (2021) 10:471-501. <https://doi.org/10.1016/j.jmrt.2020.12.006>
- 95) Huang G, Wan X, Wu K, Zhao H, Misra RDK. Effects of Small Ni Addition on the Microstructure and Toughness of Coarse-Grained Heat-Affected Zone of High-Strength Low-Alloy Steel, *Metals*, (2018) 8(9):718. <https://doi.org/10.3390/met8090718>

- 96) You, Y., Shang, C., Subramanian, S. Effect of Ni addition on toughness and microstructure evolution in coarse grain heat affected zone, *Metals and Materials International*, (2014) 20:659-668. <https://doi.org/10.1007/s12540-014-4011-4>
- 97) Bunaziv, I., Langelandsvik, G., Ren, X., Westermann, I., Rørvik, G., Dørum, C., Danielsen, M.H., Eriksson, M. Effect of preheating and preplaced filler wire on microstructure and toughness in laser-arc hybrid welding of thick steel, *Journal of Manufacturing Processes*, (2022) 82:829-847. <https://doi.org/10.1016/j.jmapro.2022.08.026>
- 98) Kim, H. S., Jo, M., Park, J. Y., Kim, B. J., Kim, H. C., Nam, D., Kim, B., Ahn, Y. S. Effects of Ti microalloying on the microstructure and mechanical properties of acicular ferrite casting steel for high-speed railway brake discs. *Materials Science and Engineering: A*, (2022) 857:144125. <https://doi.org/10.1016/j.msea.2022.144125>
- 99) Dallam, C. B., Liu, S., Olson, D. L. Flux composition dependence of microstructure and toughness of submerged arc HSLA weldments. *Welding journal*, (1985) 64(5):140-151.
- 100) Carneiro, Í., Simões, S. Recent Advances in EBSD Characterization of Metals. *Metals*. (2020) 10(8):1097. <https://doi.org/10.3390/met10081097>
- 101) Gourgues A.-F., Flower, H. M., Lindley, T. C. Electron backscattering diffraction study of acicular ferrite, bainite, and martensite steel microstructures. *Materials Science and Technology*, (2000) 16(1):26-40. <https://doi.org/10.1179/026708300773002636>
- 102) Diaz-Fuentes, M., Iza-Mendia, A., Gutierrez, I. Analysis of different acicular ferrite microstructures in low-carbon steels by electron backscattered diffraction. Study of their toughness behavior. *Metallurgical and Materials Transactions A*, (2003) 34:2505-2516. <https://doi.org/10.1007/s11661-003-0010-7>
- 103) Lehto, P., Remes, H. EBSD characterisation of grain size distribution and grain sub-structures for ferritic steel weld metals. *Welding in the World*, (2022) 66(2):363-377. <https://doi.org/10.1007/s40194-021-01225-w>
- 104) Shamsujjoha, M. Evolution of microstructures, dislocation density and arrangement during deformation of low carbon lath martensitic steels, *Materials Science and Engineering: A*, (2020) 776:139039. <https://doi.org/10.1016/j.msea.2020.139039>

- 105) Suikkanen, P. P., Cayron, C., DeArdo, A. J., Karjalainen, L. P. Crystallographic analysis of martensite in 0.2 C-2.0 Mn-1.5 Si-0.6 Cr steel using EBSD, *Journal of Materials Science & Technology*, (2011) 27(10):920-930. [https://doi.org/10.1016/S1005-0302\(11\)60165-5](https://doi.org/10.1016/S1005-0302(11)60165-5)
- 106) Vogt, J. B., Bouquerel, J., Léaux, F., Palleschi, F. Fatigue damage assessment of alternator fans by EBSD, *Procedia Engineering*, (2013) 66: 608-614. <https://doi.org/10.1016/j.proeng.2013.12.112>
- 107) Nakamura, T., Hiraoka, K. Ultrannarrow GMAW process with newly developed wire melting control system, *Science and technology of welding and joining*, (2001) 6(6):355-362. <https://doi.org/10.1179/stw.2001.6.6.355>
- 108) Xie, X., Zhong, M., Zhao, T., Wang, C. Unravelling microstructure evolution induced mechanical responses in weld metals of EH420 shipbuilding steel subjected to varied high heat inputs. *Science and Technology of Welding and Joining*, (2022) 27(6):472-478. <https://doi.org/10.1080/13621718.2022.2064649>
- 109) Chen, H., Yang, Z., Zhang, C., Zhu, K., van der Zwaag, S. On the transition between grain boundary ferrite and bainitic ferrite in Fe–C–Mo and Fe–C–Mn alloys: The bay formation explained, *Acta Materialia*, (2016) 104:62-71. <https://doi.org/10.1016/j.actamat.2015.11.012>
- 110) Jia, X., Yang, Y., Ma, Y., Wang, B., Wang, B. In situ observation of phase transformations in the partially melted zone of HSLA offshore steel during simulated welding process, *Materials Today Communications*, (2023) 34:105012. <https://doi.org/10.1016/j.mtcomm.2022.105012>
- 111) Wu, H. D., Miyamoto, G., Yang, Z. G., Zhang, C., Chen, H., Furuhashi, T. Carbon enrichment during ferrite transformation in Fe-Si-C alloys, *Acta Materialia*, (2018) 149:68-77. <https://doi.org/10.1016/j.actamat.2018.02.040>
- 112) Shrestha, S. L., Breen, A. J., Trimby, P., Proust, G., Ringer, S. P., Cairney, J. M. An automated method of quantifying ferrite microstructures using electron backscatter diffraction (EBSD) data, *Ultramicroscopy*, (2014) 137:40-47. <https://doi.org/10.1016/j.ultramic.2013.11.003>

Published or Submitted Papers in Regard to This Thesis

1. **Suwannatee, N.**, Wonthaisong, S., Yamamoto, M., Shinohara, M., Phaoniam, R. Optimization of Welding Conditions for Hot-wire GMAW with CO₂ Shielding on Heavy-thick Butt Joint, *Welding in the world*, 66, 2022, p. 833-844. (Chapter 4 & 5)
2. **Suwannatee, N.**, Wonthaisong S., Phaoniam, R., Shinohara, R., Choi, J. W., Yamamoto, M. The Optimization of High Efficiency and Low Heat Input Hot-wire Gas Metal Arc Welding for Thick Steel Plate in Shipbuilding Industry, *Proceeding of IIW2022 – International Conference on Welding and Joining*, Tokyo, Japan, 2022, p. 346-348. (Chapter 4)
3. **Suwannatee, N.**, Nakamura, K., Choi, J. W., Yamamoto, M. Large process tolerance of single-pass hot-wire MAG welding, *Proceeding of Visual-JW 2022 – The 6th International Symposium on Visualization in Joining & Welding Science through Advanced Measurements and Simulation*, Osaka, Japan, p. 31. (Chapter 3)
4. **Suwannatee, N.**, Yamamoto, M. Single-Pass Process of Square Butt Joints without Edge Preparation Using Hot-Wire Gas Metal Arc Welding. *Metals*, 13 (6):1014, 2023. (Chapter 3)
5. **Suwannatee, N.**, Yamamoto, M., Shinohara, M. Optimization of Hot-wire Fraction for Enhance Quality in Gas Metal Arc Welding, *Proceeding of IIW2023 – The 76th Annual Meeting and International Conference on Welding and Joining*, Document No. XV-1665-2023 (Chapter 4 & 5)

Presentations

1. **Suwannatee, N.**, Wonthaisong, S., Yamamoto, M., Shinohara, S. Development of Hot-wire gas metal arc welding, The 74th IIW Annual assembly and International Conference, Genoa, Italy, 2021. (Chapter 4 & 5)
2. **Suwannatee, N.**, Wonthaisong, S., Yamamoto, M., Shinohara, Phaoniam, R. The Optimization of High Efficiency and Low Heat Input Hot-wire Gas Metal Arc Welding for Thick Steel Plate in Shipbuilding Industry, The 75th IIW Annual Assembly and International Conference , Tokyo, Japan, 2022. (Chapter 4 & 5)
3. **Suwannatee, N.**, Nakamura, K., Choi, J. W., Yamamoto, M. Large Process Tolerance of Single-pass hot-wire MAG welding, The 6th International Symposium on Visualization in Joining & Welding Science through Advanced Measurements and Simulation, Visual-JW 2022, Osaka, Japan, 2022. (Chapter 3)
4. **Suwannatee, N.**, Yamamoto, M. Shinohara, S. Optimization of Hot-wire Fraction for Enhance Quality in Gas Metal Arc Welding, The 76th IIW Annual Assembly and International Conference, Singapore, 2023. (Chapter 4 & 5)